Reflectance Analysis of Layered Surfaces using a Multispectral Image

Tetsuro Morimoto

A Doctoral Dissertation

Submitted to the Graduate School of
the University of Tokyo

東京大学
THE UNIVERSITY OF TOKYO

in Partial Fulfillment of the Requirements
for the Degree of
Doctor of Information Science and Technology

June 2009

Committee:

Takeshi NAEMURA (Chair)
Jun ADACHI
Kiyoharu AIZAWA
Kaoru SEZAKI
Masashi TOYODA

Supervisor:

Katsushi IKEUCHI

ABSTRACT

Despite great public interest in cultural assets, knowledge of these assets is often restricted because of the possibility of deterioration and collapse. Consequently, it has become an important goal in the computer science community to model and record these restricted assets and then use the digital data associated with such assets in a variety of ways. For example, digital data is used to create digital media such as computer graphics CG) and virtual reality (VR) content. It is also used for analysis that can aid in the restoration and preservation of cultural assets.

Therefore, it is important to understand how to use this digital data to preserve the important information about cultural assets, including their shape and surface color. Usually, shape information can be obtained by a laser range sensor, and this information has become more accessible with improved data processing algorithms. However, current color imaging systems like digital still camera (DSC) are usually represented with the traditional red, green, blue (RGB) color model. RGB cannot always provide accurate color information. The color of images captured with DSC is dependent on both the characteristics of the device and the condition of the illumination environment, making it difficult to accurately represent color appearance in the real world. Consequently, we need to capture surface spectral reflectance as ultimate color information in order to preserve the accurate color of cultural assets.

Spectral reflectance is inherent in the nature of objects. Object analysis using the fact that different materials have different spectral reflectance is performed in many fields, such as medical imaging, agriculture, archaeology, and art. However, in the real world, it is difficult to obtain and handle a multispectral image effectively. Many objects are often found in an outdoor environment or in a dark environment, and these can pose problems. In an outdoor environment, for instance, the illumination environment changes greatly from one time to another. This causes saturation and underexposure when measuring the spectra. Moreover, many objects have at their surface complex reflection, absorption, and scattering, with a color mixture between the top and bottom layers, making material segmentation impossible. This dissertation targets analysis of cultural assets having such multilayered characteristics.

Our goal is development of novel multispectral imaging systems for modeling cultural assets, proposing reflectance analysis methods using a multispectral image, and applying them in practice. The dissertation proposes the following three tasks related to preservation, release, and analysis.

First, we propose a practical color restoration method based on spectral informa-

tion. In order to make VR contents by using 3D data, texture images by DSC are generally used as color information. However, the color of images captured with DSC is dependent on both the characteristics of the device and the condition of the illumination environment, and often the color information is not accurate. In a narrow environment, such as a tumulus, compact mobility is necessary to measure spectra. For these circumstances, we propose a color restoration method that uses both high resolution images captured by DSC and spectral information captured by a conventional spectrometer. This is a practical method from the viewpoint of automation and computational cost.

Second, we propose an efficient method for acquiring and segmenting multi-spectral images captured in outdoor environments. A conventional multispectral imaging system may have two kinds of cameras. The first is a multiband camera, which is mainly used in the color reproduction field and does not have high spectral resolution, but has high image quality. The second is a hyperspectral sensor, which is mainly used in the aerial remote sensing field and does not have high image quality, but has high spectral resolution. Compared to these systems our solution has not only high image quality and sufficient spectral resolution for object analysis but also a wide capture angle. The multispectral image segmentation method can handle object surfaces having complex reflection based on a statistical procedure.

Finally, a novel physical model, the so-called "Spider" model, which can be used to estimate the optical properties of layered surfaces, is proposed. Many object surfaces such as wall paintings are composed of layers of different physical substances, and are called "layered surfaces." Such surfaces have more complex optical properties than a diffuse surface and are generally unable to be segmented. For this reason, we propose the Spider model to analyze the complex optical properties of layered surfaces. We also develop a novel method that can not only segment the surfaces but also decompose the optical properties of layered surfaces.

The main contribution of this thesis is to propose two multispectral imaging methods and two reflectance analysis methods. We apply these not only in theory but also in practice to show their viability. The contribution can be specifically summarized by the five following points: First, we have developed a practical color restoration method based on spectral information for making VR contents, have actually produced VR contents by using restored images, and have also showed them in the Kyushu national museum. Second, we have developed a multispectral imaging system that can efficiently acquire spectra in a wide field. Third, we have proposed

a multispectral image segmentation method based on statistical procedures. Fourth, we have proposed the Spider model as a physical model for layered surfaces, and have also proposed decomposing complex reflection components of a layered surface. To our knowledge, there are no methods sharing our goals and techniques. Finally, we have applied our methods to both the reflectance analysis of tumuli and the spectral analysis of the bas-relief in the Inner Gallery of the Bayon Temple. These methods are specifically designed for modeling cultural assets, but they can be used in other fields as well.

CG VR

( )

DSC RGB

RGB

RGB

DSC

VR

DSC RGB

RGB

iv

RGB

VR
VR

Acknowledgements

First of all, I would like to express my sincere thanks to my advisor, Prof. Katsushi Ikeuchi, for his strong support and encouragement. He gave me the opportunity for valuable research experience. I feel very fortunate to have been able to work with a man who is such an honorable leader and researcher.

I would also like to thank my committee members, Prof. Takeshi Naemura, Prof. Jun Adachi, Prof. Kiyoharu Aizawa, Prof. Kaoru Sezaki, and Prof. Masashi Toyoda. Their comments greatly improved the contents of this dissertation. I am also grateful to ex-committee member Prof. Hiroshi Harashima for his valuable advice on this dissertation.

I would like to thank Toppan Printing which, during these three years, has supported me through this doctoral degree. I would also like to thank the members of our Toppan Printing team for their support and cooperation in making VR contents and measuring tumuli.

Many thanks to the current and former members of the Computer Vision Laboratory at the University of Tokyo with whom I have discussed problems in computer vision. I am especially grateful to Dr. Daisuke Miyazaki, Dr. Rei Kawakami, and Tomoaki Higo, who gave me many ideas and held important discussions with me throughout my work, and to Bjoern Rennhak and Kento Fujiwara, who help me to write papers in English. I am also grateful to others who made my lab-time enjoyable.

I am also very grateful to Prof. Robby T. Tan. Through collaborative research with him, I learned a great deal about how to proceed in my research and how to write this dissertation.

I am also grateful to Dr. Nobuaki Kuchitsu (National Research Institute for Cultural Properties, Tokyo) and Dr. Kazutaka Kawano (Kyushu National Museum) for their

Contents

List of Figures

List of Tables

Chapter 1

Introduction

1.1 Background

Motivation   Many valuable cultural assets all over the world have been in grave danger of collapse and deterioration due to weathering from sources such as salt erosion, oxidation degradation, and biodeterioration. For protecting cultural assets, it is difficult to decide whether or not to exhibit them. Consequently, many institutions that want to share cultural assets but also preserve them have focused on creating models of these assets. Some examples are Stanford's Michelangelo projects [51], IBM's Pieta Project [105], and the Bayon Temple Project [44]. Modeling cultural assets permits the exhibition of restricted cultural assets through digital data. These digital data are used to create digital media, or so-called Virtual Reality (VR) models of sites such as the Bayon Temple and the Parthenon [44, 10], the Toppan Museum [60], the Asuko-Kyo ruins [35], and Internet contents [59, 61]. The data are also analyzed for restoration and preservation purposes. In addition, our laboratory has digitized and analyzed the 3D shape and color of cultural assets through such projects as the Digital Bayon Project [44], the Great Buddha Project [32], and the Decorated Toms Project [55].

Usually, 3D shape information can be obtained by a laser range sensor at different viewpoints. Obtained 3D range data thus provide clouds of points of range information. Modeling them involves two processes. First, a set of range data that covers an entire object's surface consists of multiple data sets obtained with respect to their relative coordinate systems. An alignment process is necessary to determine the

relations among these sensor coordinate systems [66, 67]. Next, a merging process [76, 75] extracts one surface from multiple overlapped surfaces, since each range data set covers only a part of a whole object's surface. The merging process also reduces noise and produces a smoother surface. Aside from the laser range sensor, several computer vision techniques, such as photometric stereo [30, 110, 90, 25, 85, 27, 95, 26], binocular stereo [88, 106, 22, 28, 91, 109], multiview stereo [113, 102, 21, 81, 65, 19], and visual hull [82], also provide clouds of points of range information. Currently, many methods related to shape have been proposed.

As for color information, this can generally be obtained as a color image by Digital Still Camera (DSC), having RGB color components. For making a VR model, many obtained color images are mapped onto a 3D shape. When an object is located outdoors, the color picture taken contains both illumination color and object color. Thus, the color appearance of a synthesized VR model is different from one part to another. To prevent this effect, many methods to obtain color constancy by removing illumination color have been proposed [37, 36, 14, 16, 15, 94].

However, RGB color cannot always provide accurate color appearance. Color information precisely represents its spectral power distribution as a function of wavelengths from 380 nm to 780 nm. Thus, RGB color means that a continuous spectrum is reduced to three sensory quantities, and the color appearances of objects with different spectral power distributions often match. This phenomenon is called metamerism. This is a ubiquitous phenomenon that affects many areas of color imaging. Fig.1.1.a shows pictures of metamers (GATF/RHEM light indicator strips) under two illuminations. Under D50 illumination in Fig.1.1, we are not able to observe strips. However, strips are visible when the strip is viewed under other lighting, such as incandescent 5900K in Fig.1.1.b. We cannot restore the strips from the RGB image of Fig.1.1.a, but we can restore the strips from spectral information of Fig.1.1.a. Because these reflectance spectra do not match, but the RGB values match under D50 illumination. Consequently, it is necessary for us to measure the spectral power distribution of reflecting surface to acquire accurate color information. In this dissertation, we focus on methods for obtaining and analyzing spectral information of cultural assets.

The spectral power distribution is usually measured by an instrument called a spectrometer. This instrument can measure the absolute spectral power distribution of the incoming light, and is also useful from the viewpoint of mobility. However, the measurement area is limited to a small point, about 5 mm to 2 cm. Therefore,

(a) D50 illumination   (b) 5900K(PSR500WD)
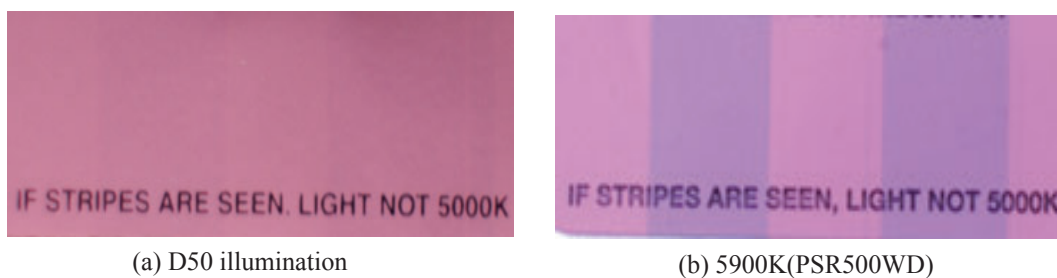
Figure 1.1: Light indicator strips under D50 (a) and 5900K (b). Viewed under 5000K or D50 standardized lighting conditions, light indicator strips cannot appear to be a solid color.

directly applying obtained spectra to a VR model using a spectrometer is difficult.

Various types of multispectral imaging systems have been developed in the remote sensing field, the color reproduction field, and the computer vision field. However, most multispectral imaging systems are restricted in the objective of the fields, such as cross-environment color reproduction and material analysis.   For preserving color information of cultural assets, we need to obtain an image having high spectral resolution, low noise, a wide field of view, high image resolution, and no distortion.

Furthermore, in an outdoor environment, it is difficult to obtain a multispectral image. Cultural assets are often located in severe outdoor environments. In an outdoor environment, wide alterations in the illumination environment often occur quickly. Fixed exposure of a system causes saturation and underexposure. Also, a multispectral imaging system that changes optical filters in temporal sequence commonly affects both the alteration of illumination intensity and the waveform of the illumination spectrum. We need to design the system considering these effects.

We can accurately analyze materials by using obtained multispectral images. However, the spectral information having high dimensional data space creates new problems in the development of data analysis techniques. This problem is known as "the curse of dimensionality [3]." Previous research has demonstrated that high dimensional data spaces are mostly empty, indicating that the data structure involved exists primarily in a subspace. It is necessary for us to develop a dimension reduction method for estimating optimal subspace without losing the original information that allows for their separation.

One of the most widely used dimension reduction techniques is principal component analysis (PCA). However, most cultural assets have complicated surfaces

with inter-reflection, absorption, and scattering. Moreover, there is a color mixture between the top layers and the bottom layer. Unfortunately, PCA, a linear dimension reduction method, cannot handle such nonlinear effects. For this reason, it is necessary for us to develop a reflection analysis method for handling nonlinear effects.

As mention above, to obtain and analyze spectral information of cultural assets involves many challenging tasks, and also contributes many applications for modeling cultural assets.

Goal   Considering the importance in various computer vision applications of modeling cultural assets, our ultimate purpose is to develop reflectance analysis methods for restoration or preservation of cultural assets. For this purpose, first, it is necessary for us to develop a new multispectral imaging system for preserving accurate color information of cultural assets, since a conventional system is unfit for our purpose. Basically, we have to consider several factors for achieving these purposes, as discussed below.

With respect to multispectral imaging, we considered two approaches. The first is how to synthesize many multispectral images having high image quality for making digital archive contents efficiently. The second is how to obtain a multispectral image having a wide field of view of high resolution with low noise for analyzing different materials on an object's surface. For the former, we invent a method using a sensor fusion approach; for the latter, we develop a new multispectral imaging system, and also apply this system for measuring the surface spectra on an object's surface in an outdoor environment.

With respect to reflectance analysis, we consider how to segment a multispectral image considering nonlinear features between different materials such as the top layer's spectra and the bottom layer's spectra. For this purpose, we have developed two approaches: a statistics-based approach and a physics-based approach.

The statistics-based approach can effectively segment spectra having different materials by using nonlinear dimension reduction. On the other hand, our proposed physics-based approach can not only segment a multispectral image considering the nonlinearity of the spectra, but also can decompose each layer's optical properties.

We apply these approaches to our projects, demonstrating not only their practicality but also their accuracy and robustness.

1.2   Acquisition of Spectral Information

 First of all, we describe spectral information. Light in the atomic scale consist of a packet of energy called photons. A photon radiated from its source moves in a perfectly straight direction, unless something affects its motion. As photons move, they also oscillate to form a spectrum of wavelengths. Photons that form visible lights cover just a small portion of wavelength, which falls between 380 nm and 780 nm. The spectral power distribution of light determines the color we perceive.

The measurement of the spectral power distributions of light is the field of spectroradiometry, which is the measurement of radiometric quantities as a function of wavelength. Of particular interests in computer vision or color appearance are irradiance and radiance. Both are measurements of the power of light sources based on the basic units of watts.

Spectral power distribution is usually measured as spectral radiance or spectral irradiance by an instrument called a spectrometer.

Irradiance is the radiance power per unit area incident onto a surface and has units of watts per square meter (Wm^2). Spectral irradiance adds the wavelength dependency and has units (Wm^2)nm. Radiance differs from irradiance in that it is a measure of the power emitted from a source, rather than incident upon a surface, per unit area per unit solid angle with units of watts per square meter per steradian (Wm^2sr). Spectral radiance includes the wavelength dependency having units of W/m^2srnm.

Although measurement is restricted to one small area (point), measuring the observed light intensity as a physical value (watt) is a large advantage. Over the past several decades, a considerable number of studies have been conducted on multispectral imaging especially in a remote sensing field and a color reproduction field.

Multispectral Imaging   In the 1960s, researchers in the remote sensing field first made aircraft-mounted sensors. Their sensors were optical-mechanical line scanning devices. They were capable of scanning a pixel of a multispectral image having information less than 20 spectral bands over the visible, reflective infrared (IR), and thermal IR regions of the spectrum.

However, the multispectral imaging system for space only allowed a four-band system with 80 m pixels and an S/N justifying a 6-bit data system. This system, called MSS (multispectral scanner), was first launched in July 1972 aboard the Landsat 1

<div style="text-align:center">(a)   (b)</div>
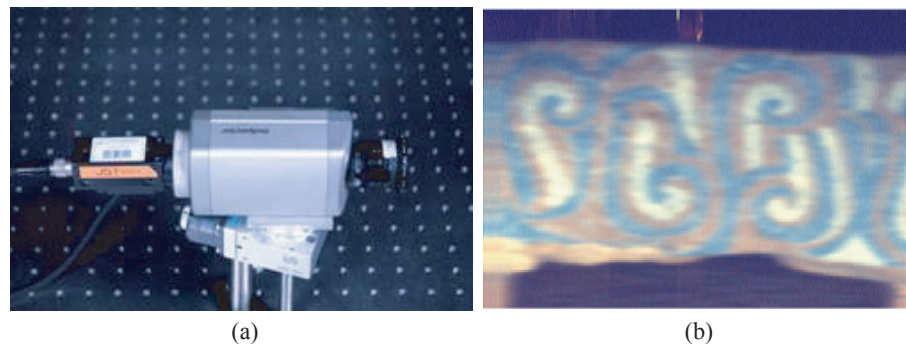
Figure 1.2: Hyperspectral sensor system. (a) Sensor system (ImSpector Specim Ltd.) (b) Captured image: this image is an RGB image transformed from spectra.

satellite.

After that, multispectral imaging technology advanced substantially. New multispectral sensors have several hundred spectral bands and an S/N requiring 10+ bit data systems. In November 2000, NASA launched an EO-1 spacecraft carrying a sensor system called Hyperion that has 220 bands, 30 m pixels, and a 10-bit data system.

This system demonstrated what sensor technology is now capable of producing. Sensors with this many spectral bands are referred to as hyperspectral.

Hyperspectral sensor systems view the scene through a narrow slit perpendicular to the frame's x-axis. The light coming through the 1D slit is dispersed by prisms or diffraction gratings onto a 2D detector array; hence a spectrum of high spectral resolution is obtainable for a pixel-wide column of the scene. The multispectral image is obtained by scanning the scene in pixel increments along the x-axis.

Ikari et al. restored an RGB trichromatic color image based on spectral information obtained by matching an RGB image and multispectral image using a hyperspectral sensor [29, 86] through geometric data. However, a prism or diffraction grating needs sufficient light intensity. And when the target object has a 3D shape, it is difficult to adjust the lens focus. Fig.1.2 shows the system and captured image.

Subsequently, a multiband camera system has been developed to perform cross-environment color reproduction for objects [56, 23] in the color reproduction field. The reflectance spectra of the objects are acquired in this imaging system for calculating the trichromatic color values under arbitrary illumination. The multiband camera usually performs using five or more color filters to obtain accurate color re-

<center>(a)</center> <center>(b)</center>
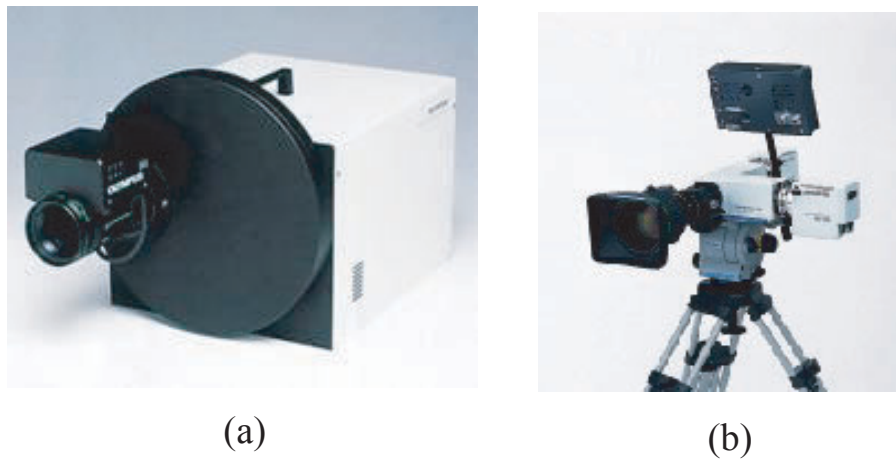
Figure 1.3: Multiband camera. (a) Wheel type 16 band multiband camera (Olympus Co., Ltd) (b) 6 band HDTV camera

production across various illumination environments. Typically, the rotating filters are mounted in front of a monochromatic CCD camera [56, 112]. This system cannot obtain an image having high spectral resolution, but can obtain an image having low noise and high image resolution. Most methods do not directly use obtained spectral information, but estimate reflectance spectra having higher spectral resolution from a spectral reflectance database: they restrict target objects [98, 56, 112]. Fig.1.3 shows examples of a multiband camera system.

Aside from these systems, Yoav et al. developed a multispectral imaging system by using a fixed spatially varying spectral filter and a monochromatic CCD camera [80, 29]. This system can obtain a multispectral imaging having high spectral resolution by using traditional image mosaics technique. This system rigidly attaches (either in front or behind the imaging lens) an optical filter with spatially varying properties to the camera. When this imaging system moves in a horizontal direction, each scene point is measured multiple times under different wavelengths. Fusing the data captured in the multiple images yields an image mosaic that includes spectral information about the scene. However, the image quality depends on the accuracy of the image mosaic.

1.3 Reflectance Analysis

In many fields, object recognition applications have been developed using differences of reflectance. For these applications, we need to consider the optical properties
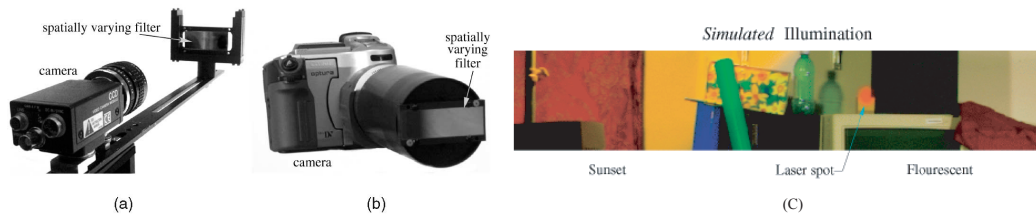
Figure 1.4: Multispectral imaging system using linear variable interference filter (a)(b) Sensor system. (c) Synthesized RGB image.
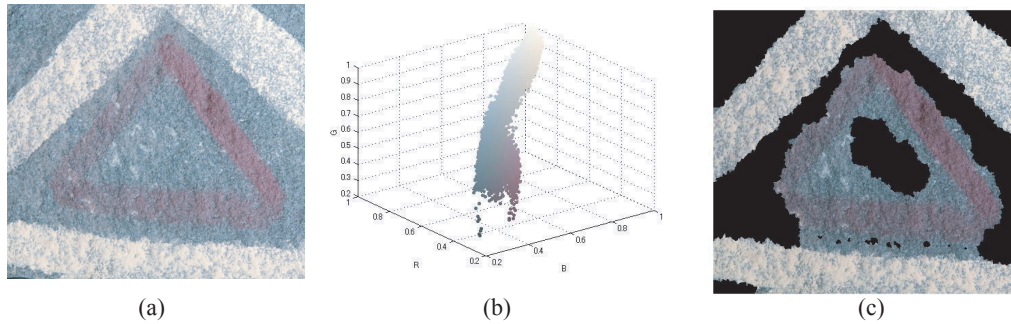
Figure 1.5: Nonlinearity of layered surface (a) Input RGB image. (b) The RGB plot of image (a). (c) The result of lazy snapping method [52]

of the object's surface. For example, specular reflection of the object is one of the causes of intractable segmentation. Tan et al. proposed a method decomposing specular and diffuse reflection using an image [93, 92, 99]. Note that we assume that our targets have no specular reflection in this dissertation, since this reflection is negligible.

On the other hand, many object surfaces are composed of layers of different physical substances, and these are known as layered surfaces. Such surfaces (e.g., patinas, water colors, and wall paintings) have more complex optical properties than diffuse surfaces, and generally cannot be segmented. This is because their colors change according to the mixtures of the optical properties of the layers. Fig.1.5 shows an example of layered surfaces. Note that their color change is nonlinear as shown in Fig.1.5.b: we cannot separate their distribution of color linearly. In computer vision, we may try to segment such layered surfaces using an image segmentation method, and many effective image segmentation methods have been proposed. Graph cut methods based on graph theory, such as Lazy Snapping [52] and Grab Cut [71], have been proposed. These methods can efficiently segment a

foreground with a background. However, handling a nonlinear feature would be difficult. Consequently, these methods would often fail to segment colors of layered surfaces as shown in Fig.1.5. Furthermore, most segmentation methods cannot be applied to high dimensional data.

There are two approaches to analyzing layered surfaces: a statistics-based approach and a physics-based approach. We describe these approaches here.

Statistics-based Approach   The surface spectral reflectance of an object refers to the object's ability to reflect different spectral distribution when light shines on it. Formally, it is defined as the ratio of reflected spectral power distribution to the incident spectral power distribution. In general, this spectral reflectance is the most crucial factor in recognizing an object, since optically different objects will have different spectral reflectances.

Fu et al. proposed an automatic absorption detection method by analyzing geometrical features of the reflectance spectrum [18]. This approach assumes absorption is represented as the valley of shape of spectral reflectance. Beside this example, many object recognition methods [5, 54, 43, 98] using reflectance spectra have been proposed in many fields.

The segmentation of high dimensional spectra needs a dimension reduction for overcoming the "curse of dimensionality [3]." One of the most widely use dimension reduction techniques is principal component analysis (PCA). PCA computes orthogonal projections that maximize the amount of data variance, and yields a dataset in a new uncorrelated coordinate system. Unfortunately, information content in multispectral images does not always much such projections. PCA cannot handle nonlinear features, since PCA is linear dimension reduction.

Therefore, the nonlinear dimension reduction methods, such as kernel principle component analysis (kernel PCA) [78] and kernel canonical correlation analysis (kernel CCA) are widely used. Kernel analysis methods are based on mapping data from the original input feature space to a kernel feature space of higher dimensionality, and then solving a linear problem in that space. This operation is called the "kernel trick." Many methods was proposed using the kernel trick [3]. Fig.1.6 depicts an example of the kernel trick. Fig.1.6.b shows how input data can be separated into two classes linearly using the kernel trick.

In the remote sensing field, some methods using nonlinear analysis have been proposed [43, 46, 54]. The classification of multispectral images [101] was proposed

(a)   (b)
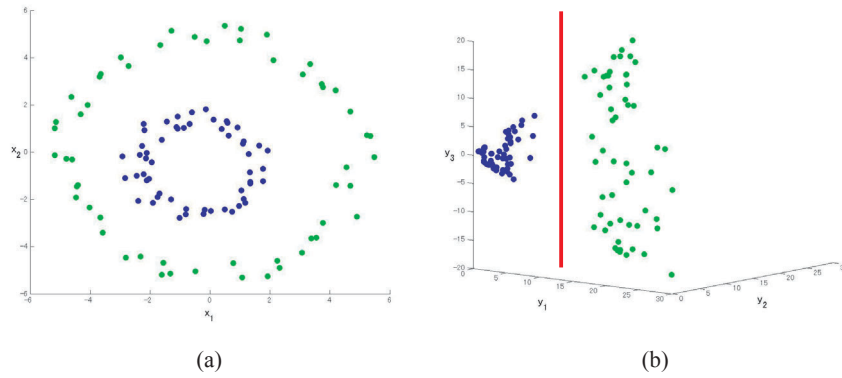
Figure 1.6: Kernel trick: (a) is linearly inseparable, while (b) is linearly separable. (a) Input data. (b) Transformed input data in kernel space using kernel function $(y_1, y_2, y_3) = (x_1^2, x_2^2, \sqrt{2}x_1x_2)$.

using the kernel-based method. Kwon et al. proposed the object detection method, which combines the kernel-based method and linear subspace detection method [43]. These methods are similar to our approach. However, their purpose is not to analyze the layered surfaces, but to develop a method without the effect of noise.

Keshava et al. introduced so-called spectral unmixing methods [38]. The mixed pixels are a mixture of more than one distinct substance, and they exist for one of two reasons. First, if the spatial resolution of a sensor is low enough that disparate materials can jointly occupy a single pixel, the resulting spectral measurement will be some composite of the individual spectra. This is the case for remote sensing platforms flying at a high altitude or performing wide-area surveillance, where low spatial resolution is common. Furthermore, there exists a linear relationship between the fraction of the substances comprising the area being imaged and the spectra in the reflected radiation: we can solve this problem using a linear method. Second, mixed pixels can result when distinct materials are combined into a homogeneous mixture. This circumstance can be solved independent of the spatial resolution of the sensor, and is same as the circumstance of layered surfaces: we need to solve this problem using a nonlinear method. However, a segmentation method handling nonlinear mixing of layered surfaces does not exist. Developing such a method is a challenging task ahead.

Physics-based Approach   In multilayered surfaces, each layer may have different optical parameter values. These values and the order of the layers physically
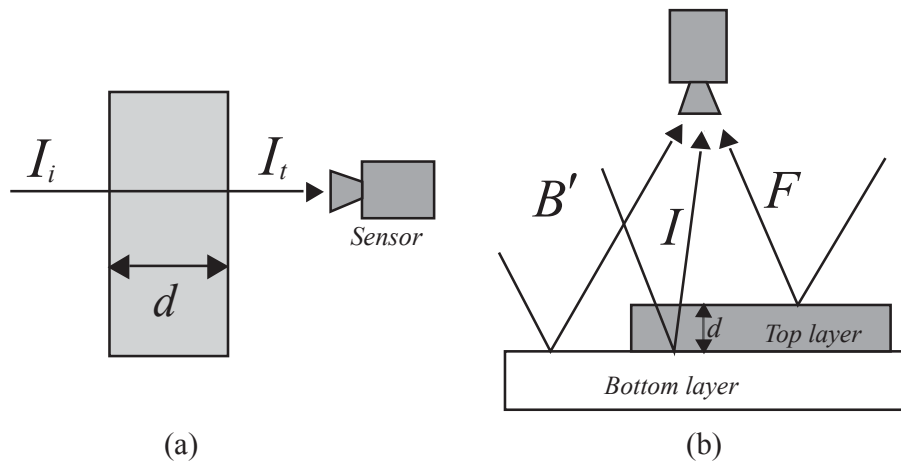
Figure 1.7: (a) The optical model of the Lambert-beer model. (b) The optical model of Lambert-beer based model.

determine the reflectance of an object and therefore also the object's appearance. For example, human skin roughly consists of two layers, namely the dermis and epidermis [100], which both contribute to the unique appearance of skin. Other examples are plant leaves, biological tissues, and oxidized objects. Surface layers are not only found on solid materials, but also exist in other forms of turbid media, such as seawater [79] and fog [73]. The fields of optics and color science have introduced many models of multilayered objects [4, 41, 111, 34, 6, 68]. These models are principally based on radiative transfer theory [6], which was originally developed in the field of astrophysics. One highly detailed representation is the many-flux scattering model presented by Mudgett [58]. Since this complex model has many parameters that make it difficult to apply, a simpler two-flux approximation called the Kubelka-Munk (KM) model [42] has been more commonly used. However, for image processing, the KM model has many parameters that make it difficult to apply to an image. Also of interest is the Lambert-Beer law, which does not explicitly take account of the scattering coefficient but is mathematically much simpler than the KM model. Many researchers in physics-based computer vision successfully use the Lambert-Beer model (e.g., [63, 62, 73, 11, 79]). Details of the Lambert-Beer law are presented here.

Light traveling in an optical medium is attenuated by absorption and scattering as shown in Fig. 1.7.a. When the concentration of the absorption in the medium is higher, transmitted energy along the regular path is reduced. The energy removed from the transmitted light is either absorbed or scattered to other directions. If the

medium does not cause significant multiple scattering, the radiant flux density of the transmitted light, I_t is related to the radiant flux density of the incident light I_i by two laws:

1. Lambert law: $I_t(\lambda) = I_i(\lambda)e^{-\alpha(\lambda)d}$, where $\alpha(\lambda)$ is absorption coefficient and d the thickness of the medium. In this law, absorbance is proportional to the thickness d of the medium.

2. Beer's law: $I_t(\lambda) = I_i(\lambda)e^{-\beta(\lambda)c}$, where c is the concentration of the absorbing medium. In this law, absorbance is proportional to the concentration c of the absorbing medium.

The two laws can be combined into a law called the Lambert-Beer law [47]:

$$L_t(\lambda) = L_i(\lambda)e^{-\mu(\lambda)cd} \tag{1.1}$$

If the density of particle is uniform in medium, the concentration of the absorbing medium is $c = 1$. We can rewrite Eq.(1.2):

$$L_t(\lambda) = L_i(\lambda)e^{-\mu(\lambda)d} \tag{1.2}$$

The Lambert-Beer law is true only when the effect of multiple scattering is negligible. Once energy is scattered away the in forward direction, a particle can be scattered back into the forward direction by a second particle. This can only happen if there is a large number if particles along the path, either because the concentration of particles is high or because the path is long.

The Lambert-Beer Law is the foundation for a model commonly used in oceanic, atmospheric optics to describe the light attenuations caused by the medium's particles, where a cloud of the particles in the medium is treated as a transparent object. However, instead of assuming light coming from one direction, this model conveys the idea of light coming from two directions simultaneously, namely from the back of the particle cloud and from the front of the particle cloud:

$$I(\lambda) = B(\lambda)e^{-\mu(\lambda)d} + F(\lambda)\left(1 - e^{-\mu(\lambda)d}\right) \tag{1.3}$$

where I is the mixture intensity of the transmitted light from B and the reflected light from F. We call I a mixed layer: B and F are the intensity of light coming from the back and the front of the particle cloud, respectively. The first term at the right side of the equation is exactly the same as the Lambert-Beer Law, while the second

term is the consequence of the first term, by assuming that the light travels solely to forward and backward directions. This means that if the attenuation of the object or particle cloud is $e^{-\mu(\lambda)d}$, then the remaining reflection factor is $(1 - e^{-\mu(\lambda)d})$. We call the model the Lambert-Beer based model, or LB-based model. Fig.1.7 depicts the optical model of the LB-based model.

Note that the absorption coefficient μ of the LB-based model depends on wavelength. However, most methods such as digital matting, vision in bad weather, and underwater vision, assume the absorption coefficient is scalar. This assumption causes a critical error for segmentation of layered surfaces because color on layered surfaces changes not linearly but nonlinearly as shown in Fig.1.5.b.

As mentioned above, a method considering nonlinearity of layered surfaces remains to be proposed. We consider the development of such a method could benefit many applications in computer vision and graphics.

1.4 Thesis Overview

In this dissertation, we propose two multispectral imaging methods and two reflectance analysis methods. For multispectral imaging methods, we introduce two approaches, one using sensor fusion and the other by developing a hardware system. For reflectance analysis, we introduce two approaches, one a statistics-based approach and the other a physics-based approach. In each chapter, we apply proposed approaches to practice to show their viability. The structure of each chapter is as follows:

In Chapter 2, we propose a method for color restoration that can effectively apply accurate color based on spectral information to a segmented image using the normalized cuts technique. This approach implies that we can synthesize a roughly multispectral image. First, we describe the Normalized Cuts (NCuts), and the segmentation of the DSC image. Second, we describe restoring segmented color areas using spectral information. Finally, the results of some experiments such as color accuracy, restoration of metamers, and application of digital archive contents, are presented, and we summarize the chapter.

In Chapter 3, we describe a new multispectral imaging system that we have developed. We first describe our hardware design for panoramic multispectral imaging and effectively capturing techniques of data acquisition for cultural assets in an outdoor environment. Obtained multispectral images have a spectrum of sufficient

spectral resolution in each pixel. We can classify different materials by segmenting different spectra. To segment a multispectral image, it is necessary for us to reduce the dimension of the spectrum in the image considering a nonlinear feature. Therefore, second, we derive a nonlinear dimension reduction method using the "kernel trick" and NCuts method, and apply NCuts segmentation to a multispectral image. Third, we evaluate our methods by experiments, and demonstrate the application for analyzing micro-organisms on the bas-reliefs of the Bayon temple. Finally, we summarize the chapter.

In Chapter 4, we propose a novel physical model considering spectra change of layered surfaces, and also propose a method that can decompose optical properties of each layer using the model. Here, we focus mainly on surfaces with two layers, top and bottom. There are no methods sharing our goals and techniques. We first describe the layered surface model. Then, we introduce a new physical model, which is called the Spider model, and which can represent a nonlinear correlation between spectra wavelengths on layered surfaces. After introducing the model, we describe how to use it for estimation and for segmenting layered surfaces. We can accurately segment surface materials using the Spider model and the Markov random fields (MRFs) model to estimate the properties of the top and bottom layers. We provide some experiments such as comparison with conventional methods and demonstration using a real image. In this chapter, we also describe a method based on RGB color for the sake of understanding. Next, we explain the extended method based on spectral information. Then we summarize the chapter.

Finally, chapter 5 concludes this dissertation by summarizing this research and contributions, and discussing possible future research directions.

Chapter 2

Color Restoration Method Based on Spectral Information Using Normalized Cuts

In this chapter, we propose a novel method for color restoration that can effectively apply accurate color based on spectral information to a segmented image using the Normalized Cuts technique. Using the proposed method, we can obtain a digital still camera image and spectral information in different environments. Also, it is not necessary to estimate reflectance spectra using a spectral database such as those that are used in other methods. The synthesized images have accurate color and high resolution. The proposed method works effectively when applied to digital archive contents.

2.1 Introduction

Highly accurate image synthesis is important in many fields such as remote sensing, medical imaging, agriculture, archaeology, and art. Our goal is to design a system that can accurately restore color to digitial archive contents. Since we need to capture and manipulate many images to map onto 3D objects, the system should be practical from the viewpoints of portability of the image capturing devices, operation automation, and computational cost. Current color imaging systems like those using a digital still camera (DSC) are usually represented with the traditional red, green,

and blue (RGB) color model. Images captured by these systems have high resolution and high quality. However, the color model is not able to represent accurate color. The color of images captured with DSC is dependent on both the characteristics of the device and conditions of the illumination environment. For instance, it is almost impossible to accurately simulate colors of metamers with the RGB color model since, by definition, metamers are perceived as identical colors. Two metamers with different spectral reflectance have the same RGB properties under particular illuminations. Thus, humans who perceive the objects and the image produced by a DSC see these images as having identical colors. This phenomenon is called metamerism. This is a ubiquitous phenomenon that affects many areas of color imaging. For an accurate representation of color differences, we need to use a color-encoding method that is more accurate than the three-wavelength RGB method. For this reason, our method uses spectral information related to the target object.

Johnson and Fairchild [33] developed a color reproduction system using full-spectral rendering that was able to capture the differences beneath the phenomenon of metamerism. However, unlike spectral imaging, this system could not be applied to a texture image. There are many types of spectral imaging technology. A spectral imaging system may have two kind of cameras: a multispectral camera and a hyperspectral sensor. In order to obtain high spectral band data, the methods in [56, 23, 24] using a multispectral camera need a spectral reflectance database of target materials; hence, they restrict target objects. On the other hand, a hyperspectral sensor does not need that database and is able to obtain high resolution data. Gevers et al. [20] proposed computational methods for color constant identification of object colors through the analysis of spectral color data using hyperspectral data. However, the captured image was noisy and heavy. Moreover, image synthesis is computationally a very expensive process. Ikari et al. [29] proposed a method to map a spectral image onto an RGB image through a 3D object. However, in this method, the color accuracy depends on mapping accuracy. Thus, the operation is difficult.

In the process of creating digital archive contents, we needed to capture many textured images by DSC. Therefore, we focused on the idea of using both high resolution images captured by DSC and spectral information captured by a conventional spectrometer. Reinhard and Ahikmin [70] proposed a color transfer method between images, and in colorization, Levin et al. [49] added color to a monochrome image or movie using a segmentation method. In this study, we wanted to design a practical

method from the viewpoint of automation and computational cost. Therefore, we applied color calculated by spectral information to a segmentation image using the Normalized Cuts (NCuts) method [84], which was proposed by Shi and Malik as a graph-based way of segmenting images. This method is an unsupervised image segmentation method, and it can divide multiple segments stably and effectively. Other graph cut methods, such as lazy snapping [52] and grab cut [71], are fast and useful, but they only divide an image into bipartitions and need supervised information.

In this chapter, we describe a practical method to synthesize high resolution and accurate color images for digital archive contents. In our method, we assume the following. First, we use white reference to obtain illumination spectrum. Next, the target object is a diffuse object, and our target has 5 or 6 solid colors such as those found in a tumulus. Finally, we use the brightness of the DSC image to brighten the scene. In our experiment, we found that our method results in sufficient color restoration accuracy to produce an adequate value. Our method is also able to discriminate between metamers. Furthermore, our method was successful when applied to a 3D-textured digital model of archive contents.

2.2   Overview

The structure of this chapter is as follows. In section 2.3.1, we describe NCuts, and the segmentation of the DSC image. Next, we describe the color restoration algorithm using spectral information in section 2.4, and implementation of our method in section 2.5. Results of some experiments are presented in section 2.6, and we summarize this chapter in section 2.7.

2.3   Image Segmentation Using Normalized Cuts Method

We employ image segmentation using the NCuts method to apply spectral information into the DSC image effectively. In subsection 2.3.1, we describe the NCuts method. In subsection 2.3.2, we describe the segmentation of the DSC image. Furthermore, we use a slight improvement to divide the imaged DSC into multiple groups [17].

2.3.1   Normalized Cuts Method

The NCuts method is most closely related to the graph theoretic formulation of grouping proposed by Shi and Malik [84]. The set of points in an arbitrary feature space is represented as a weighted undirected graph $G = (V, E)$, where nodes V of the graph are the points in the feature space, and edges E are formed between every pair of nodes. The weight on each edge, $w(u, v)$, is a function of the similarity between nodes u and v. Here we partition a graph G into two joint sets, $A, B, A \cup B = V, A \cap B = \emptyset$, by simply removing the edges connecting the two parts. The degree of dissimilarity between these two pieces can be computed as the total weight of the edges that have been removed. In theoretic graph language, it is called the *cut*:

$$cut(A, B) = \sum_{u \in A, v \in B} w(u, v). \tag{2.1}$$

The optimal bipartition of a graph is the one that minimizes the value of the *cut*. Although there is an exponential number of such partitions, finding the minimum cut of a graph is a well-studied problem. Therefore NCuts is the normalized measure of disassociation.

The dissociation between the groups is given by

$$Ncut(A, B) = \frac{cut(A, B)}{assoc(A, V)} + \frac{cut(A, B)}{assoc(B, V)} \tag{2.2}$$

where $assoc(A, V) = \sum_{u \in A, t \in V} w(u, t)$ is the total connection from nodes u in A to all nodes in the graph and $assoc(B, V) = \sum_{u \in B, t \in V} w(u, t)$ is similarly defined. The *cut* of the groups is normalized for each total connection.

Next, Shi and Malik [84] stated that NCuts can be minimized by solving the generalized eigenvalue system as follows:

$$(D - W)y = \lambda D y. \tag{2.3}$$

Let D be an $N \times N$ diagonal matrix $D_j = \text{diag}(W(1, j), W(2, j), \cdots)$, $j = 1, 2, \cdots, N$, where N is the number of samples. W is an $N \times N$ symmetrical matrix with $W(u, v) = w_{u,v}$. We can transform the generalized eigenvalue system into a standard eigen system, and then rewrite Eq. (2.3) as

$$D^{-1/2}(D - W)D^{-1/2}z = \lambda z \tag{2.4}$$

where eigen vector z is $z = D^{1/2}y$. Solving Eq. 2.4, we use the eigen vector with the second smallest eigenvalue to bipartition the graph by finding the median value as the splitting point.

The NCuts method is able to segment more than bipartitions. One way is using the recursive 2-way cut, while another can use all of the top eigenvectors to simultaneously obtain a k-way partition. In this method, the n top eigenvectors are used as n dimensional indicator vectors for each pixel. We use this NCuts method for DSC image segmentation.

2.3.2   DSC Image Segmentation using Normalized Cuts Method

We divide a DSC image into color segments to use the NCuts method described in section 2.3.1. We create the feature vector as follows:

$$F(i) = [a_i^*, b_i^*, x_i, y_i], \quad i = 1, 2, 3, \cdots, N \tag{2.5}$$

where x and y are the horizontal and vertical positions of image pixels, N is the number of samples, and a^* and b^* are colors. Then our method uses the a^*b^* plane of the CIE1976LAB color space. This color space can represent the color perception of a human to Euclidean distance, and we do not use the L^* factor to exclude the possible effect of illumination. In the first step, a simple clustering algorithm, such as the k-means algorithm, is used to obtain an over-segmentation of the image into N groups. Setting the nodes of the graph decides the average points of N groups. Then, we calculate the weight on each edge w_{uv} between all the nodes u and v.

$$
w_{uv} = \exp\left(\frac{-\|I(u) - I(v)\|^2}{\sigma_I^2}\right) \times
$$
$$
\begin{cases}
\exp\left(\dfrac{-\|X(u) - X(v)\|_2^2}{\sigma_X^2}\right), & \text{if } \|X(u) - X(v)\|_2 < r \\
0, & \text{otherwise}
\end{cases}
\tag{2.6}
$$

where $I(u)$ and $I(v)$ are calculated from color values a^* and b^*. σ_I^2 is the variance of color distribution, and σ_X^2 is that of spatial distribution. Then, using edge weights w_{uv}, we calculate weight matrix W and diagonal matrix D.

Here we use a slight variation from a later paper by Fowlkes et al. [17]. In Eq. (2.4) $D^{-1/2}(D - W)D^{-1/2}$ is called the normalized Laplacian $\mathcal{L}$, and can be rewritten as follows:

$$\begin{aligned}
\mathcal{L} &= D^{-1/2}(D - W)D^{-1/2} = \\
&\quad I - D^{-1/2}WD^{-1/2}.
\end{aligned} \tag{2.7}$$

By Eq. (2.7), Eq. (2.4) is rewritten as

$$(D^{-1/2}WD^{-1/2})z = (1 - \lambda)z. \tag{2.8}$$

We can span a low dimensional space, of $E - 1$ dimensions, with the eigenvectors from the $E + 1$ least significant eigenvalues, where E is the partition number, and we ignore the least significant eigenvalue and the corresponding eigenvector. In the least significant space, all the input data have roughly same values due to the data normalization. We map the input data onto this low dimensional space.

$$y_{Eij} = \frac{z_{i+1,j}}{\sqrt{D_{jj}}}, \quad (i = 1, ..., E, j, ..., N,) \tag{2.9}$$

Finally, we can segment y_{Eij} into E clusters using the k-means method.

2.4   Color Restoration based on Spectral Information

The spectra obtained by a spectrometer depend on the illumination and object characteristics. Therefore, these spectra vary with a change in intensity and energy distribution of the light source, which are material characteristics. This problem is called color constancy. Our method has a solution of color constancy by spectral information using a white reference [20]. This color, which is invariant to illumination, is applied to the color of the DSC image. In this section, we describe how to calculate spectra under arbitrary illumination in subsection 2.4.1 and to restore a color based on spectral information into the color of a DSC image in subsection 2.4.2. In subsection 2.4.3, we describe how to find correspondences between the sensor spectral responses and the segmented images.

2.4.1   Illumination Color Change using Spectral Information

First, consider an opaque inhomogeneous dielectric object having diffuse reflection, and then the body reflection described by Shafer [83] as follows. Let $E(x, \lambda)$ be spectral power distribution of the incident light at the object surface at x, and let

$R(x, \lambda)$ be the spectral reflectance at the object surface at x. The spectral sensitivity of the k-th sensor is given by $S_k(\lambda)$. Then, the sensor response of the k-th channel $I_k(x)$ is given by

$$I_k(x) = G_B(x, n, s) \int_\lambda E(x, \lambda)R(x, \lambda)S_k(\lambda)d\lambda \qquad (2.10)$$

where λ denotes the wavelength, n is the surface normal, and s is the direction of the illumination surface. The integral is taken from the visible spectrum (e.g., 380-780 nm). The geometric term G_B denotes the geometric dependency on the reflection.

Second, a white reference has the reflectance of a perfect diffuser. This reflects all wavelengths of the light source and does not absorb any of them. Hence, a white reference has spectral reflectance $R^w(\lambda) \cong 1$. Furthermore, we assume that the surface normal n is equal to lighting direction s, then $G_B(x, n, s) = 1$. The sensor response of the matte white reflectance allows us to rewrite Eq. (2.10) as

$$I_k^w(x) = \int_\lambda E(x, \lambda)S_k(\lambda)d\lambda. \qquad (2.11)$$

In this way, the relative spectral power distribution of the white reference is measured.

Third, an object spectrum of an arbitrary sample is measured under the same illumination conditions. The k-th sensor response of a sample with respect to a white reference is given by

$$\frac{I_k(x)}{I_k^w(x)} = \frac{G_B(x, n, s) \int_\lambda E(x, \lambda)R(x, \lambda)S_k(\lambda)d\lambda}{\int_\lambda E(x, \lambda)S_k(\lambda)d\lambda}. \qquad (2.12)$$

Through the use of the spectrometer, the filters $S_k(\lambda)$ are narrow-band filters. Let the filter $S_k(\lambda)$ be modeled as a unit impulse that is shifted over N wavelengths, the transmission at $\lambda_k = \delta$ and zero elsewhere. This allows us to rewrite Eq. (2.12) as

$$\frac{I_k(x)}{I_k^w(x)} = \frac{G_B(x, n, s)E(x, \lambda_k)R(x, \lambda_k)}{E(x, \lambda_k)} \qquad (2.13)$$

obtaining

$$\frac{I_k(x)}{I_k^w(x)} = G_B(x, n, s)R(x, \lambda_k). \qquad (2.14)$$

Finally, the target color spectra $I_k'(x)$ are the product of Eq. (2.12) and the sensor response $I_k^{w'}(x)$ of the white reference under an arbitrary illumination. The equation is as follows:

$$I'_k(x) \;=\; \frac{I_k(x)I^{w'}_k(x)}{I^w_k(x)} \;=\;$$
$$G_B(x, n, s)E'(x, \lambda_k)R(x, \lambda_k)S'_k(\lambda_k) \qquad (2.15)$$

where $S'_k(\lambda_k)$ denotes the arbitrary spectral sensitivity of the k-th sensor. According to Eq. (2.12), the color itself depends on spectral reflectance whereas the brightness of the color depends on factor $G_B(x, n, s)$. However, since our method uses the brightness of the DSC image, then we assume that $G_B(x, n, s)$ corresponds to the brightness of the DSC image.

2.4.2　Combining Spectral Information and the DSC image

We calculate CIE tristimulus value CIEXYZ from sensor response $I'_k(x)$ in Eq. (2.15). Here, we measure the color in point of object surface by a spectrometer. Therefore, the color pixel x denotes color region $m = 1, 2, \cdots, N$, where N is the number of color regions. Also, the spectral sensitivity of the k-th sensor $S'_k(\lambda_k)$ is changed into CIE RGB color matching functions $\bar{x}(\lambda_k), \bar{y}(\lambda_k), and \bar{z}(\lambda_k)$. Using Eq. (2.15), this equation is as follows:

$$X_{sp}(m) = K \int_{\lambda_k} E'(m, \lambda_k)R(m, \lambda_k)\bar{x}(\lambda_k)\mathrm{d}\lambda_k$$
$$Y_{sp}(m) = K \int_{\lambda_k} E'(m, \lambda_k)R(m, \lambda_k)\bar{y}(\lambda_k)\mathrm{d}\lambda_k \qquad (2.16)$$
$$Z_{sp}(m) = K \int_{\lambda_k} E'(m, \lambda_k)R(m, \lambda_k)\bar{z}(\lambda_k)\mathrm{d}\lambda_k$$

$$K = \frac{100}{\int_{\lambda_k} E'(m, \lambda_k)\bar{y}(\lambda_k)\mathrm{d}\lambda_k} \qquad (2.17)$$

where K is a coefficient to normalize Y_{sp} to 100. Next, we calculate color differences, $CIE\Delta E^*_{ab}$, from target color $X_{sp}(m), Y_{sp}(m), Z_{sp}(m)$ and the average of segmented image color $X_{img}(m), Y_{img}(m), Z_{img}(m)$. Using the method of subsection 2.4.3, we can find correspondences m of target colors and color segment images. In our method, the brightness of the target color coincides with the brightness of the segmented image.

The equation is as follows:

$$
\begin{aligned}
X_{sp}(m) &= X_{sp}(m)\frac{Y_{img}(m)}{Y_{sp}(m)} \\
Y_{sp}(m) &= Y_{img}(m) \\
Z_{sp}(m) &= Z_{sp}(m)\frac{Y_{img}(m)}{Y_{sp}(m)}.
\end{aligned}
\tag{2.18}
$$

The transform vectors $X_t(m)$, $Y_t(m)$, and $Z_t(m)$ to apply the target color to the segmented image are given by

$$
\begin{aligned}
X_t(m) &= \frac{X_{sp}(m)}{X_{img}(m)} \\
Y_t(m) &= 1.0 \\
Z_t(m) &= \frac{Z_{sp}(m)}{Z_{img}(m)}.
\end{aligned}
\tag{2.19}
$$

Finally, the transform vectors $X_t(m)$, $Y_t(m)$, and $Z_t(m)$ are multiplied by all the pixels of the segmented image $X_{img}(x)$, $Y_{img}(x)$, and $Z_{img}(x)$.

$$
\begin{aligned}
X'_{img}(m) &= X_{img}(x)X_t(m) \\
Y'_{img}(m) &= Y_{img}(x) \\
Z'_{img}(m) &= Z_{img}(x)Z_t(m).
\end{aligned}
\tag{2.20}
$$

When all the segmented images are synthesized, the result is transformed into RGB color.

2.4.3 Finding correspondence of the spectral information and segmented image

We need to find the correspondence between the spectral sensor response and segmented image so that their color difference is minimized. Therefore, we calculate the color difference, $CIE\Delta E^*_{ab}$, from the spectral sensor response and the average color of the segmented image. This is calculated from a^* and b^* color values in the CIELAB color space. The equation is as follows:

$$
\Delta E^*_{ab} = \left[(a^*_{sp} - a^*_{img})^2 + (b^*_{sp} - b^*_{img})^2\right]^{1/2}
\tag{2.21}
$$

where a^*_{sp} and b^*_{sp} denote a^* and b^* values of the spectral response, a^*_{img} and b^*_{img} are a^* and b^* values of the average of the segmented image. Finding the smallest sets, we can find correspondences between spectral sensor responses and segmented images.
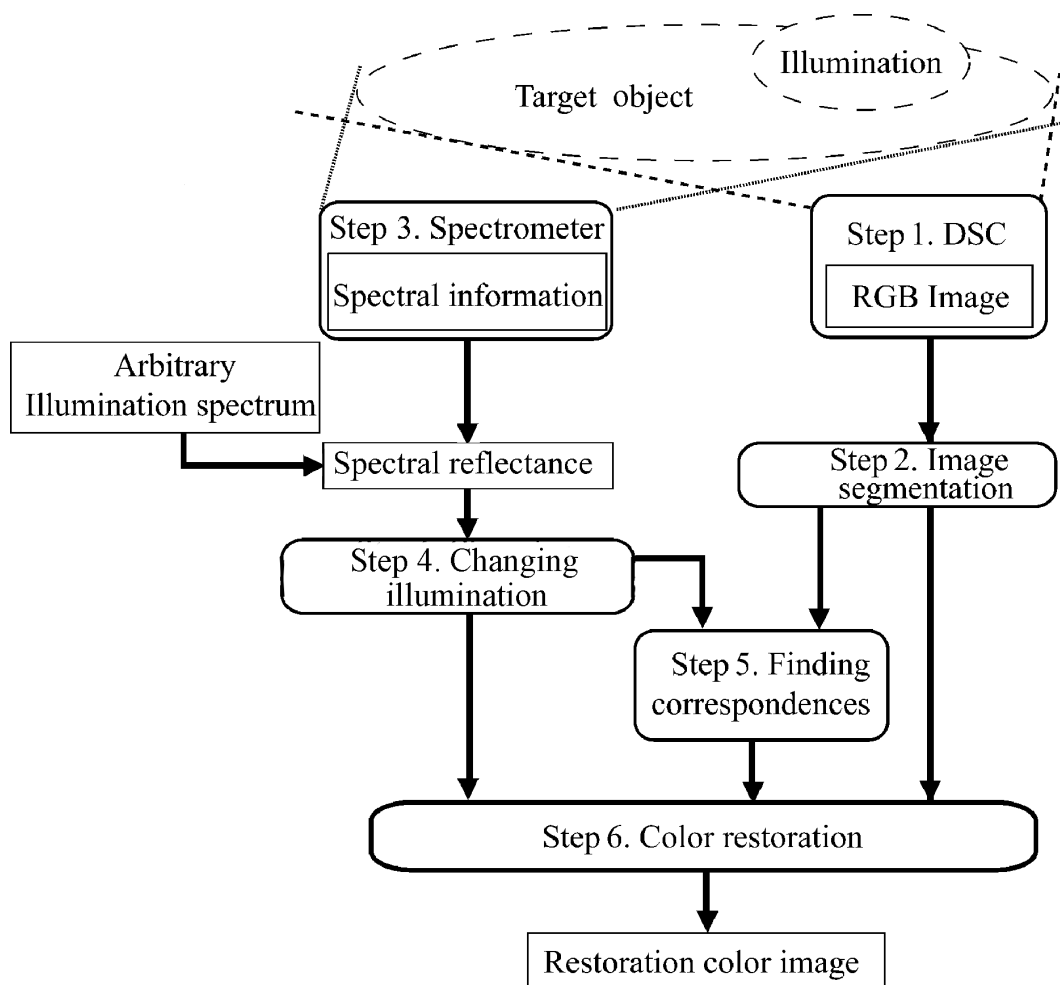
Figure 2.1: System process

2.5   Implementation

Fig. 2.1 shows the process of our proposed system. The system consists of the following steps.

Step 1. Obtain a high resolution RGB image using a DSC.

Step 2. With image segmentation technique by the Normalized Cut method, divide the DSC image into segments for each color. Here, using color space without brightness as the feature space, we can segment the brightness invariant color of the object visually.

Step 3. Measure the spectral information by a spectrometer, specifically identify the spectral power distribution (SPD) of each color on a target object and the illumination spectrum by a white reference. Here, our method allows the environments of measuring spectral information and capturing a DSC image to be different.

Step 4. Spectral reflectances are calculated from the object's spectra and illumination spectrum. Target colors are calculated from the spectral information and arbitrary illumination spectrum.

Step 5. Find correspondences of color segments and target colors as described in subsection 2.4.3.

Step 6. Target colors are applied to each segment image. Here, our method uses brightness from the image.

In this way, we are able to obtain high resolution and accurate color images efficiently.

Nikon D1-X   SpectraScan PR-650

Figure 2.2: Equipment

2.6 Experiments and Results

In this section, we describe three experiments we have conducted, verification of color restoration, accuracy color restoration of metamers, and application to digital archive contents. All experiments were performed using a DSC (Nikon D1-X), spectrometer (SpectraScan PR-650), and white reference (PhotoResearch SRS-3). Fig.
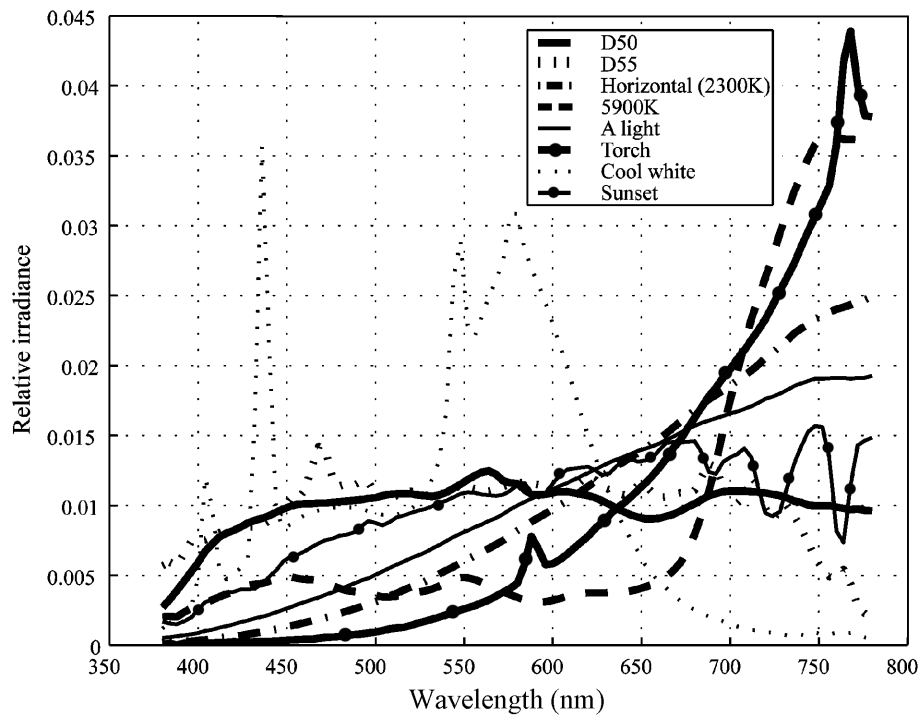
Figure 2.3: Illumination spectra

2.2 shows the equipment of our system. In these experiments, we used lights as follows: D55 Light (day light 5500K :SERIC XC-100) and A light (tungsten light 2848K), cool white (fluorescent lamp), horizontal (2300K), D50 in (day light 5000K: Sakata Inx Corporation SpectraLight III), real torch light, real sunset light, and incandescent light (5900K: PSR500WD). These illumination spectra are shown in Fig. 2.3.

2.6.1   Verification of Color Restoration Accuracy

In this experiment, we evaluated the color restoration accuracy of our method. We selected a target object that consists of five colors and has no specular reflection. First, we captured a target image under the D55 light. Simultaneously, we measured the spectral power distribution of colors of an object surface and a white reference using a spectrometer. We changed the color of the DSC image into the color under target illuminations by our method, where target illuminations were a light, cool white, and horizontal, described in the previous section.

Notice that the color of the output image Figs. 2.4. c, d, and e at left is similar

to that of ground truth Figs. 2.4. c, d, and e at right. However, our method uses brightness from the image. Thus, the brightness of the object does not correspond. Table 2.1 shows the color differences, $\Delta E_{a^*b^*}$, between ground truths and restoration colors. Here, the ground truth of the target spectra is measured under several illuminations, and restoration colors are estimated values in the CIELAB color values. Notice that the average of the color differences, $\Delta E_{a^*b^*}$, between ground truths and restoration colors is less than 1.08 in the target object. Generally, in human vision, the color difference that enables us to discriminate between two colors is more than about 3.0.

2.6.2   Color Restoration of Metamers

In this section, we describe the color restoration of metamers using our method. If two different surfaces look the same when viewed under a particular illumination, then they are called metamers, and this phenomenon is called metamerism. Using the RGB color model, we are not able to restore the color of metamers because the metamers have different spectral reflectances. However, if we calculate restoration color based on spectral information, we are able to restore the color of metamers under arbitrary illumination. In this experiment, we tried to restore the color of metamers under several illuminations. Fig. 2.5 shows pictures of metamers (GATF/RHEM light indicator strips) under two illuminations. Under D50 illumination in Fig.2.3, we are not able to see stripes. However, stripes are visible when the strip is viewed under other lighting, such as incandescent 5900K. Fig. 2.6 shows spectral reflectance of the metamers. Fig. 2.7 shows simulated color under each illumination using spectral information about the metamers. Viewed under a A light, and a torch lighting conditions, the different metamers appear to be a solid color.

	Purple	Green	Skin	W and B	Average
A	0.282301	0.438471	0.968805	0.20786	0.474359
Cool White	0.788768	1.460883	1.895176	0.20272	1.086887
Horizontal	0.245402	0.284683	1.096399	0.33352	0.490001

Table 2.1: Color difference ($\Delta E_{a^*b^*}$) between restoration colors and ground truths

(a)Input image   (b)Segmented image

Output image   Ground truth
(c) A Light

Output image   Ground truth
(d) Cool White(fluorescent lamp)

Output image   Ground truth
(e) Horizontal
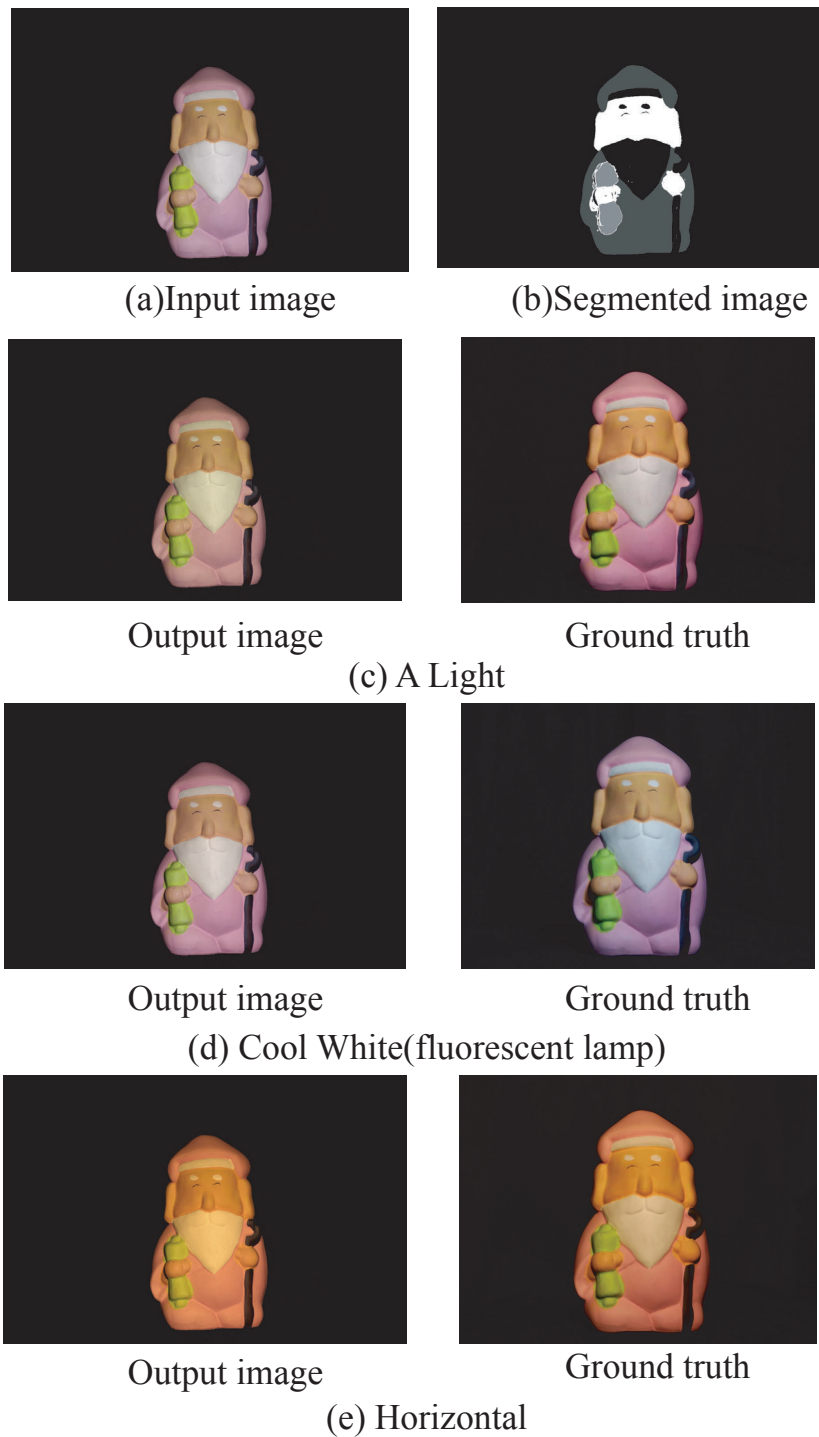
Figure 2.4: Output image and ground truth. (a) Input image; (b) Segmentation result by NCuts method; (c),(d), and (e) left column: simulated image under each light by our method; (c), (d), and (e) right column: captured image under each light.

(a) D50 illumination

(b) 5900K(PSR500WD)

Figure 2.5: Light indicator strips under D50 (left) and 5900K (right). Viewed under 5000K or D50 standardized lighting conditions, light indicator strips will appear to be a solid color.
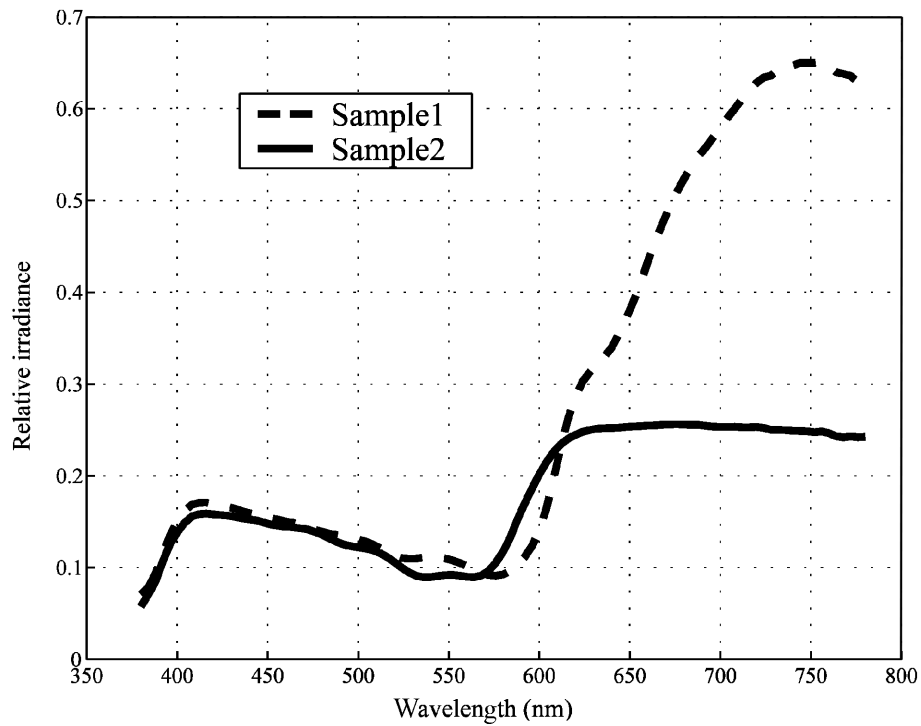
Figure 2.6: Spectral reflectance of metamers. These spectra are obtained from light indicator strips.

2.6.3 Application to Digital Archive Contents

We made digital archive contents to evaluate the practicality of our method. Benkei-ga-ana tumulus is an ancient tomb in Japan, made late in the 6th century. Several wall paintings resembling ships and horses were painted by ancient artists in this tumulus.

Notice that part of the red pigment can be extracted, as shown in Fig. 2.8~2.9.
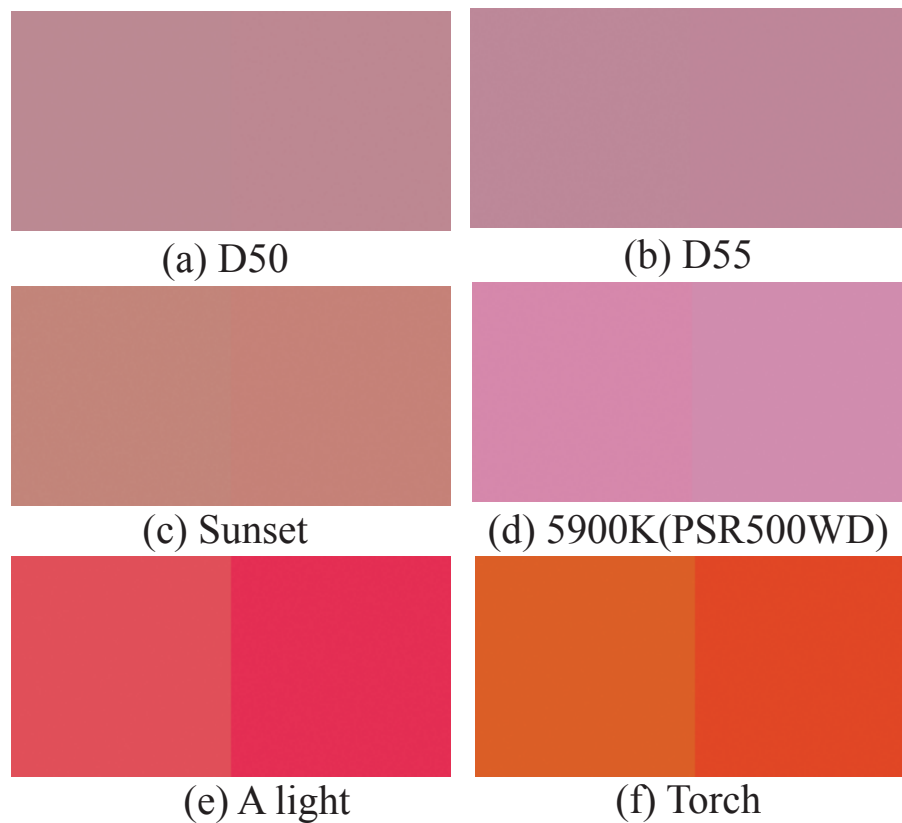
Figure 2.7: Simulated colors under different illuminations using spectral reflectance of light indicator

This object has an ambiguity of boundary caused by degradation of the wall painting. For this reason, we configured the parameter of NCuts to decrease the contribution of spatial distribution σ_X in Eq. (2.6) and increase the number of segments. The clear boundary of each segment cannot be observed, but we can extract relatively accurate pixels in the parts of the pigments in Fig. 2.8~2.9.

Color transformation error could hardly be observed in Fig. 2.11. However, we show the effect of segmentation error in Fig. 2.12. Fig.2.12. a is an example of incorrect segmentation due to an increase of the contribution of spatial distribution parameter σ_X. Fig. 2.12. c is an image simulated using Fig. 2.12. a under D65 illumination. Fig. 2.12. b is an image simulated using the correct segmentation result under D65 illumination. In Fig. 2.12. c, notice that in a section of rock, the incorrectly segmented pixels turn red or pink. This effect may occur frequently when the target object contains complicated colors.

Fig. 2.10 shows the result of comparison between the k-means method and the

(a) Input image   (b) Segmented image
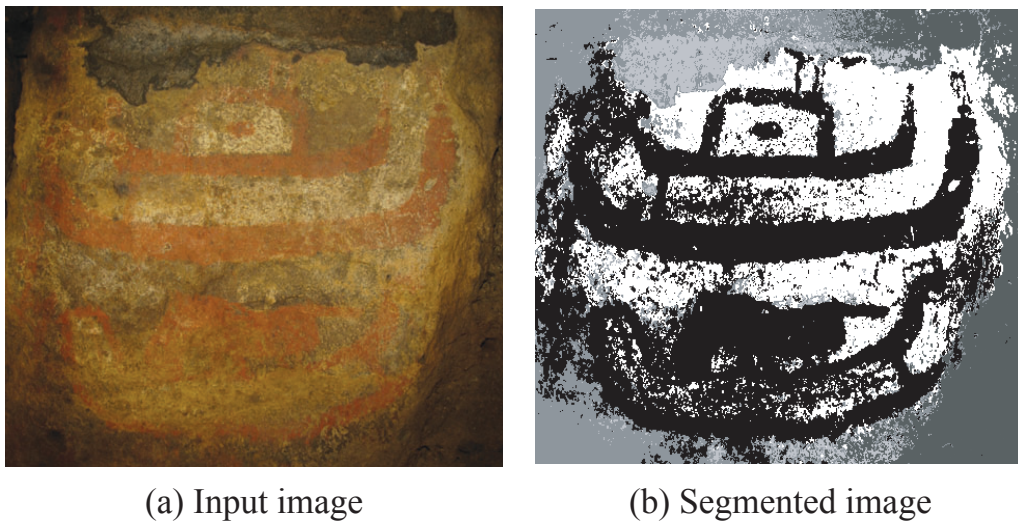
Figure 2.8: Image segmentation result 1 of a wall painting in Benkei-ga-ana tumulus using the NCuts method

(a) Input image   (b) Segmented image
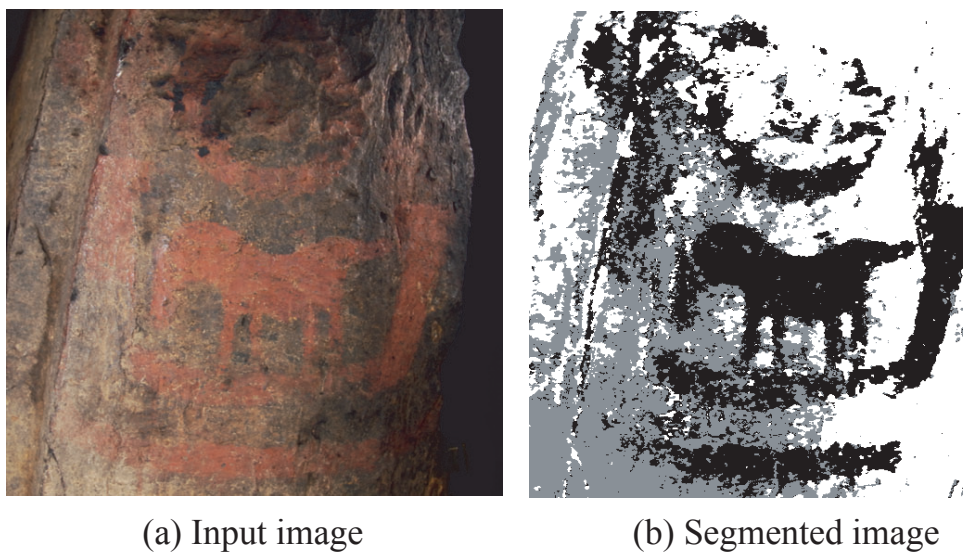
Figure 2.9: Image segmentation result 2 of a wall painting in Benkei-ga-ana tumulus using the NCuts method

NCuts method. The hyperplane of k-means is a straight line, while the hyperplane of NCuts is a curved line. This result shows that NCuts can handle the mixture of pigment and rock. Using NCuts, we can obtain a stable solution for wall painting.

Archaeologically, we have a question as to how the artists painted the wall painting. We do not know whether they painted in daylight or using torch illumination.

(a) Input image   (b) a*b* plot

(c) kMeans
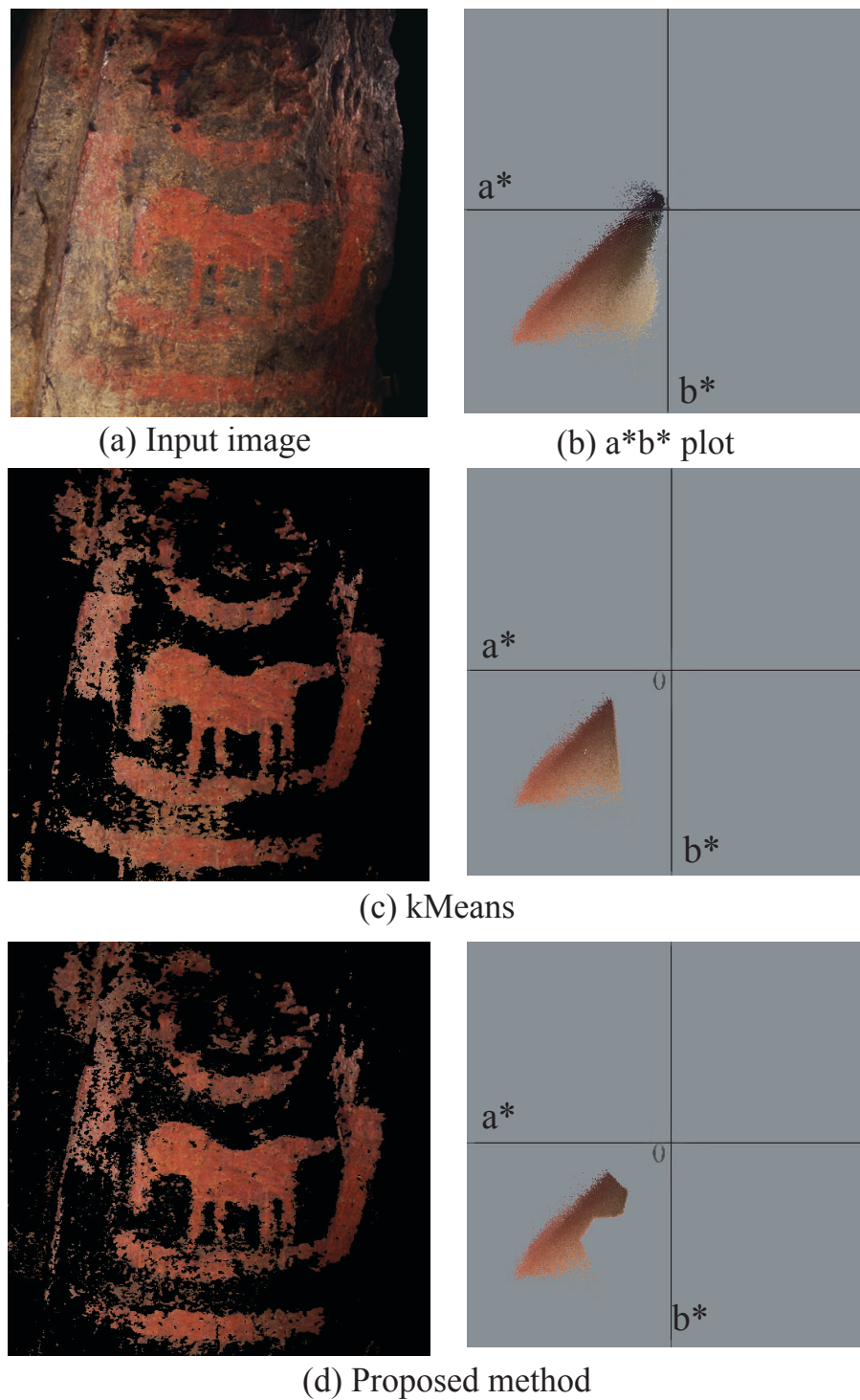
(d) Proposed method

Figure 2.10: Comparison of k-means and NCuts: The hyperplane of the proposed method is a curved rather than a straight line.

In Fig. 2.11, we are able to discriminate difference of colors under D65 (CIE daylight 6500K); however, under torch illumination, it is difficult for us to discriminate the color difference. Therefore, our assumption is that the artists made the wall paintings under D65 illumination. Fig. 2.13 ~ 2.16 shows the application of our method to digital archive contents. We restored more than 80 texture images in a content. Also, we found it possible to map the color restoration images onto 3D geometry by laser range sensor. This application behaves like virtual reality: we can interactively operate the viewpoint and change the illuminations.

(a) Input image   (b) Torch illumination   (c) D65 illumination

Figure 2.11: Color restoration of an image in the Benkei-ga-ana tumulus. (a) DSC captured image; (b) Simulated image under torch illumination; (c) Simulated image under D65 illumination

(a)   (b)   (c)
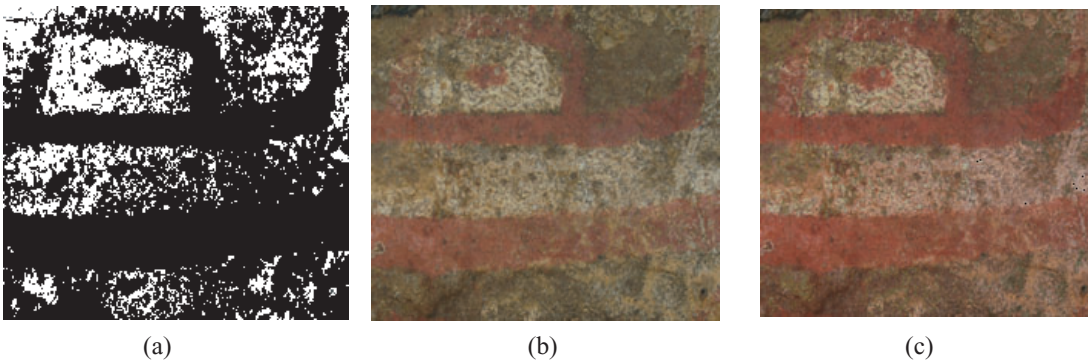
Figure 2.12: The effect of segmentation error. (a) Incorrect segmentation result; (b) Correct restoration color image; (c) Incorrect restoration color image

2.7　Summary

We proposed a practical color restoration method based on spectral information. Using our method, we are able to obtain high resolution and accurate color images. DSC images and spectral information can be obtained under different environments. We do not need to obtain these data simultaneously. For example, we are able to obtain images under arbitrary illumination. Also, we can share our database of spectral reflectance with archaeologists.

In our experiment, color restoration accuracy was sufficient only in the case of a diffuse object. Our method was also able to represent the phenomenon of metamerism. For this reason, our method can synthesize sufficiently accurate texture images. Moreover, image segmentation using the NCuts method worked well for making digital archive contents. Thus, we further applied our method to digital archive contents, which were showed in the Kyushu national museum, and were able to realize textured images.

(a)

(b)

Figure 2.13: Digital archive contents of Benkei-ga-ana tumulus 1 (a) Simulation of color appearance under D65 light (b) Simulation of color appearance under torch light

(a)

(b)

Figure 2.14: Digital archive contents of Benkei-ga-ana tumulus 2 (a) Simulation of color appearance under D65 light (b) Simulation of color appearance under torch light
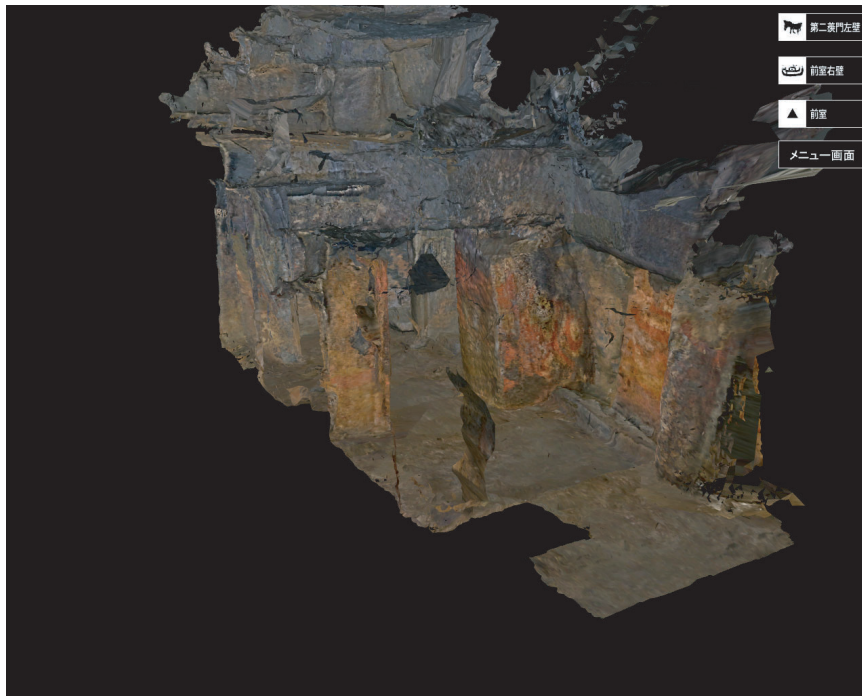
(a)

(b)

Figure 2.15: Digital archive contents of Benkei-ga-ana tumulus 3 (a) Overview of Benkei-ga-ana tumulus. (b) Entrance of Benkei-ga-ana tumulus.
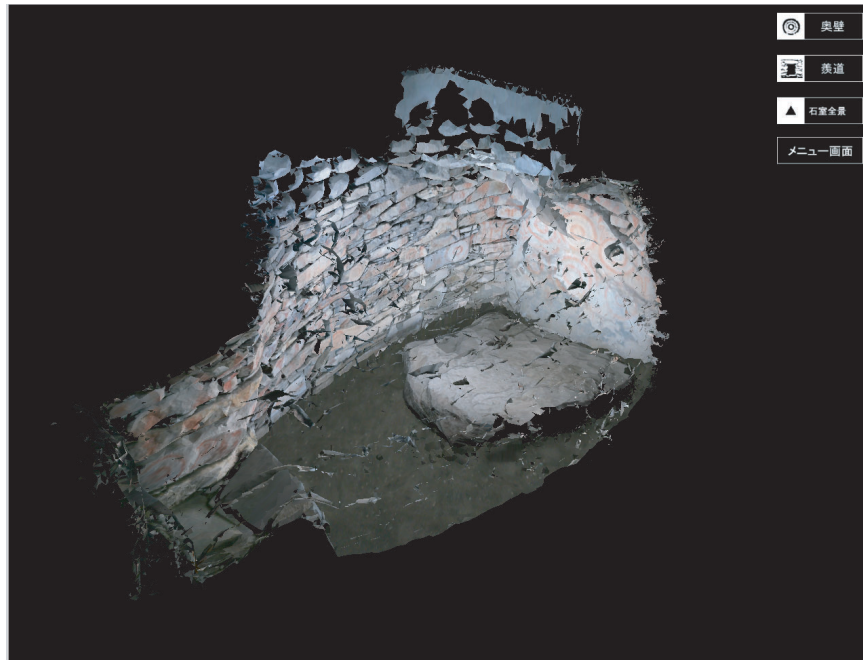
(a)

(b)

Figure 2.16: Digital archive contents of Hinooka tumulus 4 (a) Overview of Hinooka tumulus. (b) Entrance of Hinooka tumulus.

Chapter 3

Multispectral Imaging for Material Analysis in an Outdoor Environment Using Normalized Cuts

Multispectral imaging has promising and wide application areas, including medical imaging, remote sensing, and cultural asset preservation. In particular, cultural assets are often damaged by microorganisms such as moss and mold. Thus, asset preservation requires measuring the kinds and extent of microorganisms by obtaining spectral information in wide areas. This process requires developing an efficient spectral sensing system that can obtain data for wide areas as well as segmentation methods to identify those locations. This chapter describes a new multispectral imaging system applicable to wide areas. Our design allows the system to have a wide field of view of high resolution with low noise and negligible distortion. We can apply this system to measuring the surface spectrum on an object surface in an outdoor environment. For determining the distribution of microorganisms, we developed a multispectral image segmentation method using the data obtained by our system. Finally, we applied our system and segmentation method to the data from the bas-relief of the Bayon Temple in the Angkor ruin, and we identified the classes and distribution areas of the microorganisms.

3.1   Introduction

Spectral reflectance is inherent in the nature of objects. Different materials have different spectral reflectance. Object analysis based on this fact has been conducted in many fields, such as medical imaging, agriculture, remote sensing, and archaeology, to name a few. For example, the Digital Bayon Project [31], which digitizes the shape and surface reflectance of the Bayon Temple in the Angkor ruin for preservation and deterioration prevention, needs to determine what kind of microorganisms are present and how widely they exist over the structural surfaces. This involves the analysis of spectral reflection distribution of microorganisms living on the bas-relief of the Bayon Temple.

For the efficient analysis of spectral distribution over an object surface, a two-dimensional spectral image acquisition system is desirable. Traditional spectral cameras provide spectral data only from a limited area, often from a spot. It is difficult, if not impossible, to cover the entire surface of the bas-relief, whose size is 800m x 4m, located in the inner corridor of the temple. This is one of the motivations for us to develop an efficient, handy, and yet high-resolution spectral imaging system. The requirements of the system are: 1) to cover a wide area for efficient measurement to be able to determine distribution of microorganisms, 2) to be able to ignore variations of illumination conditions in dramatic weather changes from bright sunshine to dark squall, and 3) to design a handy system that can be transported to a deep jungle.

In the color reproduction field, the so-called multiband camera system has been developed to perform cross-environment color reproduction for an object surface [23, 112]. The reflectance spectra of an object surface are acquired in this imaging system for calculating the trichromatic color values under arbitrary illumination of the surface. The multiband camera usually employs five or more color filters in order to reproduce accurate colors across various illumination environments. Typically, the rotating filters are mounted in front of a monochromatic CCD camera [56, 112]. This type of system is easy to handle, but it cannot obtain a continuous spectrum distribution of an object surface.

Hyperspectral sensors are used in the aerial remote sensing field [46, 54, 43]. Such systems can obtain a multispectral image by scanning the scene in one-pixel increments along the x-axis. The multispectral image that is obtained has a high spectral resolution and wide field of view. However, it has low image quality due to blurring, lack of focus, and distortion caused by a moving platform.

We developed a new multispectral imaging system using a Liquid Crystal Tunable Filter (LCTF) [98], mounted on an automatic pan/tilt platform. Compared to conventional systems, our system has not only high image quality with sufficient spectral resolution but also a wide capturing angle for efficient sampling.

Preservation of cultural assets involves challenges to spectrum measurement. Cultural assets are often in severe outdoor environments, such as the environments of the pyramids in Egyptian desert or the Angkor ruin in Cambodian jungle. In an outdoor environment, wide alterations in the illumination environment often occur quickly. Fixed exposure of a system causes saturation and underexposure. To tackle these problems, we developed a measuring method that can estimate optimum exposures based on noise analysis of the system.

Preservation of cultural assets also needs to determine not only the kinds of microorganisms that exist but also how widely they are spread and how much they mix with each other. This requires us to segment the multispectral images into spatial segments corresponding to the distribution of these microorganisms.

Segmentation is conducted based on subspace data. Segmentation should be done based on multispectral data in high-dimensional data space. However, previous research has demonstrated that high-dimensional spaces are mostly empty, indicating that the meaningful data exist primarily in a subspace. It is necessary for us to find the optimal subspace, depending on the class of spectrum given by the microorganisms to be handled, without losing the original information that allows for their separation. In other words, determining the distribution of microorganisms requires bringing data from a high-order dimension to the optimal low-order dimensional space by overcoming the "curse of dimensionality [13]."

One of the most widely used dimension reduction techniques is principal component analysis (PCA). PCA computes orthogonal projections that maximize the amount of data variance, and yields a dataset in a new uncorrelated coordinate system. However, most cultural assets have complicated surfaces with interreflection, absorption, and scattering. Moreover, there is a color mixture between the top layer of the microorganisms and the bottom layers of asset surfaces. Unfortunately, PCA, a linear dimension reduction method, cannot handle such nonlinear effects.

We propose an effective dimension reduction method by using Normalized Cuts (NCuts) [84], a class of nonlinear dimensional reducers. NCuts methods are widely used as segmentation methods for RGB images in computer vision, but they are not used for multispectral image segmentation in general. NCuts methods are conve-

nient in reducing dimension in a nonlinear manner, and simultaneously segmenting the data. One difficulty in applying NCuts method to our problem is the necessity of a huge memory space ($N \times N$) for creating an affinity matrix. We solve this issue by applying a local linear approximation [3], by assuming local linearity on the tangential space of a global manifold space in the high dimension.

The specific contributions of our work are to propose a multispectral image acquisition technique for obtaining panoramic multispectral images, and to develop a segmentation method to handle global nonlinear dimensional reduction. This chapter confines our application to microorganism classification for asset preservation, but the method itself can be used for other applications.

3.2   Overview

The structure of this chapter is as follows. Section 3.3 describes our hardware design for panoramic multispectral imaging and capturing techniques of data acquisition for cultural assets. Section 3.4 derives a nonlinear dimension reduction method using the "kernel trick" and NCuts method, and applies the NCuts segmentation to a multispectral image. In section 3.5, we evaluate our methods and demonstrate the application for analyzing microorganisms on the bas-reliefs of the Bayon temple. Finally, we summarize the chapter in section 3.6.

3.3   Acquisition of a Multispectral Image

We developed a novel multispectral imaging system that has a wide view angle, high image quality, and an accurate spectrum. The system can efficiently measure a target object in an outdoor environment. In subsection 3.3.1, we describe the hardware construction of our system. In subsection 3.3.2, we describe the technique for capturing images in an outdoor environment. In subsection 3.3.3, we describe reconstruction of each band of images having different configurations, and how to stitch a multispectral image.

3.3.1   Panoramic Multispectral Camera

Our multispectral imaging system has been designed to be a handy system with spectrum accuracy in each pixel with a wide view angle. The system consists of a

small monochromatic CCD camera with a liquid crystal tunable filter (LCTF), shown in Fig. 3.1, mounted on an automatic pan/tilt platform (CLAUS Inc. Rodeon VR head). The LCTF (CRI Inc. Varispec) is an optical filter that allows the wavelength of the transmitted light to be electronically adjusted. The monochromatic CCD camera (Sony XCD-X710) with the LCTF mounted can obtain a series of two-dimensional spectral images by repeatedly changing the LCTF's transmittable wavelength with image acquisitions. The captured image has high image quality without distortion. The LCTF capturing system has a narrow field of view because the LCTF is mounted in front of the lens. We compensate for this problem by using an automatic panorama pan/tilt platform. The system captures a wide view multispectral image by synchronizing these three devices efficiently.

3.3.2   Estimation of Adaptive Exposure in an Outdoor Environment

The optimal exposure time is necessary to be determined in each wavelength due to the two reasons: uneven characteristics and varying illumination conditions. A multispectral imaging system using LCTF generally needs a fixed exposure time over the entire range of wavelengths for comparing pixel intensities over all wavelengths. However, the spectral sensitivity given by the combination of LCTF and monochromatic camera is very low in short wavelengths (e.g., 400-500 nm), as shown in Fig. 3.2.(a), and relatively high in other wavelengths. If the pixel intensity at a certain wavelength would be smaller than the dark current noise, we would not be able obtain a meaningful measurement at that wavelength. For instance, Fig. 3.2.(b) shows a measured spectrum under dark illumination. Longer exposure time is necessary for spectral accuracy with wavelengths from 400 nm to 500 nm than for other wavelengths.

Varying illumination conditions occur in an outdoor environment, in which many cultural assets are located. Our sensor samples spectral data by changing the LCTF's filtering characteristics and samples a series of images along the wavelengths. During this sampling period, it often occurs that the illumination condition varies due to the movement of clouds. If the intensity of illumination dramatically varies during measurement, it would induce saturation or underexposure at certain wavelengths. The dynamic determination of optimal exposure time at each wavelength is necessary for adjusting the effects of varying illumination conditions.
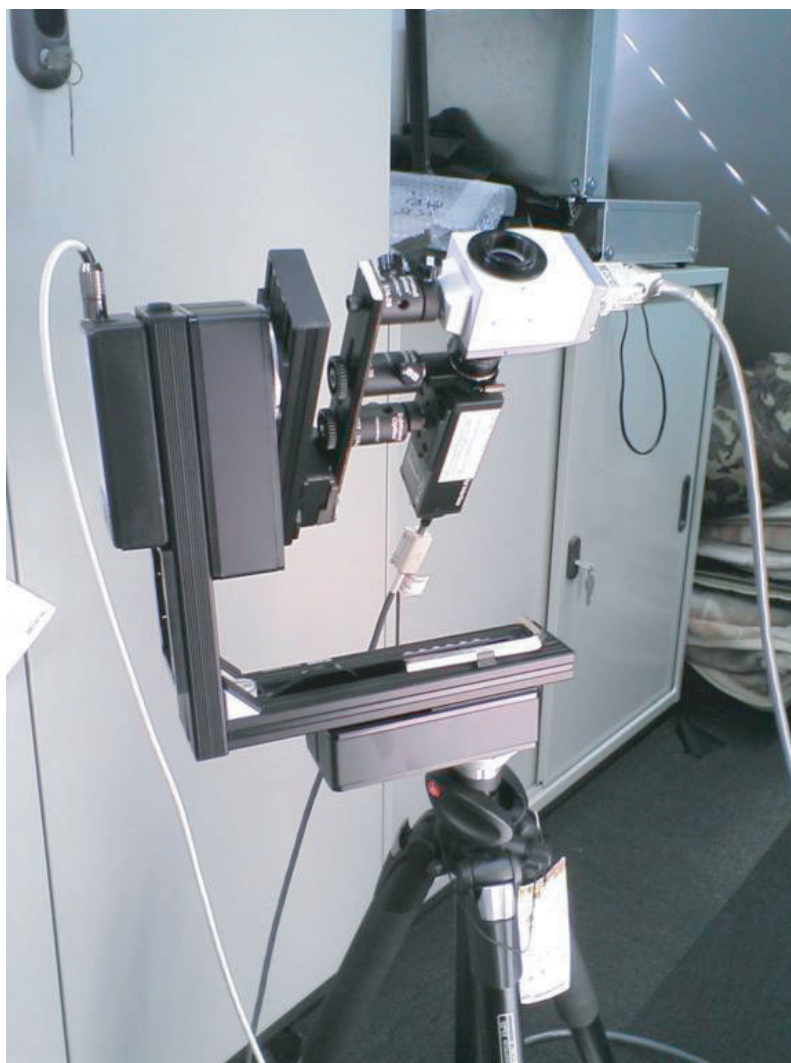
Figure 3.1: Panoramic multispectral imaging system

We attempt to estimate an optimal exposure time for each wavelength based on noise analysis [69]. The noise can be categorized into signal-dependent noise and signal-independent noise (SIN). In this system, we mainly consider the effect due to the signal-independent noise, since the signal-dependent noise is negligible compared with signal-independent noise. The signal-independent noise is composed of fixed pattern noise (FPN) and read-out noise, and photo response non-uniformity (PRNU). FPN is a dark current noise, a dynamic component. The read-out noise is composed of the reset noise, amplifier noise, and quantization noise. We focus on the FPN and the read-out noise, since PRNU is a static component easily calibrated in the initial stage.
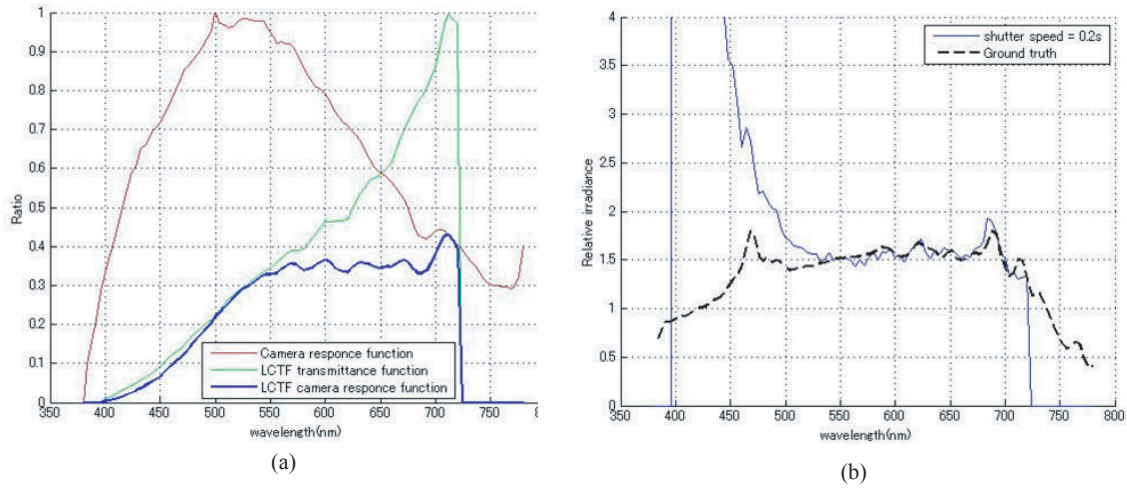
Figure 3.2: (a) Spectral sensitivity function of monochromatic CCD camera and LCTF transmittance function (b) Illumination spectrum when the exposure time in all bands is fixed.

The FPN depends on the temperature and the exposure time. Here, we assume that the sampling time is reasonably short, say 5 to 10 min, so that the temperature can be considered as constant. The FPN has a linear relation with the exposure time as shown in Fig. 3.3. The linear relation can be expressed as follows: $\epsilon_{DC} = at + b$, where t is an exposure time, a is the amount of the FPN increase depending on exposure times, and b is the amount of the FPN with zero exposure time at that particular temperature. These values are measured at the site before sampling from a series of images with various exposure times while the lens is covered with a cup.

The read-out noise appears randomly at pixel positions at each image. We model the read-out noise as a Gaussian distribution at each pixel. In order to evaluate the parameters of the Gaussian distribution, we obtain a series of lens-covered images, and we calculate mean and standard deviation values. The mean value of images ϵ_{DC} are the FPN, and the standard deviation value of images ϵ_R are read-out noise. We use the upper bound of the SIN as $\epsilon_{DC} + \epsilon_R$.

Based on the discussion of the noise analysis, we design the procedure to determine the optimal exposure time at each wavelength. The procedure consists of two parts. The first part finds the exposure time that gives the brightest image of a white reference while avoiding saturation over all wavelengths. The second part determines any wavelength that gives lower value in the white reference than the SIN upper boundary, and, if this wavelength exists, it increases the exposure time
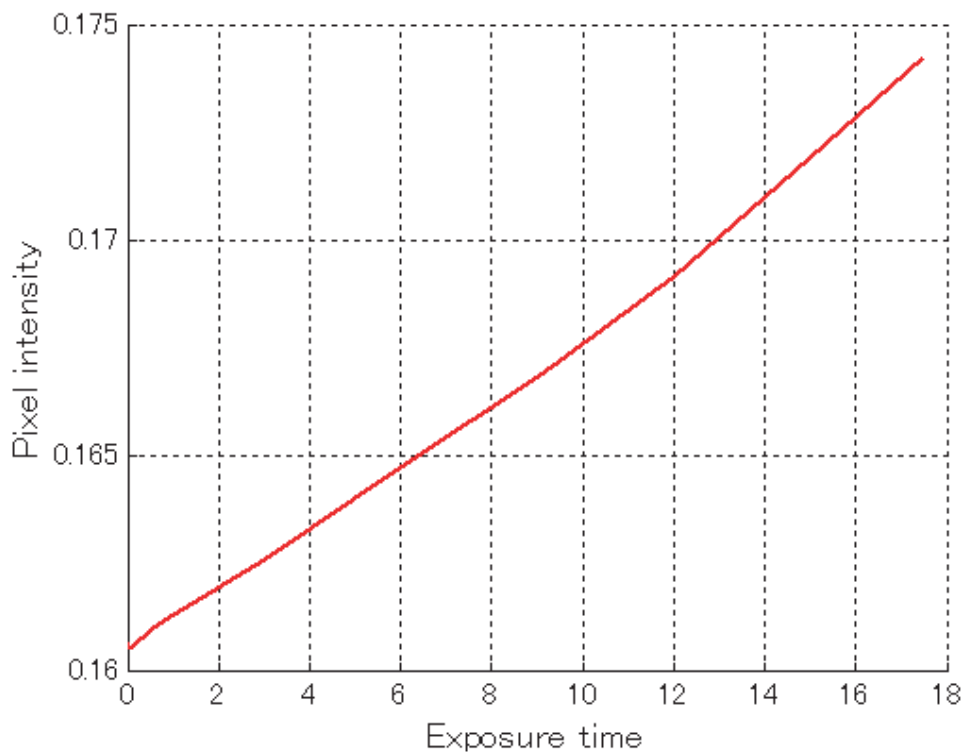
Figure 3.3: The correlation between the FPN and exposure time.
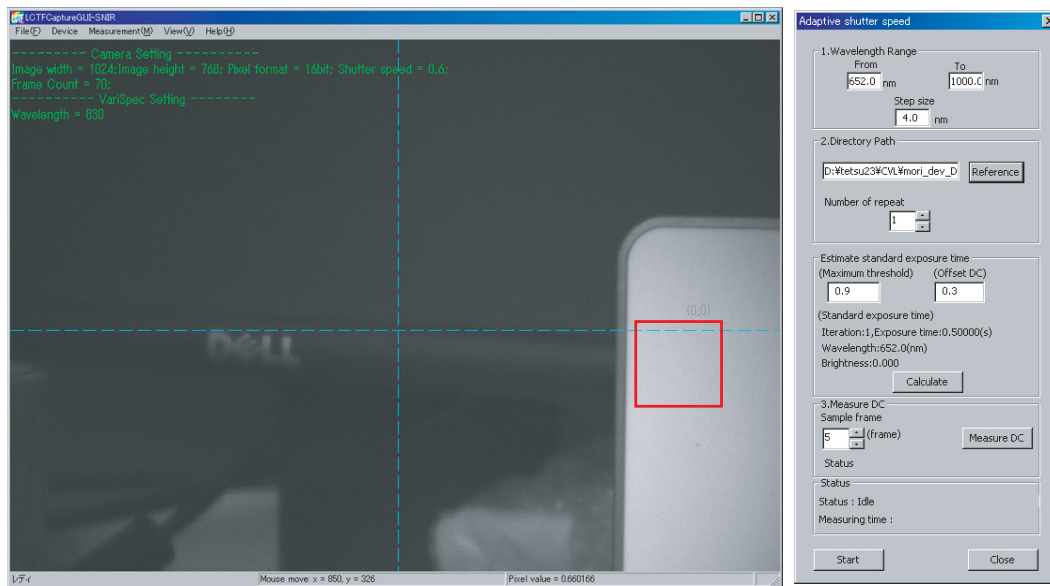
Figure 3.4: GUI of panoramic multispectral imaging system.

while avoiding saturation.

The first part consists of:

Step 1. Select the brightest area ($m \times n$) on a white reference at each wavelength, λ, as shown in Fig. 3.4, and obtain the average brightness within the window, $L(\lambda)$. Repeat this step over all wavelengths

Step 2. Obtain the maximum value, L_{max}, among all the brightness values over all wavelengths.

Step 3. Determine the standard exposure time t_s as the longest exposure time when all the values in the brightest area found in Step 1 are not saturated. Namely, $L_{max} < 2^{16}$.

The second part rescues the particular wavelength image buried under the noise level. For this, we measure the FPN ϵ_{DC} and read-out noise ϵ_R by putting the cap in front of lens. Here, the average value is the FPN, and the standard deviation is considered as the boundary of the read-out noise.

In each wavelength, the optimal exposure time $t(\lambda)$ is adaptively estimated. The optimal exposure time $t(\lambda)$ can be represented as:

$$t(\lambda) =$$
$$\begin{cases} t_s \frac{\epsilon_{DC}+\epsilon_R+\mu}{L(\lambda)} & (if\ L(\lambda) < \epsilon_{DC} + \epsilon_R + \mu) \\ t_s & (otherwise) \end{cases} \tag{3.1}$$

where μ is an off-set value to bring the adjustment to the safer side.

3.3.3   Multispectral Image Synthesis

After capturing images, we can synthesize the obtained images $L(i, j, \lambda)$ to the spectral power distribution image $L'(i, j, \lambda)$:

$$L'(i, j, \lambda) = t_s \frac{(L(i, j, \lambda) - \epsilon_{DC}(i, j, \lambda))}{t(\lambda)} \tag{3.2}$$

Here, the FPN image $\epsilon_{DC}(i, j, \lambda)$ in arbitrary exposure time can be estimated by using following equation, according to the linear correlation between the FPN and exposure time, as shown in Fig. 3.3:

$$\epsilon_{DC}(i, j, \lambda) = \alpha(\lambda)\epsilon_{DC}^s(i, j, \lambda) \tag{3.3}$$

where $\epsilon_{DC}^s(i, j, \lambda)$ is measured as the FPN image first. This can be obtained to calculate the mean image of captured images when light is intercepted from the camera. The linear correlation between the FPN and exposure time is as follows:

$$\alpha(\lambda) = \frac{at(\lambda) + b}{at_s(\lambda) + b} \tag{3.4}$$

where a and b are, respectively, slope and intercept.

We calculate a spectral power distribution image $L(i, j, \lambda)$, which is divided into the channel values $L'(i, j, \lambda)$ in each pixel i, j by camera sensitivity function $C(\lambda)$, and LCTF transmittance function $T(\lambda)$. Fig. 3.2 shows the actual sensitivity functions of each.

$$L(i, j, \lambda) = \frac{L'(i, j, \lambda)}{C(\lambda)T(\lambda)} \tag{3.5}$$

Next, we stitch the multispectral images of different view angles. Stitching usually extracts image features from a pair of images, establishes correspondences among such extracted features, and calculates the translation and rotation parameters to superimpose overlapping areas for connecting these two images. Here, the features in multispectral images are different in each band image. To overcome this issue, we generate an intensity image using all the spectral images in each viewing direction. Second, we extract Scale-Invariant Feature Transform (SIFT) features (interest points) [53] from these initensity images and establish correspondences for obtaining the translation and rotation parameters. Finally, we stitch the spectral image of each view angle using these parameters. Fig. 3.5 shows a synthesized panoramic multispectral image.

3.4   Multispectral Image Segmentation

Segmentation of a multispectral image needs dimensional reduction. For dimensional reduction, linear and nonlinear reduction methods exist. Our prime objects, microorganisms on the bas-relief of the Bayon temple, have a nonlinear characteristic in spectral distributions due to the combination of top and bottom layers. This nonlinear problem can be solved either by employing the "kernel trick" explained below [78, 43] or extending the Ncut method.

First, we describe kernel principal component analysis (KPCA) [78] in subsection 3.4.2, which is a typical kernel method. Second, we describe the comparison between Kernel PCA and NCuts methods, and also discusses NCuts in detail in subsection
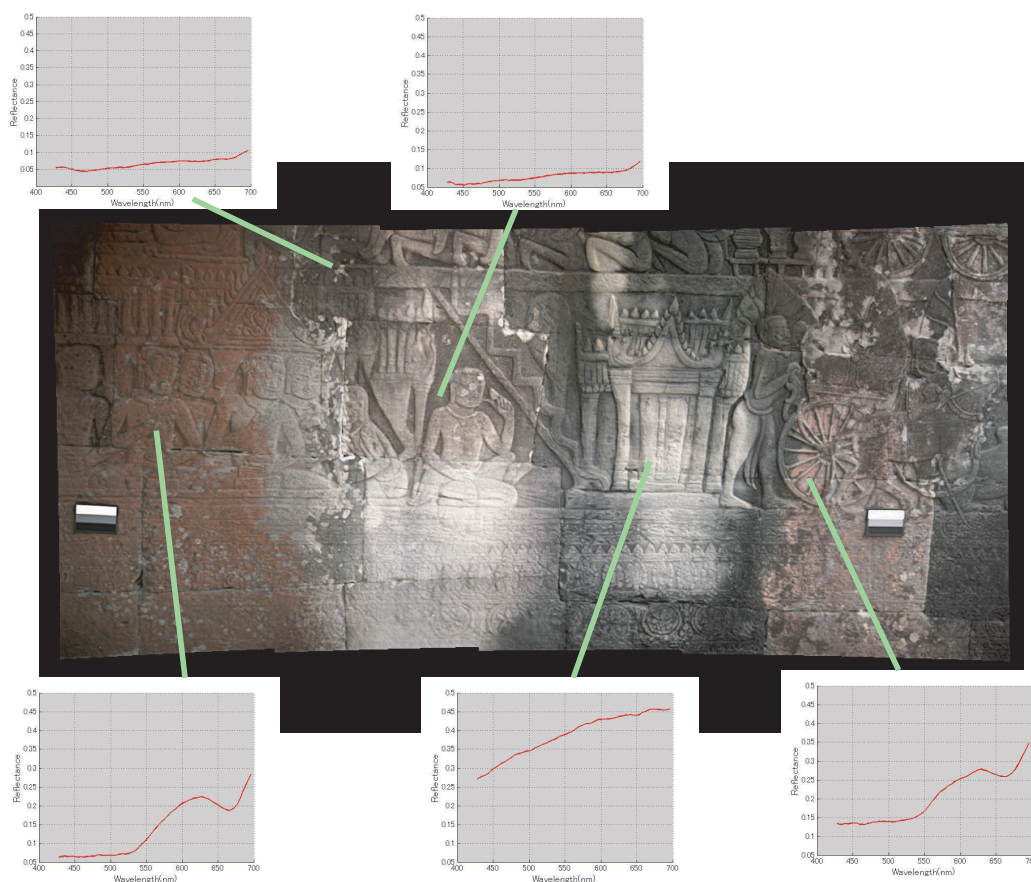
Figure 3.5: Panoramic image made from multispectral images: this image has 81 dimensional spectrum in each pixel.

3.4.3. Finally, subsection 3.4.4 describes the extension of the NCuts method to handle high-dimensional segmentation.

3.4.1 Nonlinear Mixing and Layered surfaces

Some of the top layer's pixel spectra typically show mixed spectral characteristics between the top layers and bottom layer. In a remote sensing field, these cause a so-called spectral mixing [38]. The spectral mixing can be categorized into two models: linear mixing and nonlinear mixing. The linear mixing occurs when one pixel consists of sub-parts from different materials; the different materials are distributed on the image plane. Generally, the linear mixing can be solved by reducing spectral dimension by using PCA, and clustering reduced data.

Our application, analysis of microorganisms, falls in the category of nonlinear

mixing. This mixing occurs due to layer surfaces such as microorganisms and bottom rock surfaces. The different half-transparent materials are distributed along the line of sight. The PCA method cannot be applied to nonlinear mixing, but mixing can be achieved either by employing the kernel PCA (KPCA) [78] or extending the NCuts method.

3.4.2   Segmentation using KPCA

KPCA is an extension of principal component analysis using the kernel trick. Let $I = \{I_1, I_2, I_3, ., I_i, .., I_N\}$, where I_i is input data such as color values or spectral values, of m dimension, at the node i, which is a pixel or a super-pixel. Using the kernel function $\Phi(I)$, we can map the original input data space, a nonlinear space, onto a kernel data space, a linear space, using $H = \{\Phi(I_i) \| I_i \in I\}$. To this kernel space, we can apply the PCA method, and this operation is referred to as the "Kernel trick."

$$\left\langle \Phi(I_i), \Phi(I_j) \right\rangle_H = K(I_i, I_j) \tag{3.6}$$

The Gram matrix $\tilde{K}$ of KPCA, similarity matrix among nodes, is given by:

$$\begin{aligned}
\tilde{K}_{ij} &= K(I_i, I_j) - \frac{1}{N} \sum_{a=1}^{N} K(I_i, I_a) \\
&\quad - \frac{1}{N} \sum_{b=1}^{N} K(I_b, I_j) + \frac{1}{N^2} \sum_{a,b=1}^{N} K(I_a, I_b)
\end{aligned} \tag{3.7}$$

Using the Gaussian Kernel, we can rewrite the Gram matrix in the following form:

$$\begin{aligned}
\tilde{K}_{ij} &= \exp(-\frac{\|I_i - I_j\|^2}{\sigma^2}) - \frac{1}{N} \sum_{a=1}^{N} \exp(-\frac{\|I_i - I_a\|^2}{\sigma^2}) \\
&\quad - \frac{1}{N} \sum_{b=1}^{N} \exp(-\frac{\|I_b - I_j\|^2}{\sigma^2}) \\
&\quad + \frac{1}{N^2} \sum_{a,b=1}^{N} \exp(-\frac{\|I_a - I_b\|^2}{\sigma^2})
\end{aligned} \tag{3.8}$$

KPCA maximizes the variance of the kernel space as is the case in the PCA method. The maximized variance can be represented as the eigenvector of the maximum eigenvalue of the Gram matrix. We can find its eignvalues by solving the following equation:

$$\tilde{K}_{ij} V_{jk} = \lambda_k V_{ik} \tag{3.9}$$

where λ_k represents the eigenvalues of the k in descending order, and V_{jk} represents the eigenvectors, accordingly. We can map original high-dimensional data into the lower-dimensional space, spanned by these k eigenvectors.

We use this procedure to apply KPCA to multispectral image analysis. First, we map multispectral data into low-dimensional space by using the kernel trick, checking the cumulative sum of the eigenvalues, about 98 % typically in the 10-dimensional space. Then, we can make clusters in this space by using the k-means method for the segmentation of an input multispectral image.

3.4.3 Normalized Cuts

We can employ the NCuts method to nonlinear segmentation in a manner similar to that used for the KPCA. As was described in the previous subsection, KPCA projects high-dimensional space to lower-dimensional space, using eigenvalue decomposition based on the Gram matrix. NCuts method employs the Laplacian matrix, instead of the Gram matrix, for nonlinear mapping from input data and Gaussian Kernel, and then finds the optimal lower-dimensional space using eigenvalue decomposition.

We prefer the NCuts method over the KPCA because of computational cost. KPCA needs more dimensions for effectively representing data, because typically a cumulative curve is rather flat in KPCA; there is not much difference in the contribution between two adjacent eigenvalues. On the other hand, in the NCuts method, once we find the partition number, indicating how many regions exist in an image, we only need to pick up n eigenvectors in ascending order, where n is the partition number. In our application, it is relatively easy to set the partition number as a rough estimation of how many regions of microorganisms exist in the scene. For this reason, we prefer the NCuts method to KPCA for our nonlinear segmentation.

The NCuts method consists of nonlinear dimension reduction and clustering. Among various segmentation methods, the Ncut method has a unique feature of nonlinear dimensional reduction. A detailed description of NCuts was presented in section 2.3.1 in Chapter 2.

3.4.4   Applying NCuts to multispectral segmentation

Dimensionality is one of the issues in applying the NCuts method to the multi-spectral image segmentation method. The NCuts method requires making a weight matrix of a high-resolution image, of which the dimensions are $(N \times N)$, where N is the number of image pixels, typically more than 250,000. The NCut method handles this issue by effectively using the proximity threshold, ignoring remote nodes for calculation, and ending up solving a sparse matrix of a high-dimensional image.

We employ a two-step method to overcome this high-dimensional issue. In our microorganism analysis, we cannot apply the proximity threshold because two remotely located regions from the same kind of microorganism should be classified into the same class. We assume that a nonlinear manifold of high dimension has a linear sub-space in a low dimension such as local linear embedding [72], or ISOMAP [96]. First, we over-segment the multispectral image using a standard PCA method and k-nearest neighbor method, and form super-pixels corresponding to each segment. Then, we apply the NCuts method to these super-pixels.

Our implementation is as follows: First, we compute M super-pixels by over-segmentation using PCA dimension reduction and k-nearest neighbor method. Second, we calculate M mean spectra for all M super-pixels. Let $I = \{I_1, I_2, I_3, ., I_i, .., I_M\}$, where I is spectrum data of m dimensional. Third, we compute the weight matrix W from M ($M < N$) super-pixel values using the following equation:

$$W_{ij} = exp\left(\frac{-\|I(i) - I(j)\|^2}{t^2}\right) \tag{3.10}$$

In our experiment, we set t, a normalization factor, at 70% of the maximum distance in the weight graph. Finally, we can segment a multispectral image into material regions by using this weight matrix and NCuts.

3.5   Experimental Results

In this section, we describe three experiments. We conducted accuracy verification of our method compared with a conventional method, and applied our method to the analysis of cultural assets.

3.5.1 Accuracy Verification of Multispectral Image

In this subsection, we evaluate image noise and spectral accuracy of a multispectral image given by our system.

Image Noise Fig. 3.6. (a) and (b) show, respectively, the captured image in fixed exposure, and the captured image by the proposed dynamic exposure method. The captured image from the fixed exposure method provides much noisier data. This effect is more apparent in the short wavelength area. On the other hand, the captured image given by our method is less noisy.

(a)

(b)
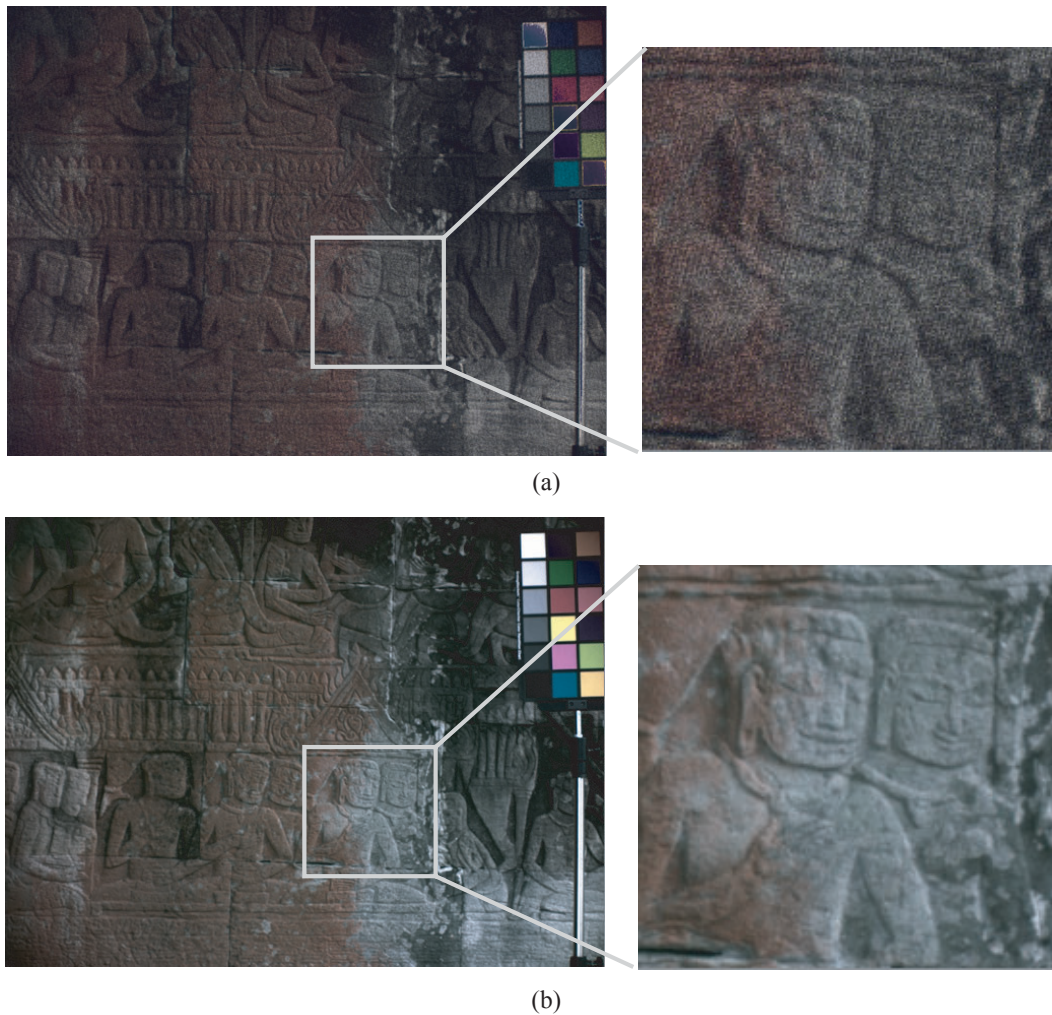
Figure 3.6: Image quality of synthesized image (a) Captured multispectral image in fixed exposure time. (b) Proposed method.

Spectral Accuracy   Table.3.1 shows the spectral accuracy of our system. In this experiment, we captured multispectral images of a color chart (X-lite Color checker), under artificial sunlight (Seric XC-100), by using both fixed exposure and the proposed dynamic exposure methods, respectively. Then, we measured the spectrum of each patch using a spectrometer (PhotoResearch PR-655) as the ground truth. Second, we calculated the root mean square error (RMSE) between the obtained spectral data and the ground truth in each patch. Compared with the RMSE values by the fixed exposure method, the RMSE values by the proposed method are much lower. The result also showed that our system is effective for spectral analysis.

			RMSE		
Color	Fix	AE	Color	Fix	AE
DarkSkin	4.469	1.301	YellowGreen	0.914	0.764
LightSkin	1.347	1.064	OrangeYellow	0.915	0.870
BlueSky	1.254	0.909	Blue	0.627	0.398
Foliage	3.060	0.850	Green	1.204	0.657
BluishFlower	1.196	0.885	Red	0.953	0.887
BluishGreen	0.916	0.516	Yellow	1.102	0.914
Orange	1.460	0.987	Magenta	1.002	0.885
PurplishBlue	1.420	1.074	Cyan	0.619	0.449
ModerateRed	0.937	0.892	White	1.174	0.892
Purple	1.109	1.029	Mean	1.352	0.854

Table 3.1: Spectral accuracy

3.5.2   Segmentation of a Panoramic Multispectral Image

Fig. 3.7 shows the segmentation result of panoramic multispectral image. The image resolution is 2392×1024. If we calcurate the weight matrix of this image without our local approximation method, the matrix size is 2449408×2449408. This size does not allow a general computer allocates memory.
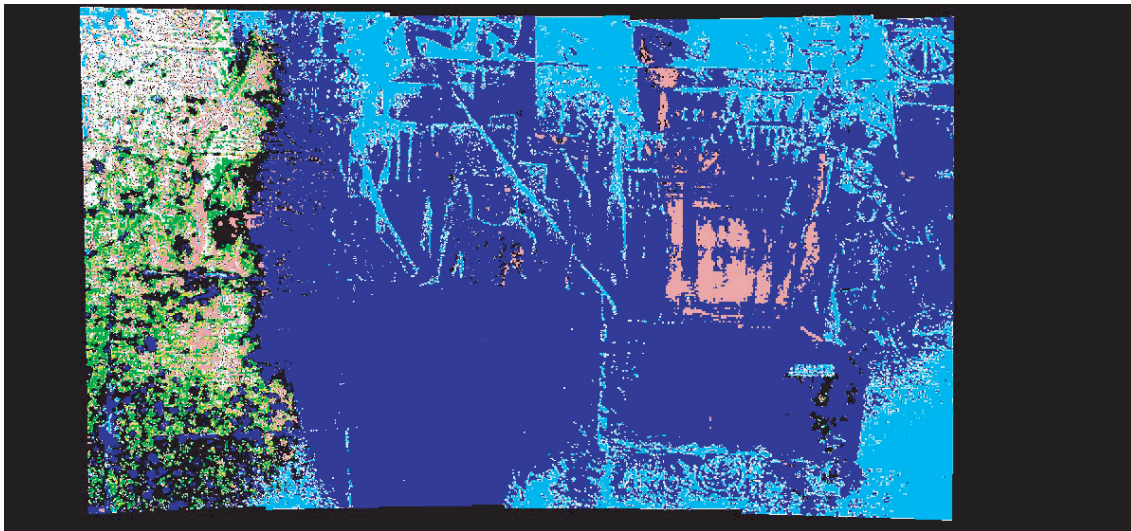
Figure 3.7: Segmentation result of panoramic multispectral image. The image has the resolution of 2392×1024.

3.5.3   Comparison with Conventional Segmentation Method

In this subsection, we compared conventional segmentation methods and the proposed method. First, we calculated reflectance spectra from the input multi-spectral image by using our method. Second, we segmented the reflectance spectra image into different materials using these methods:

1. Method 1: PCA and k-means clustering

2. Method 2: KPCA and k-means clustering

3. Method 3: Proposed NCuts on super-pixel method

3D object   Fig. 3.8 shows the segmentation result of a 3D object. Method 1, PCA and k-means, in Fig. 3.8. b, cannot segment the part of the chest, because this method cannot handle nonlinearity due to noise and shading effects. Method 2, KPCA and k-means, Figs. 3.8. c and d work relatively well in handling the nonlinear effects. However, the result by Method 3, the proposed method, is better than one given by Method 2 in the chest area and the background area.

(a) RGB image

(b) PCA

(c) Kernel PCA

(d) Proposed method

Figure 3.8: Segmentation result of 3D object (a) Input image (b) Method 1: PCA + k-means (c) Method 2: KPCA + k-means (d) Method 3: Proposed NCuts on super-pixel method
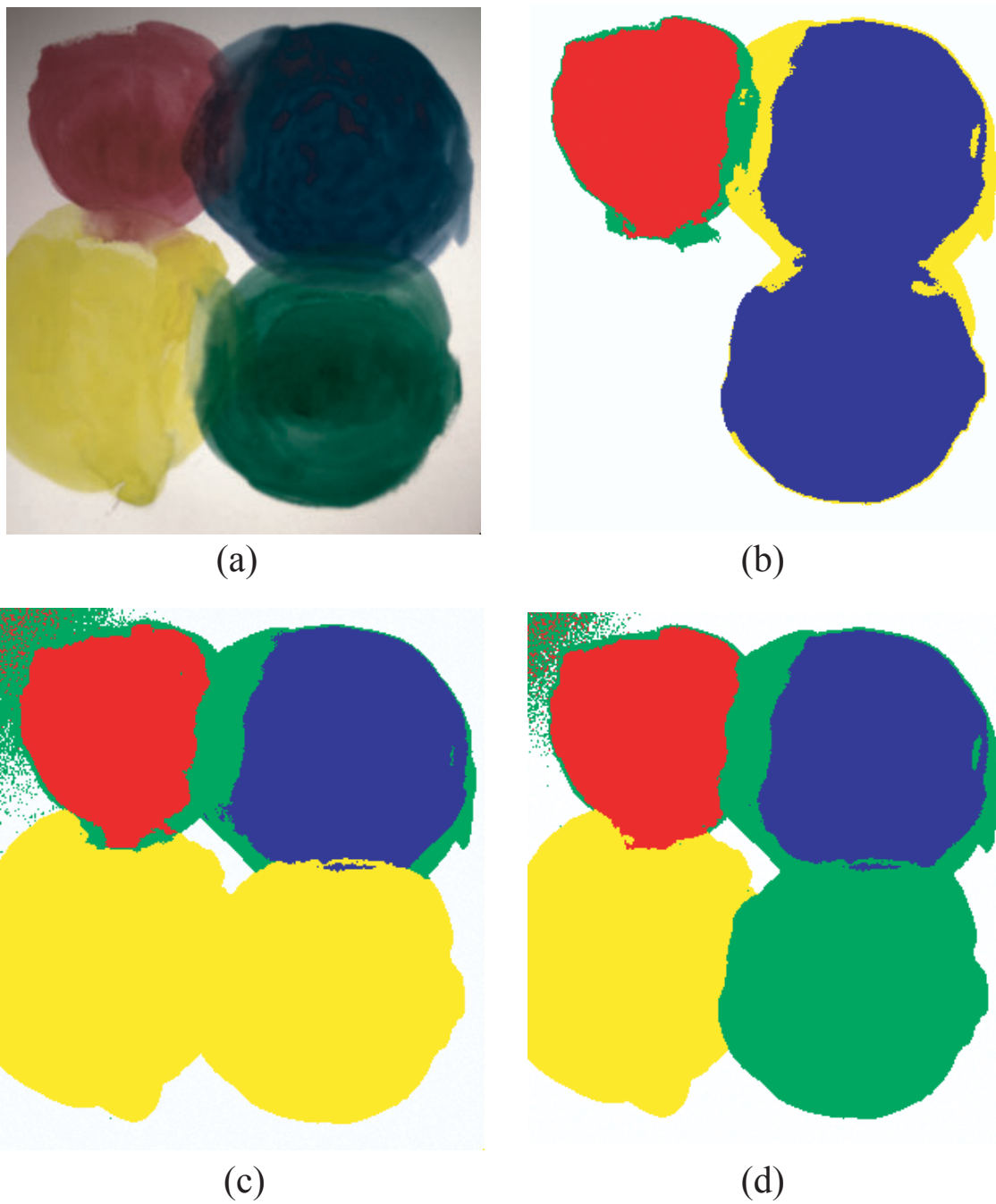
Figure 3.9: Segmentation result of layered surfaces (a) Input image (b) Method 1: PCA + k-means (c) Method 2: KPCA + k-means (d) Method 3: Proposed NCuts on super-pixel method

Layered surfaces   Fig. 3.9 shows the segmentation result of layered surfaces for examining the effect on the nonlinear mixture. The input image is a watercolor pigment painted on a white paper. This image has complex color between the top layer and the bottom layer. Fig. 3.9. b, by Method 1, and c, by Method 2, include significant segmentation error.

3.5.4   Spectral Image Analysis for Bas-relief at the Inner Gallery of Bayon Temple

This section describes how we applied our proposed multispectral imaging system and segmentation method to analyze a cultural asset.

At the Bayon Temple in Cambodia, microorganisms are one cause of deterioration in the inner gallery. Fig. 3.10 shows the microscope images of microorganisms observed at each spot. Due to deterioration, the detailed bas-reliefs on the walls are losing their shapes. We examined the kind, distribution, and reproductive cycle of the microorganisms to find an effective method to remove them. We assumed that some of them could be discriminated by detecting the absorbance spectra of photosynthetic pigments in them, and we found we could calculate absorbance from reflectance.
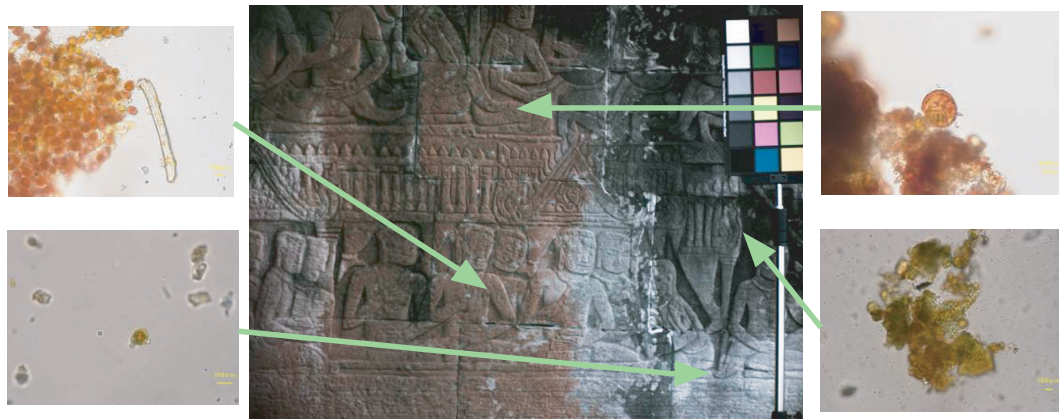
Figure 3.10: Microbial growth on the wall surface: microscope images of microorganisms observed at each spot

Fig. 3.12 shows the image of the scene we observed. Then, we found correspondences among multispectral images in different seasons to the same area through 3D data. The results in Fig. 3.5.4 show the measured absorbance spectrum of each
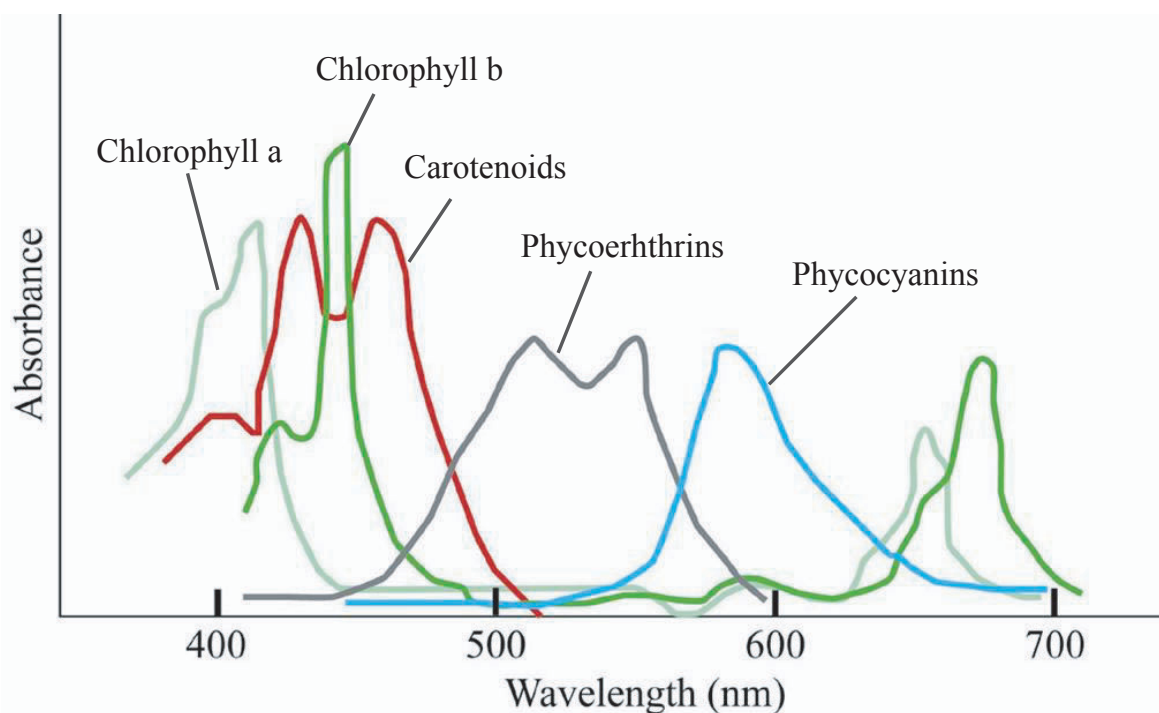
Figure 3.11: Absorbance of photosynthesis pigments: green algae mainly has chlorophyll a and b. Cyanobacteria mainly has chlorophyll a and phycocyanins.

segmented area. The three areas, depicted using blue, white, and red colors in the figure, should be differentiated by the quantity of phycocyanin. This is because the areas' absorption has large differences at around 600 nm, which coincides with the phycocyanin's absorbance spectrum as shown in Fig. 3.11. As Fig. 3.14 shows, white and blue areas decrease in a dry season compared to a rainy season, which implies that the quantity of phycocyanin has decreased in the dry season. The results indicate that the cyanobacteria, the main source of phycocyanin, increase in a rainy season and decrease in a dry season.

Aside from microorganisms, we also show the segmentation results of wall paintings in the Noriba tumulus in Figs. 3.15 and 3.16. These results are shown by the degradation of pattern in a degraded wall painting.

Figure 3.12: Observed scene image: this scene was made by mapping a multispectral image onto 3D data.
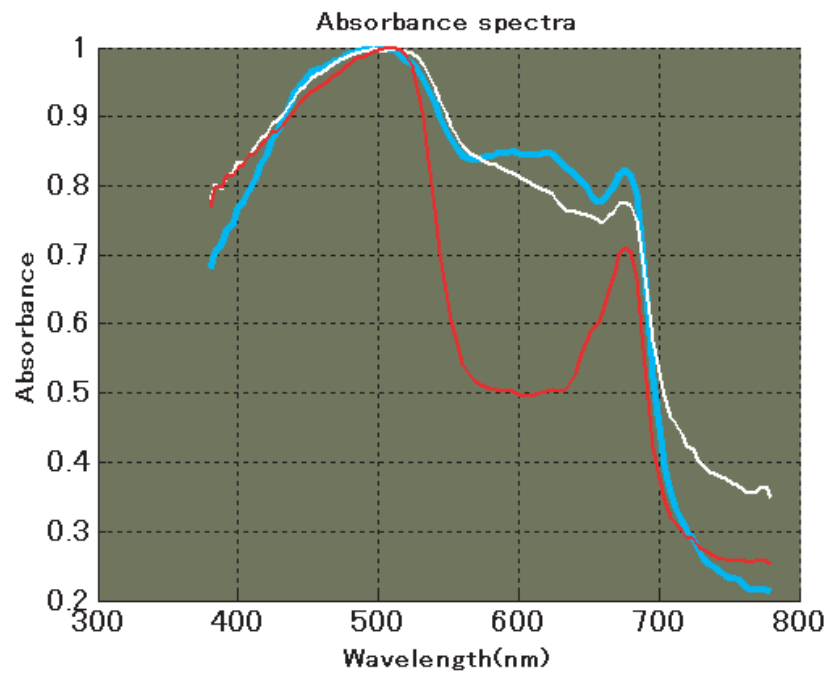
Figure 3.13: Absorbance spectrum in each class area.

(a)
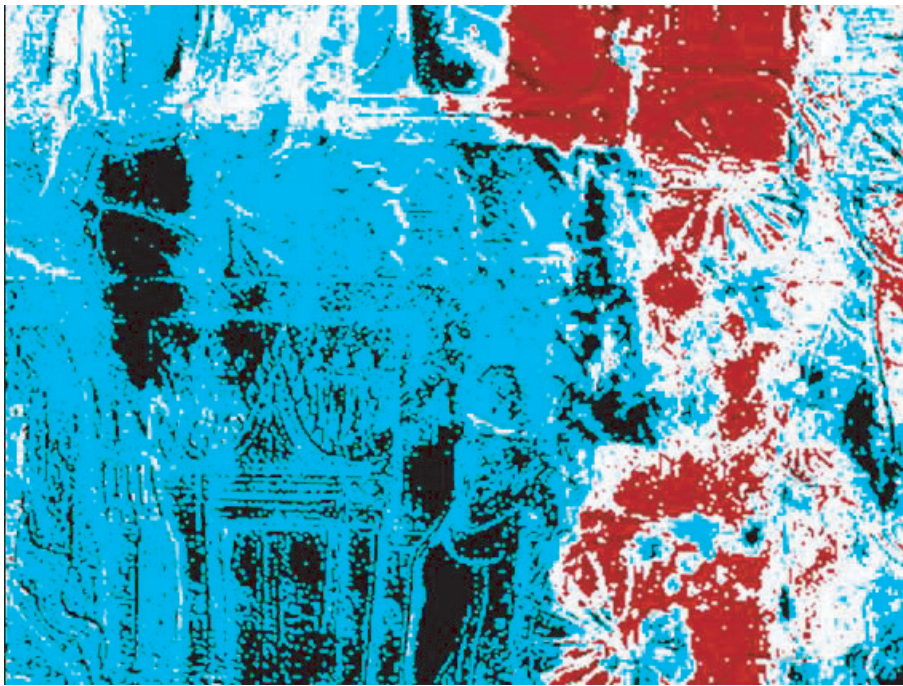
(b)

Figure 3.14: Segmentation results of microorganisms. (a) Rainy season (b) Dry season

3.6   Summary

We proposed a novel multispectral imaging system and a segmentation method for multispectral images. Our system can efficiently obtain a wide view angle image in an outdoor environment, and also segment a high-dimensional spectral image effectively. In our experimentation, we found that our proposed multispectral imaging system has sufficient accuracy for material segmentation. Furthermore, our multispectral image segmentation method could effectively segment both a 3D object and layered surfaces into different spectra. The system also analyzed microorganisms on bas-reliefs in the Bayon Temple. Our experimental results showed the reproductive cycle of microorganisms in rainy and dry seasons.
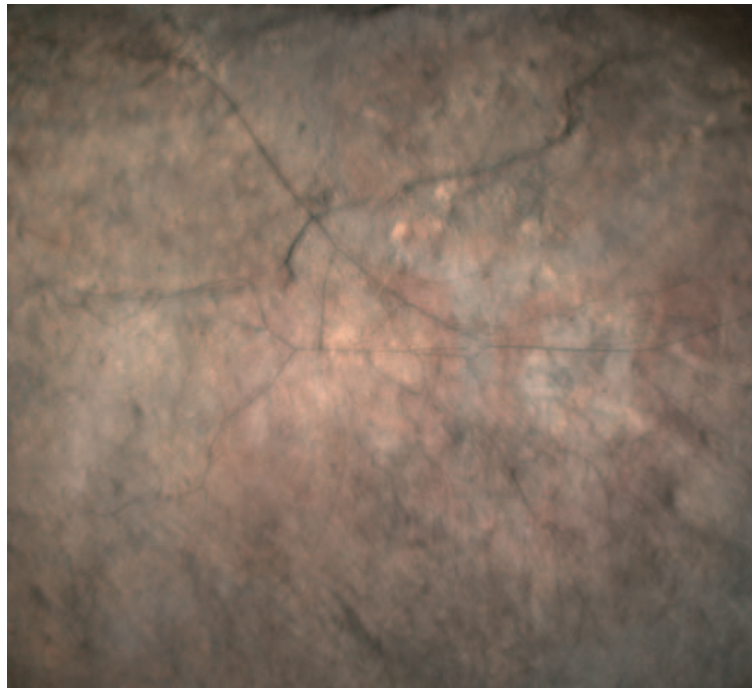
(a)
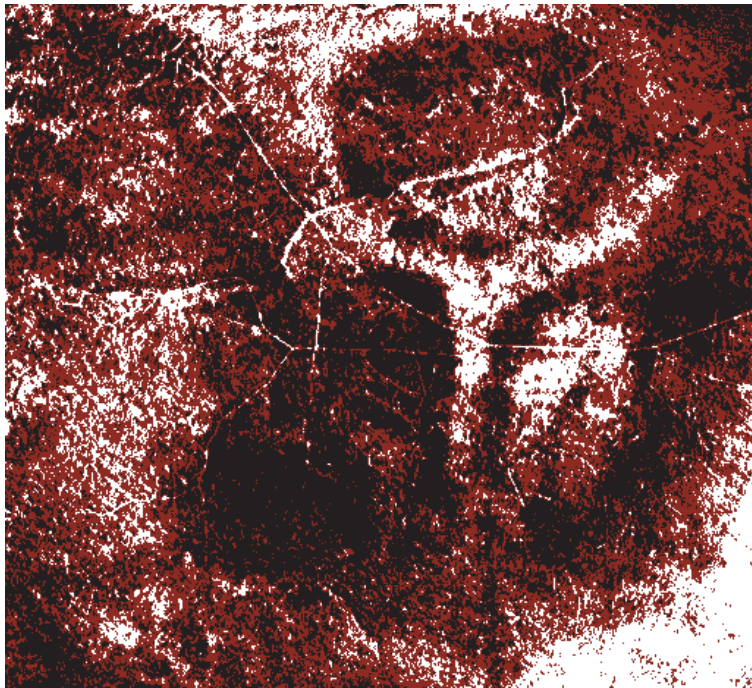
(b)

Figure 3.15: Segmentation result of wall painting in decorated tumulus 1. Segmentation result represents the pattern of degraded wall painting. (a) Reference image. (b) Segmentation result.
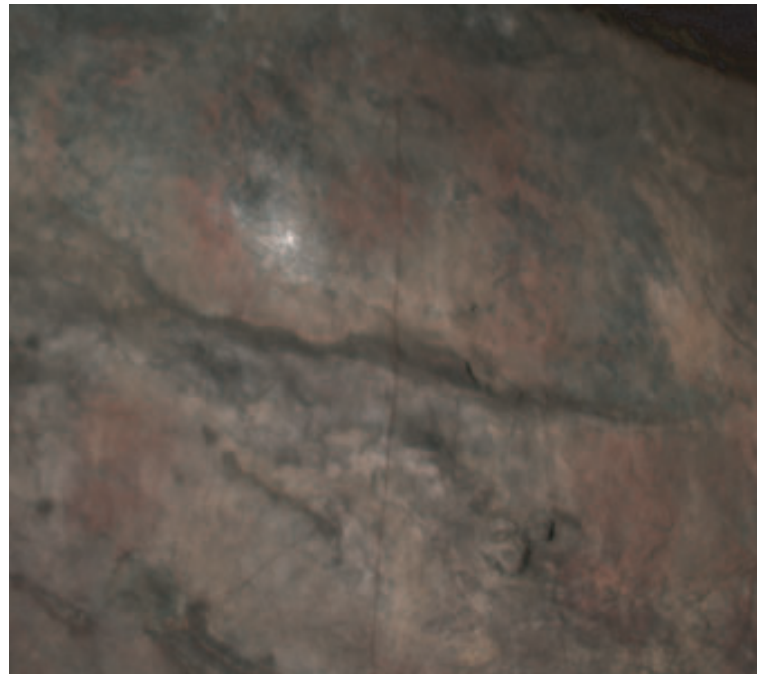
(a)
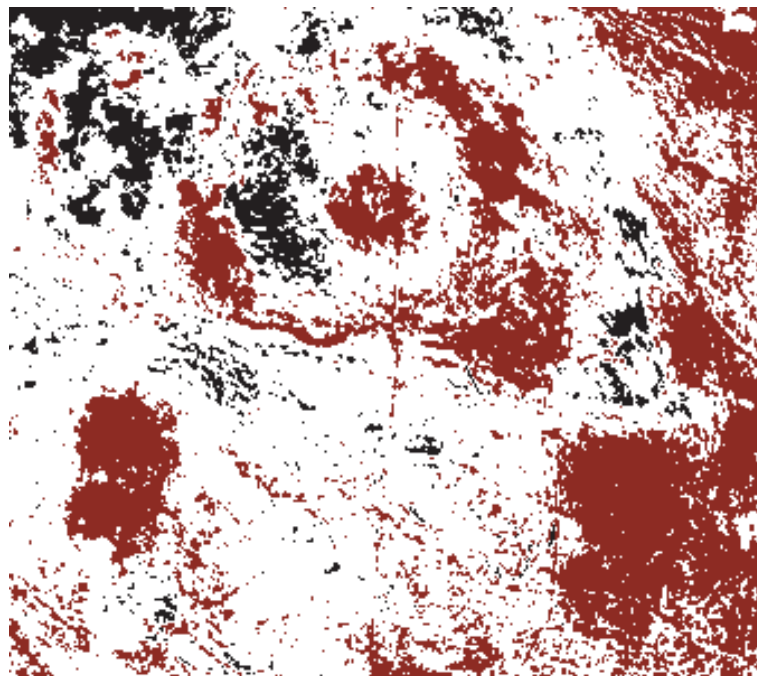
(b)

Figure 3.16: Segmentation result of wall painting in decorated tumulus 2. Segmentation result represents the pattern of degraded wall painting. (a) Reference image. (b) Segmentation result.

Chapter 4

Decomposing Complex Reflection Components of a Layered Surface Using the Spider Model

Many object surfaces are composed of layers of different physical substances, and these are known as layered surfaces. Such surfaces (e.g., patinas, water colors, and wall paintings) have more complex optical properties than diffuse surfaces, and generally are incapable of being segmented. This is because their colors change according to the mixtures of the optical properties of the layers, implying the colors change gradually instead of changing sharply. In this chapter we focus mainly on surfaces with two layers, namely, top and bottom layers. Given a single input image, our goal is to segment the colors of the image based on the physical model of layered surfaces, and to extract the approximated optical properties of the two layers. To physically model the layered surfaces, we use the Lambert-Beer based model, which is sufficiently accurate to model surfaces with negligible scattering coefficients. The basic ideas of our proposed method are first, to use a nonlinear correlation between color channels, which we define as the Spider model, to estimate the label of a pixel. Then, we use the Markov random fields to estimate the properties of the top and bottom layers in the whole image. The end results provide us with the top layer's opacities, the top layer's reflections, and the bottom layer's reflections. The latter two are equivalent to the top and bottom layers' segmented colors. Furthermore, our method can apply not only to RGB images but also to spectral data. Experiments

(a)   (b)   (c)
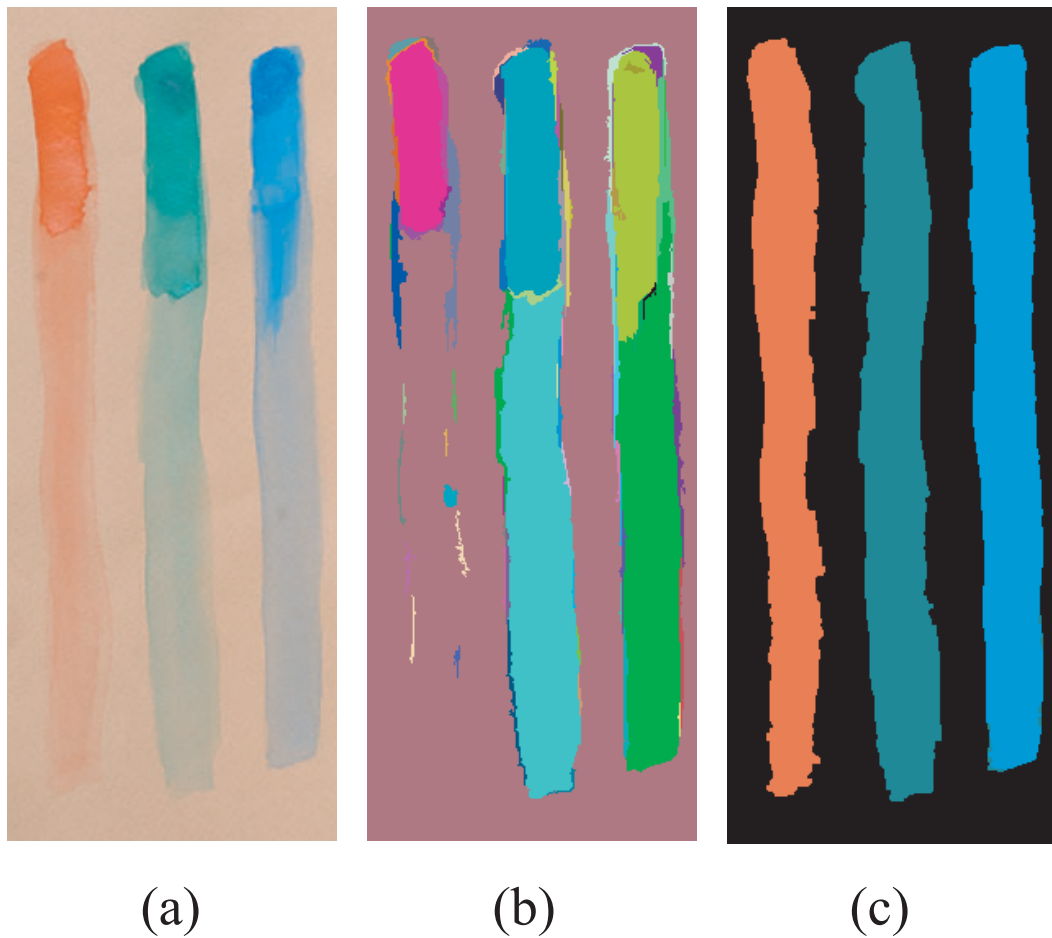
Figure 4.1: (a) Input image. (b) Segmentation result by using a graph-based segmentation method [12]. (c) Segmentation result by using the proposed method.

with real images show the effectiveness of our method.

4.1   Introduction

The surface of most natural objects contains a number of layers with different physical substances. For instance, human skin is composed of at least two layers: epidermis and dermis. Each of these layers has distinct optical properties consisting of absorption, scattering, transmittance, reflectance, etc. This kind of surface is known as a layered surface. The reflectance of an object, and therefore the object's appearance, is determined by the number of layers and their optical properties. Other examples of layered surfaces in nature are leaves, patinas, biological tissues, fruits

(grapes, strawberries, tomatoes), etc.

Optically, layered surfaces are categorized as turbid media, and the fields of optics/color science have introduced many models of them [4, 41, 111, 34, 6, 68]. These models are principally based on radioactive transfer theory [6]. One highly detailed representation is the many-flux scattering model presented by Mudgett [58]. However, in practical applications a simpler two-flux approximation called the Kubelka-Munk (KM) model [42] is preferred although this complex model has many parameters that make it difficult to apply an image. Aside from the KM model, the Lambert-Beer (LB) Law [2] is also commonly used to represent light transmission through a transparent substance in optics and color science. While the LB law does not explicitly take account of the scattering coefficient, it is mathematically much simpler than the KM model. Moreover, the LB-based model can describe layered surfaces appropriately [63, 62, 73, 11, 79] in most cases when the layers have a negligibly small scattering coefficient.

Despite the number of layers, most methods assume that an object's surfaces can be modeled by the Lambertian model [45] in many areas of computer vision. This assumption is not always correct, and it causes some methods to be inaccurate in delivering their outputs for objects with layered surfaces. One of those areas is color segmentation. Most methods in this area assume that different colors mean different regions, and these methods tend to fail when the colors change gradually instead of changing crisply. Fig. 4.1.a shows an input image with gradual color changes, due to the change of the optical properties of the top layers. Fig. 4.1.b shows the result of graph-based segmentation [12]. As one can observe, the regions are incorrectly segmented. Another area affected by the incorrect assumption about object surfaces is physics-based vision. Surface reflectance parameter estimation (e.g. [77, 64, 57]) and surface color analysis (e.g. [39, 40]) will fail to provide correct results if the methods are applied straightforwardly to layered surfaces.

In the light of the problems of layered surfaces and color segmentation, our main goal in this chapter is to provide a practical framework for layered surfaces that can be used to solve color segmentation and to estimate the approximated optical properties of layered surfaces, particularly when the surfaces consist of two layers. Such optical property estimation and color segmentation should be useful for many applications in computer vision and computer graphics. To attain our goal, we rely for our optical framework on the LB-based model, using a nonlinear correlation between different color channels. This nonlinear correlation represents the color's

gradual changes. We define this nonlinear correlation as the Spider model. Our basic ideas are to use the Spider model to estimate the labels of pixels, and then to build a cost function based on Markov random fields to estimate the top and bottom layer's properties. An example of our color segmentation is shown in Fig. 4.1.c, which is more accurate compared with that of the graph-based segmentation method.

While there are no methods sharing our goals and techniques, to our knowledge, there are a few methods that use the LB-based model to enhance visibility in atmospheric imagery [63, 62, 73, 11] and oceanic imagery [79]. Furthermore, the LB-based model happens to be very similar to a model used in digital matting, which is known as the α-matting equation. The main goal of digital matting is to extract the opacities of foreground objects, and many methods have been proposed to achieve this goal. Poisson-based matting [87] resolves the problem by using the gradients of the opacity and solving the partial differential equation. Robust matting [104] proposes a robust global sampling method, assisting the local sampling procedure to generate enough color samples. Closed-form matting [50] and spectral matting [48] assume foreground and background colors can be fitted with a linear color line model in local windows, which leads to a quadratic cost function in alpha that can be minimized globally. Other methods of digital matting are [74, 8, 7, 9, 107, 108, 103, 1].

Aside from physics-based computer vision and digital matting, segmentation methods based on user interactions, like Lazy Snapping [52] or Grab Cut [71], provide an elegant framework to solve object segmentation. However, their data costs are not intended to handle layered surfaces or colors with gradual changes. In the experimental results, we will compare our results with recent digital matting [48] and segmentation [52] techniques.

4.2   Overview

The structure of this chapter is as follows. In section 4.3, we describe a layered surface model based on the Lambert-Beer model. Next, we describe our proposed model Spider model, and also present a color segmentation and parameter estimation algorithm using the Spider model in section 4.4. We demonstrate implementation of our method in section 4.5. Results of some experiments are presented in section 4.6. The previous sections apply to the RGB-based method, but in section 4.7, we extend our method to spectral data. Finally, we summarize this chapter in section 4.8.
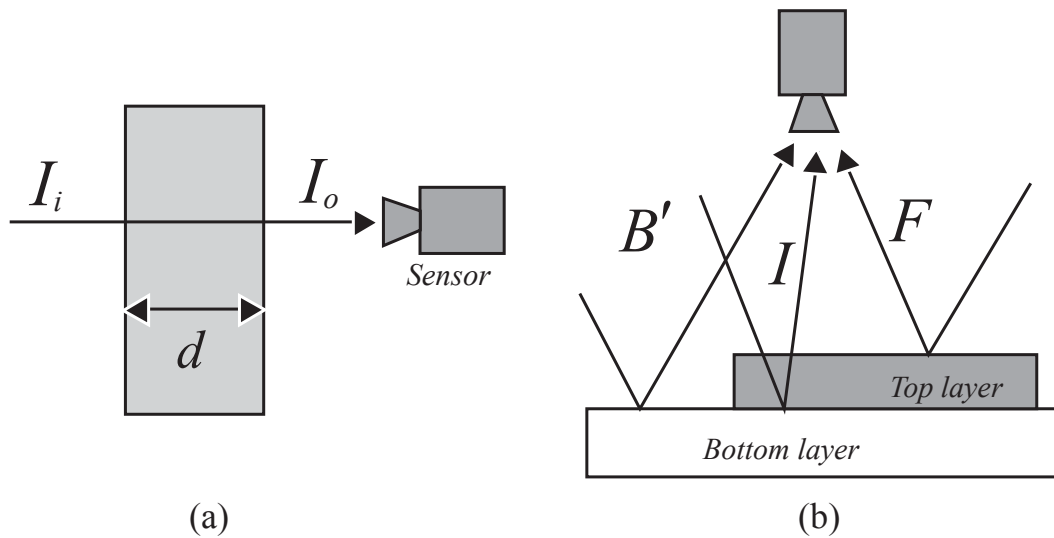
Figure 4.2: (a).The optical model of the Lambert-beer model. (b).The optical model based on the Lambert-Beer model of layered surface objects

4.3 Layered Surface Model

According to the Lambert-Beer Law [2], the optical transmittivity of light passing through a transparent object can be described as the exponential function of the attenuation factor multiplied by the distance of the light traveling through the object. Mathematically, it is written as:

$$T(\lambda) = \frac{I_o(\lambda)}{I_i(\lambda)} = e^{-\mu(\lambda)d} \tag{4.1}$$

where T is the optical transmittivity, λ is the wavelength, I_o is the intensity of the outgoing light, I_i is the intensity of the incoming light, μ is the attenuation factor of the object, and d is the distance of the light traveling through the object (the length of the light path). Assuming the light travels perpendicularly to the object surface, d can represent the optical thickness of the object. Regardless of the light direction, for simplicity, we call d optical thickness throughout this chapter, although it should be considered to be the length of the light path. The attenuation factor, μ, is the product of the extinction coefficient and its concentration. Fig. 4.2. a shows the pictorial description of the law.

The Lambert-Beer Law is the foundation for a model commonly used in oceanic and atmospheric optics to describe the light attenuations caused by the medium's particles, where a cloud of the particles in the medium is treated as a transparent

object. However, instead of assuming light coming from one direction, this model conveys the idea of light coming from two directions simultaneously, namely from the back of the particle cloud and from the front of the particle cloud:

$$I(\lambda) = B(\lambda)e^{-\mu(\lambda)d} + F(\lambda)\left(1 - e^{-\mu(\lambda)d}\right)$$ (4.2)

where I is the mixture intensity of the transmitted light from B and the reflected light from F. We also call I a mixed layer. B and F are the intensity of light coming from the back and the front of the particle cloud, respectively. The first term at the right side of the equation is exactly the same as the Lambert-Beer Law, while the second term is the consequence of the first term, by assuming that the light travels solely in forward and backward directions. This means that if the attenuation of the object or particle cloud is $e^{-\mu(\lambda)d}$, then the remaining reflection factor is $(1 - e^{-\mu(\lambda)d})$. Many researchers in physics-based computer vision successfully use the model (e.g., [63, 62, 73, 11, 79]). We call the model the Lambert-Beer based model, or LB-based model.

Interestingly, the LB-based model happens to be very similar to the digital matting equation:

$$I = \alpha F + (1 - \alpha)B$$ (4.3)

where α is the pixel's opacity. If we define $\alpha = (1 - e^{-\mu d})$, then the last equation is equivalent to Eq. (4.2). However, most research in digital matting assumes that α is scalar, which is not always the case for $e^{-\mu d}$, since μ is dependent on the wavelength. Therefore, when α is assumed to be scalar, the digital matting is not identical to the LB-based model.

In this chapter, we use the LB-based model and consider the layered surfaces have no scattering coefficients or the scattering coefficients are negligibly small. Moreover, instead of using spectral data, we first use RGB color data taken from an ordinary digital camera for which the gamma correction is set to "off." (However, in section 4.7, we will describe an extension method for spectral data.) The LB-based model for the RGB data can be expressed as:

$$I_c(x) = B_c(x)e^{-\mu_c(x)d(x)} + F_c(x)\left(1 - e^{-\mu_c(x)d(x)}\right)$$

(4.4)

where index c represents one of the three color channels {r,g,b}, and x is the spatial image coordinate. B_c is the reflection by the bottom layer after receiving light that has

passed through the top layer. F_c is the reflection of the top layer when the thickness is infinitely large (or sufficiently large so that the bottom layer does not affect the top layer's reflection). This reflection occurs after the top layer receives light coming directly from the light source. In the last equation, we assume that the camera's color sensitivities follow the Dirac delta function. For the sake of simplicity, we will omit x throughout the chapter; however, unless it is stated otherwise, the variables should be considered to be dependent on x. Like the KM model, we also assume that the object surfaces are flat, and both top and bottom layers are made from diffuse materials.

Given an image like that in Fig. 4.1. a, there are two types of bottom layers. The first is the bottom layer that is not covered by the top layer. This bottom layer receives light directly from the light source, which mathematically can be described as:

$$B'_c = L_c \rho_c \tag{4.5}$$

where B'_c is the reflection of the bottom layer when it is not covered by the top layer. L_c is the light intensity. ρ_c is the albedo of the bottom layer.

The second type is the bottom layer covered by the top layer, which we can formulate as:

$$B_c = L_c e^{-\mu d} \rho_c, \tag{4.6}$$

and differs from Eq. (4.5) due to the change of the light impinging on its surface ($L_c e^{-\mu d}$). Note that in the last equation, we ignore the cumulative reflections reflected back and forth from the bottom layer to the top layer (the interface reflections), as shown in Fig. 4.2. b.

4.4   Segmentation and Parameter Estimation

In this section, given a set of image intensities, I_c, containing layered surfaces, we intend to, first, segment the top layers according to their reflections or colors, and second, to estimate the optical properties of the top layers. To accomplish this task, we need to derive the correlations of the image intensities in the RGB space. The derivation will be separated into two parts: first, when the values of F_c are known, and second, when the values of B_c are known.

(a)
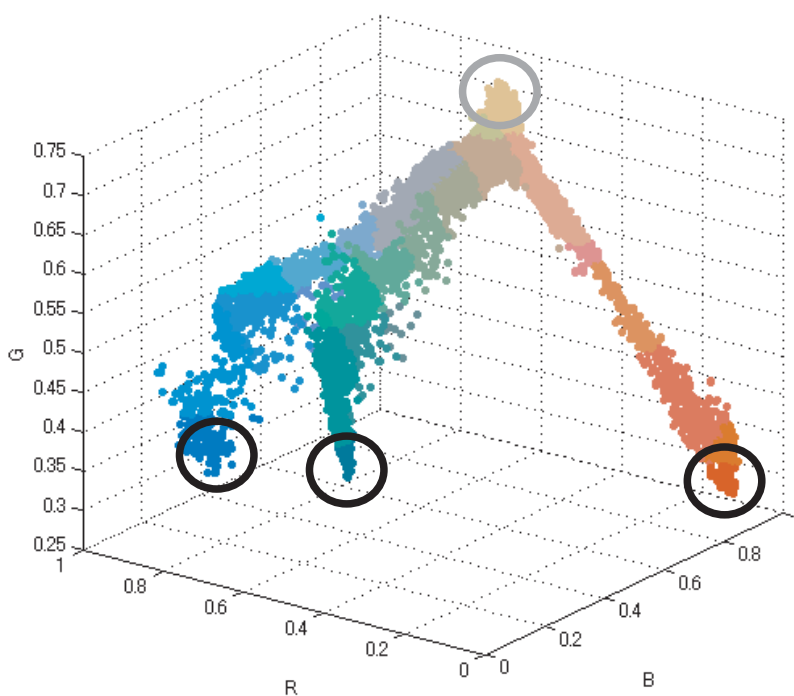
(b)

Figure 4.3: Spider model: (a) An image having layered surfaces (b) The plot of (a) in normalized RGB space. The gray circle represents the bottom layer's color. Black circles represent the top layer's colors.

Known Top Layers Considering the intensities in the red and green color channels, from Eq. (4.4), we can write:

$$I_r = B_r e^{-\mu_r d} + F_r(1 - e^{-\mu_r d}) \tag{4.7}$$

$$I_g = B_g e^{-\mu_g d} + F_g(1 - e^{-\mu_g d}) \tag{4.8}$$

In the last two equations, all variables are independent from the color channels except for d. Thus, by letting $\epsilon_c = e^{-\mu_c d}$:

$$-d = \frac{\log \epsilon_c}{\mu_c} \tag{4.9}$$

$$\frac{\log \epsilon_r}{\mu_r} = \frac{\log \epsilon_g}{\mu_g} \tag{4.10}$$

$$\epsilon_r = \epsilon_g^{\mu_r/\mu_g} \tag{4.11}$$

From Eq. (4.8), we know that:

$$\epsilon_g = \frac{I_g - F_g}{B_g - F_g} \tag{4.12}$$

Substituting the last equation into Eq. (4.11), we can obtain:

$$\epsilon_r = \left(\frac{I_g - F_g}{B_g - F_g} \right)^{\mu_r/\mu_g} \tag{4.13}$$

Finally, by plugging the last equation into Eq. (4.7), we can express the intensity of the red color channel as:

$$I_r = F_r + \psi_r(I_g - F_g)^{\gamma_r} \tag{4.14}$$

where $\gamma_r = \mu_r/\mu_g$, and $\psi_r = (B_r - F_r)/(B_g - F_g)^{\gamma_r}$. Accordingly, we can apply to the blue color channels, resulting in the following equation:

$$I_b = F_b + \psi_b(I_g - F_g)^{\gamma_b} \tag{4.15}$$

where $\psi_b = (B_b - F_b)/(B_g - F_g)^{\gamma_b}$, and $\gamma_b = \mu_b/\mu_g$.

Eqs. (4.14) and (4.15) imply that the correlations of the intensities in different color channels are not linear, since $\mu_r \neq \mu_g \neq \mu_b$ is not. To obtain $\{\psi_c, \gamma_c\}$, we assume the values of F_c are known.

Known Bottom Layers Accordingly, we can derive from Eqs.(4.16) and (4.17) equations that are similar to Eqs. (4.14) and (4.15) when the values of B_c are known. Let $\alpha'_c = 1 - e^{-\mu_c d}$, and then Eqs. (4.16) and (4.17) become:

$$I_r = B_r(1 - \alpha'_r) + F_r \alpha'_r \tag{4.16}$$

$$I_g = B_g(1 - \alpha'_g) + F_g \alpha'_g, \tag{4.17}$$

which eventually produce:

$$I_r = B_r + \psi'_r(I_g - B_g)^{\gamma'_r} \tag{4.18}$$

$$I_b = B_b + \psi'_b(I_g - B_g)^{\gamma'_b} \tag{4.19}$$

where $\psi'_r = (F_r - B_r)/(F_g - B_g)^{\gamma'_r}$, $\psi'_b = (F_b - B_b)/(F_g - B_g)^{\gamma'_b}$, $\gamma'_r = \mu_r/\mu_g$. and $\gamma'_b = \mu_b/\mu_g$. Based on these equations, we can obtain the values of $\{\psi'_c, \gamma'_c\}$.

Fig. 4.3 shows the plot of the intensities, I_c, of layered surfaces (Fig. 4.1. a) in the RGB space, which forms a curved line as predicted by Eqs. (4.14), (4.15) or Eqs. (4.18), (4.19). We define these correlations according to the Spider model, since the RGB plot (Fig. 4.3) is similar to Spider. The Spider model is the core of our method, since by obtaining these correlations. we are able to know whether a pixel belongs to a bottom layer or a top layer, which in turn enables us to segment the colors of the top layers. Moreover, using these equations we can estimate the approximated optical parameters of the top layers. In the following subsections, first, we will discuss the segmentation of layered surfaces, and then follow with parameter estimation.

4.4.1 Color Segmentation

Given an image like that in Fig. 4.1. a, and we ask users to mark the input images based on the mixture reflection and the bottom layers like conventional segmentation methods. Then, the problem of segmentation is identical to a labeling problem, namely, how to know whether a pixel belongs to the bottom layer or to the red/green/blue top layers. Solving this problem is also equivalent to estimating the values of ψ_c and γ_c, since, by knowing the values of these parameters, we can draw curved lines in the RGB space connecting the top layers to the bottom layer, as shown in Fig. 4.3. These curved lines, the Spider model, definitively represent the top layers' gradual color changes. As a result, we can compute the probability of the label of a pixel based on the distance between the pixel's RGB value and the lines. The closer the distance, the higher the probability. Besides, since the pixel could be part of the bottom layer, we should also include the distance between the pixel's RGB value and the RGB value of the bottom layer.

To estimate the values of $\{\psi_c, \gamma_c\}$, we employ a fitting algorithm based on the Lavenberg-Marquardt method and on Eqs. (4.14) and (4.15) or Eqs. (4.18) and (4.19). Provided the information of regions of the mixed layers and the bottom layers by users, we find the values of F_c by plotting a marked region (representing one of the

mixed layers) into the RGB space. Here we assume that the value of F_c is the mixed layer's point of greatest distance from B'_c in the RGB space. Although this point is not always the actual F_c, since our goal is segmentation, this assumption does not do any harm to the segmentation results.

Having estimated the values of $\{\psi_c, \gamma_c\}$ for all mixed layers, we define a cost function based on the RGB values of the input image, the bottom layers, and the curved lines. Let $Q = [1, \ldots, i, \ldots, N]$, where Q is the set of labels, namely the labels for the top layers and the bottom layers. N is the number of the top layers plus the number of the bottom layers. Then, the cost function is described as:

$$
D(\phi_x = i | B'_{c,i}, l_i, p_x) = \begin{cases} 0 & \text{if } E(p_x, B'_{c,i}) < th \\ 1 - e^{-E(p_x, l_i)} & \text{otherwise} \end{cases} \tag{4.20}
$$

where ϕ_x is the random variable representing the label of pixel p_x. $B'_{c,i}$ is the bottom layer's RGB value, as in Eq. (4.5). l_i represents the curved line created by parameter ψ^i_c and γ^i_c. Subscript x represents the spatial coordinate of the pixel. Function E represent the Euclidean distance in the RGB space. Threshold th is set depending on the noise level of the bottom layer and the camera. In our experiment we set the value between $10 \sim 20$ (within RGB standard values from 0 to 255). As the initial values, for all values of i and x, we set $D(\phi_x = i | B'_{c,i}, l_i, p_x) = 1$.

Like most segmentation methods, we also employ the smoothness constraint, and model the spatial correlations based on Markov Random Fields (MRFs):

$$
\begin{aligned}
E\left(\{\phi\}, \{B'_c\}, \{l_i\}, \{p\}\right) &= \sum_x D(\phi_x = i | B'_{c,i}, l_i, p_x) \\
&+ \sum_{x,y} S(\phi_x, \phi_y)
\end{aligned} \tag{4.21}
$$

where $S(\phi_{i,x}, \phi_{i,y})$ will be zero if $\phi_x = \phi_y$, and one otherwise. To minimize the cost function, we use graphcuts for multiple labels [89].

4.4.2 Parameter Estimation

Our framework is not only capable of segmenting a layered surface, but also of estimating the approximated values of the optical properties of the top layers, namely, the values of $e^{-\mu_c d}$, F_c. The bottom layer's reflections for the whole input image can be obtained straighforwardly using the estimated top layer's properties.

As mentioned in section 4.3, while in some cases we can observe B'_c directly from the input image, the values of B_c are hidden under the top layers. Consequently, solving three unknowns (B_c, F_c and $e^{-\mu_c d}$) from a single equation (Eq. 4.4) is totally ill-posed. However, since obtaining the values of $e^{-\mu_c d}$ (namely, the distributions of the thickness of the top layers in the image) is considerably useful for many applications, we intend to relax the constraint by assuming that $B_c = B'_c$. With regard to the assumption, we intend to estimate the top layer's properties based on two cases. The first case is when the input image contains the values of F_c for all different top layers. The second case is when the input image does not contain the values of F_c, yet it contains at least two different bottom layers.

Case One F_c is the reflection of the top layer when it is sufficiently thick so that the reflection of the top layer is not affected by the bottom layer. We assume the values of F_c for each mixed layer are present in the input image and included in the regions marked by users. To illustrate, let us consider the input image in Fig. 4.5. a and the marked regions in Fig. 4.5. b.

The first process is the same as the segmentation method discussed in section 4.4.1. However, unlike the segmentation method, the values of F_c that are the greatest distance from B'_c in the RGB space are the actual values of F_c, since the values between F_c and B'_c represent the color's gradual changes. Having estimated the values of F_c, we can straightforwardly compute the values of $e^{-\mu_c d}$ for every pixel, since Eq. (4.4) becomes closed form. Figs. 4.5. c, d show the result of the estimated F_c and $e^{-\mu_c d}$ for every pixel of the input image. Furthermore, Figs. 4.5. e shows estimated result using straight color line. Notice that this result represents the importance of Spider model, since straight color lines do not work well.

Case Two   Unlike case one, this case does not assume that the input image contains F_c. Instead, it requires the image to contain at least two bottom layers. For clarity, we consider the input image with two bottom layers, as shown in Fig. 4.6. a. Given the input image and its marked regions (Fig. 4.6.b), we intend to estimate the values of F_c, B_c and $e^{-\mu_c d}$ for every pixel.

The first process is to estimate the value of F_c of each top layer. However, unlike the previous case, we can no longer use the greatest distance from B'_c to find F_c, since the input image does not contain the values of F_c. To solve this problem, in the

(a)

(b)

(c)

(d)
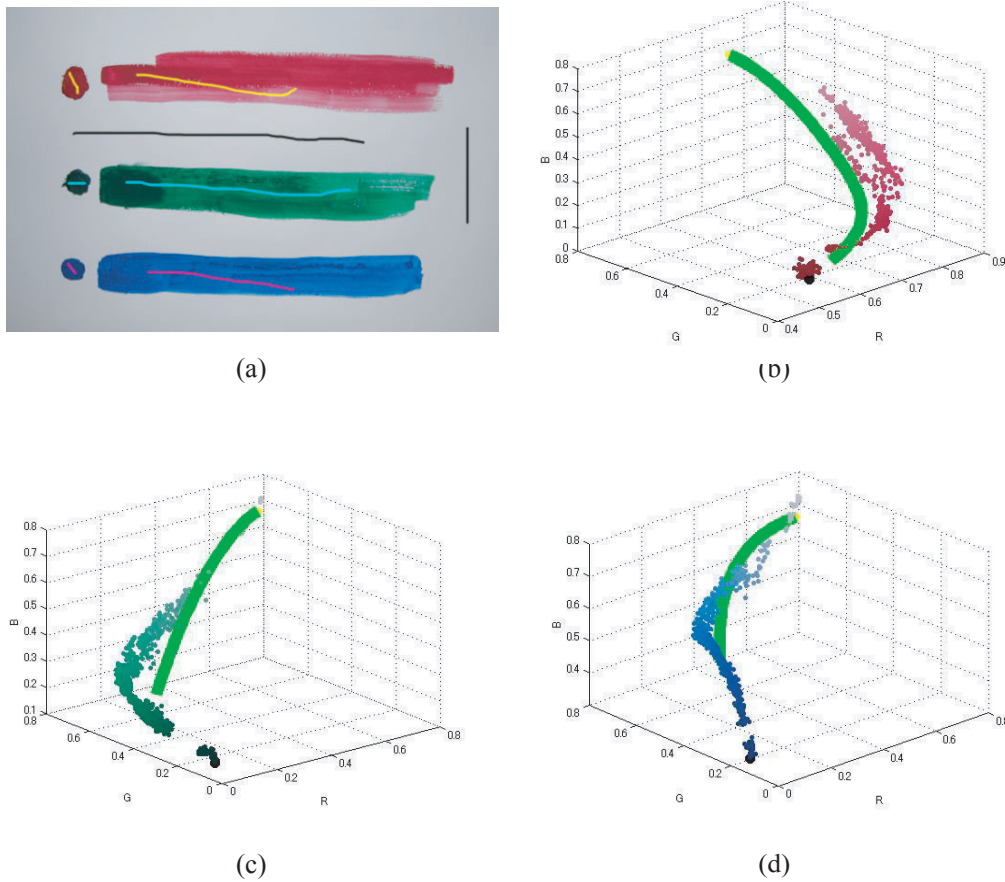
Figure 4.4: Estimated nonlinear color lines of real layered surfaces. (a) Scribbled image. (b) Estimated red color line. (c) Estimated green color line. (d) Estimated blue color line.

RGB space, we plot the intensity values (I_c) of the two mixed layers that have the same color in the top layers yet different colors in the bottom layers (we know this information from the users' marked regions). We fit each of them with the curved line in Eqs. (4.18) and (4.19) using the Lavenberg-Marquardt method. The fitting lines from the two top layers will intersect at a point that represents the value of F_c, as shown in Fig. 4.7. Having estimated the values of F_c, the remaining processes are the same as those of case one. Fig. 4.6. c, d shows the estimated values of F_c, $e^{-\mu_c d}$, respectively.

Note that, aside from using two bottom layers to estimate the top layer's properties, we can also use the same technique to estimate an unknown bottom layer (a totally hidden bottom layer) from two colors of mixed layers, where the intersection will represent the color (or reflection) of the bottom layer.
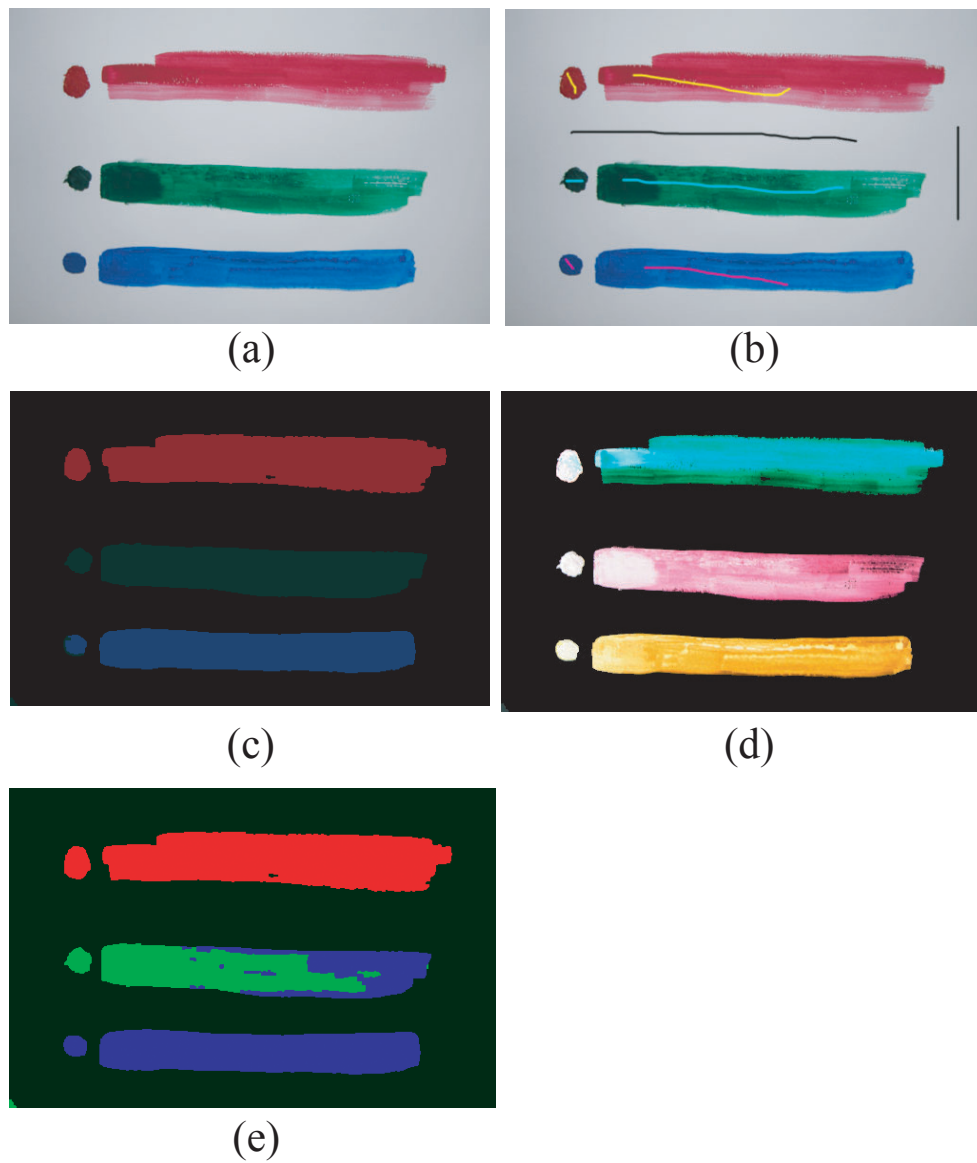
Figure 4.5: Decomposition result: Case one. (a) Input image. (b) Marked regions. (c) F_c. (d) $-e^{\mu_c d}$. (e) Segmentation result using straight color line

4.5   Implementation

In this section, we further discuss the detailed implementation of our proposed method. Again, our goal is to estimate, for each pixel p, the values of top layer's reflection $F(p)$, the bottom layer's reflection, $B(p)$, and the values of $e^{-\mu d}$ from a single input image, with the help of a few users' interactions. Pseudo code 4.5.1 shows the step-by-step processes in our algorithm. In this algorithm, we mainly focus on the
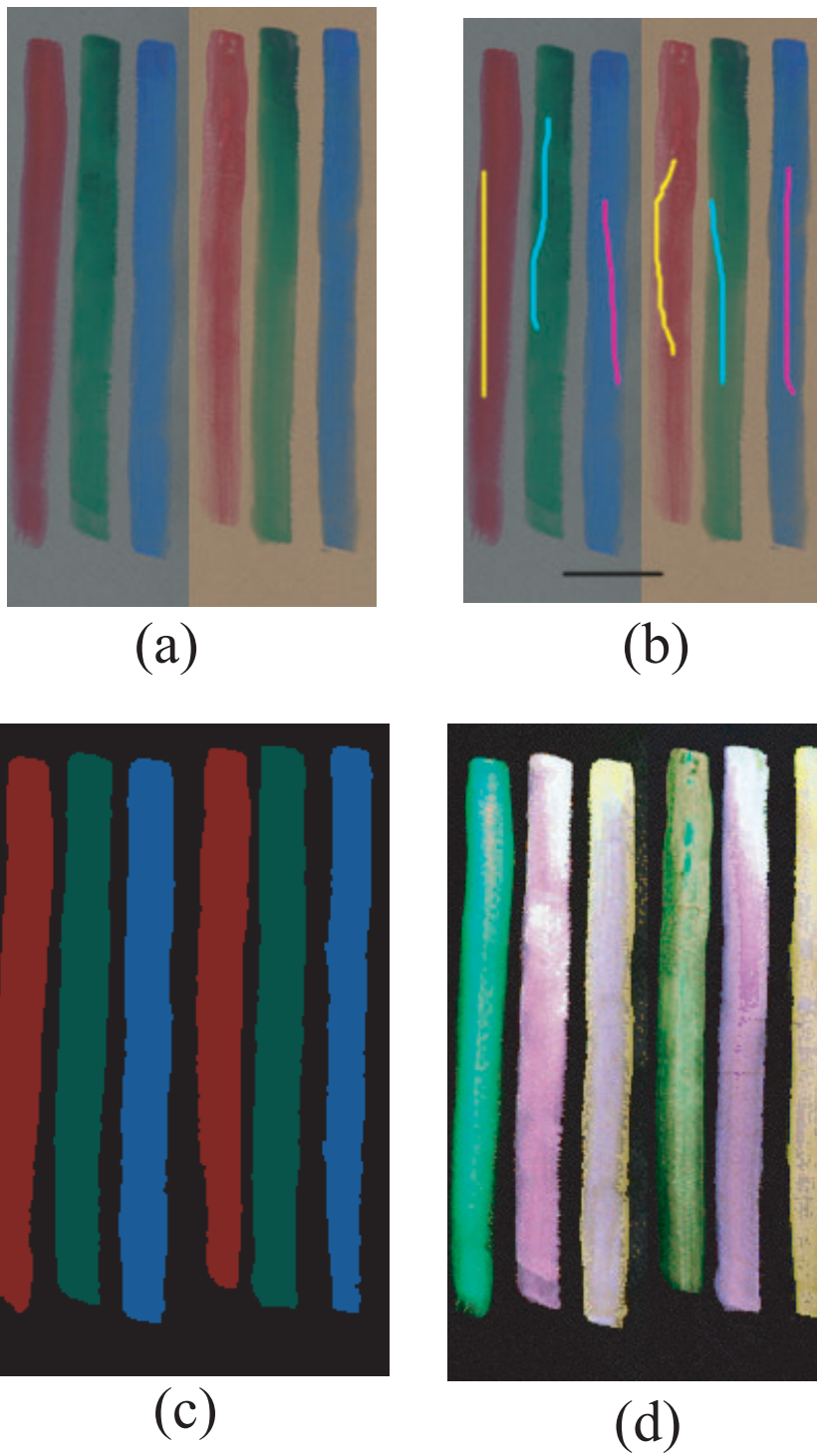
Figure 4.6: Results of Case two. (a) Input image. (b) Marked regions. (c) Decomposed top layers. (d) Decomposed $e^{-\mu_c d}$.

(a)

(b)

(c)
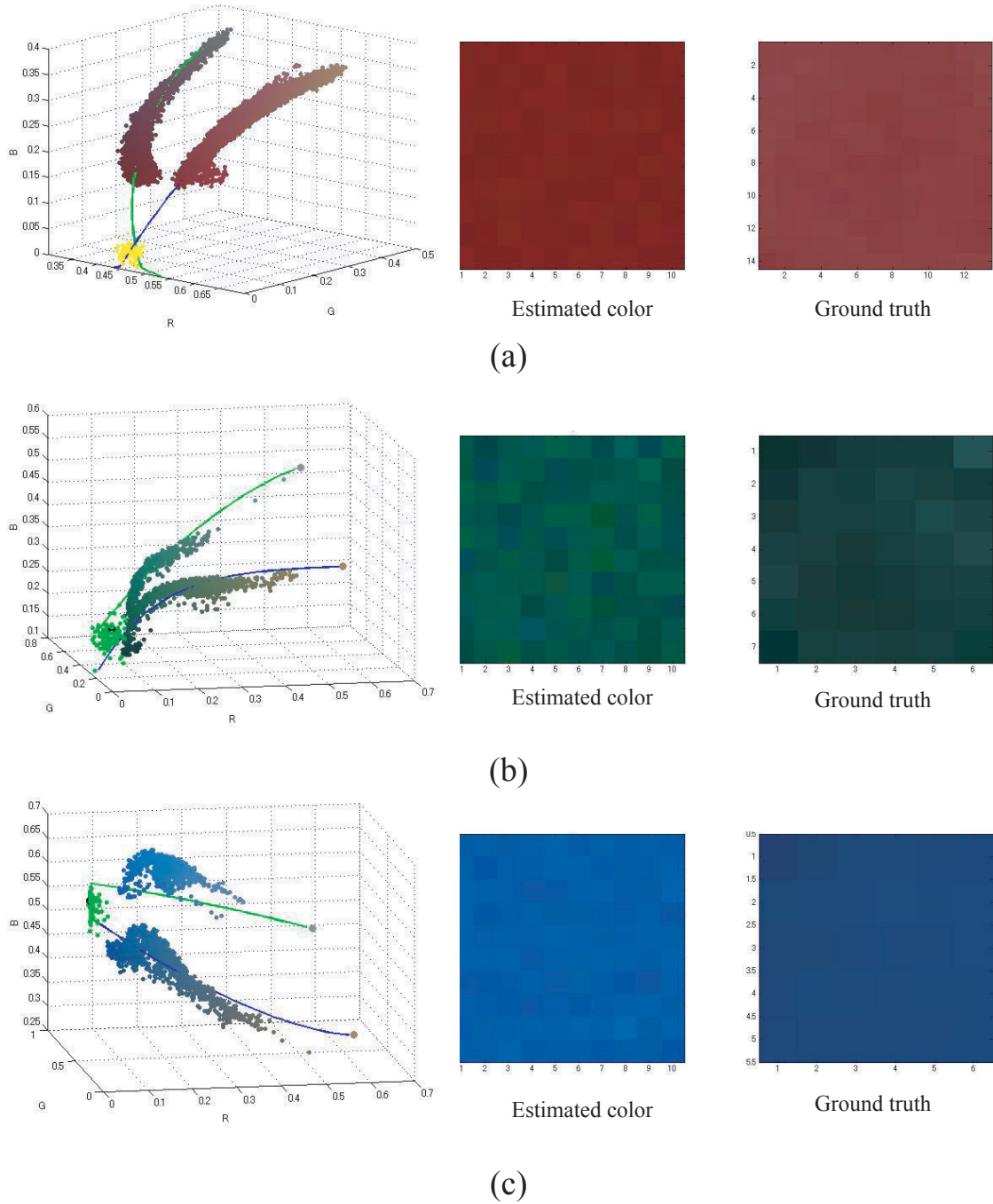
Figure 4.7: Estimation using the intersection of color. (a)(b)(c) Left: Estimated color lines and top layer's color of each colorant in the RGB space. In plot graph, the yellow point is the estimated top layer's color. (a)(b)(c) Middle: Estimated top layer's color. Right: Ground truth

(a)

(b)
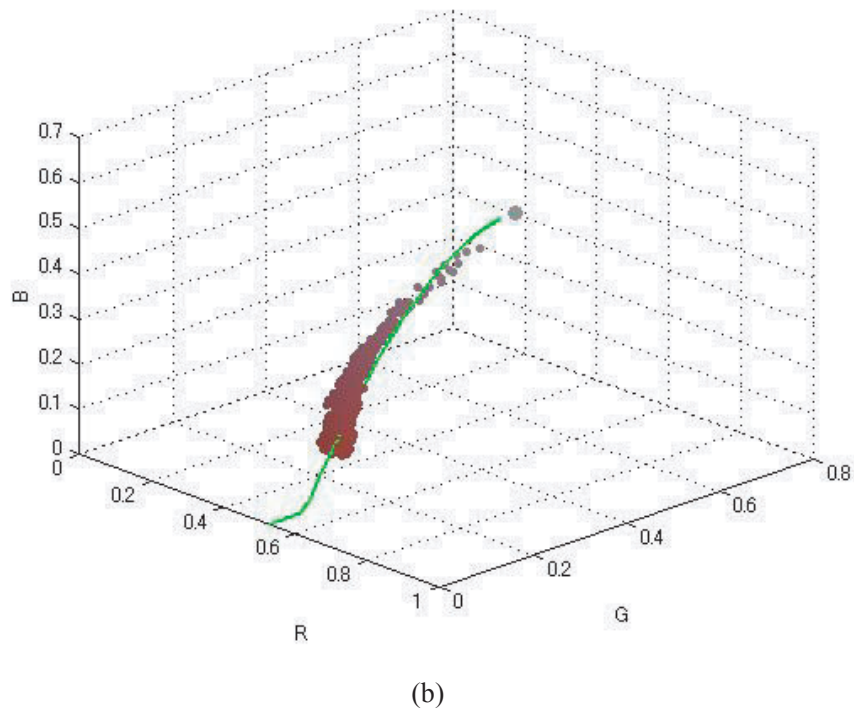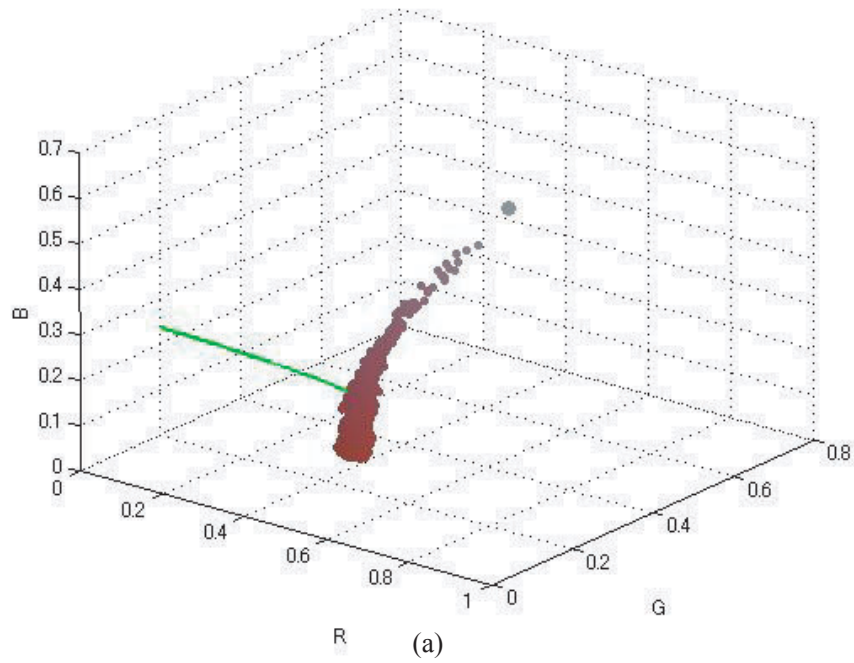
Figure 4.8: Fitting nonlinear color line (a) Case of failure of color line fitting (b) Case of success of color line fitting

segmentation process. Given an input image I_c, in step 1, we ask users to mark the input images based on the mixture reflection and the bottom layers. In step 2, we estimate the value of each top layer F_c. If we have two top layers, then we have two RGB values of F_c. In step 3, we estimate the nonlinear color line using the marked pixels in each of the pixel mixture. We need to observe the following constraints. As shown Figure 4.8. a, if the top layer colorants are red and the channel of the right side of Eqs. (4.14) and (4.15) or Eqs. (4.18) and (4.19) are set to R-channel, the accuracy of estimation does not work well, since the variance of mixed color samples in R-channel is small. Figure 4.8. b shows the result. Therefore, we must select the channel where the variance of samples is the largest.

Algorithm 4.5.1: LAYERED SURFACES DECOMPOSITION($I_{c,i}$)

comment: I_c is the input image

(1) Scribble a few mixed pixels $I_{c,i}$ and bottom pixels B_j
(2) Estimate F_c of each top layer
(3) Compute $\{\psi_c, \gamma_c\}$ in each curved color line
(4) Compute the data term $D(\phi = i|B_i', l_i, p_x)$
(5) Compute the smoothness term $S(\phi_x, \phi_y)$
(6) Do segmentation using MRFs
$$E\left(\{\phi\}, \{B_c'\}, \{l_i\}, \{p\}\right) = \sum_x D(\phi_x = i|B_{c.i}', l_i, p_x)$$
$$+ \sum_{x,y} S(\phi_x, \phi_y)$$
(7) Synthesize each layer's image $F(p), B(p),$ and compute $\alpha(p)$ in a closed-form manner.

In steps 4~6, we segment the layered surfaces image with each colorant using the procedure described in section 4.4.1. The pixels labeled by segmentation are each classified as top or bottom layer. Finally, in step7, each alpha value is calculated in a closed-form manner.

4.6 Experimental Results

Setup In our experiments, we captured images using NIKON D1X, a camera that is radiometrically calibrated to obtain a linear correlation between the incoming light and the image intensities by setting the gamma correction off. We arranged the position of the light source's distance from the objects, and we excluded the possibilities of shadows and interreflections.

Results Figs. 4.10. a and b show, respectively, the input image, and the regions marked by a user. The input image is a water color painting painted by a professional artist. The result of extracted values of F_c for every pixel, which also represent the segmented colors, is shown in Fig. 4.10. d. For better visualization, we colored bottom layer to gray. We compared the result with the extracted foreground of a digital matting method [48], shown in Fig. 4.10. c. As one can observe, the top layer extraction result outperformed the matting method. Figs. 4.10. f and 4.10. h show the result of extracted B_c' and $e^{-\mu d}$, respectively. Fig. 4.10. f is white since it represents the white canvas. Figs. 4.10. e and g show the result of the extracted background layer and opacity by the matting method.

Figs. 4.11~4.18 show the experimental results for a number of real objects.
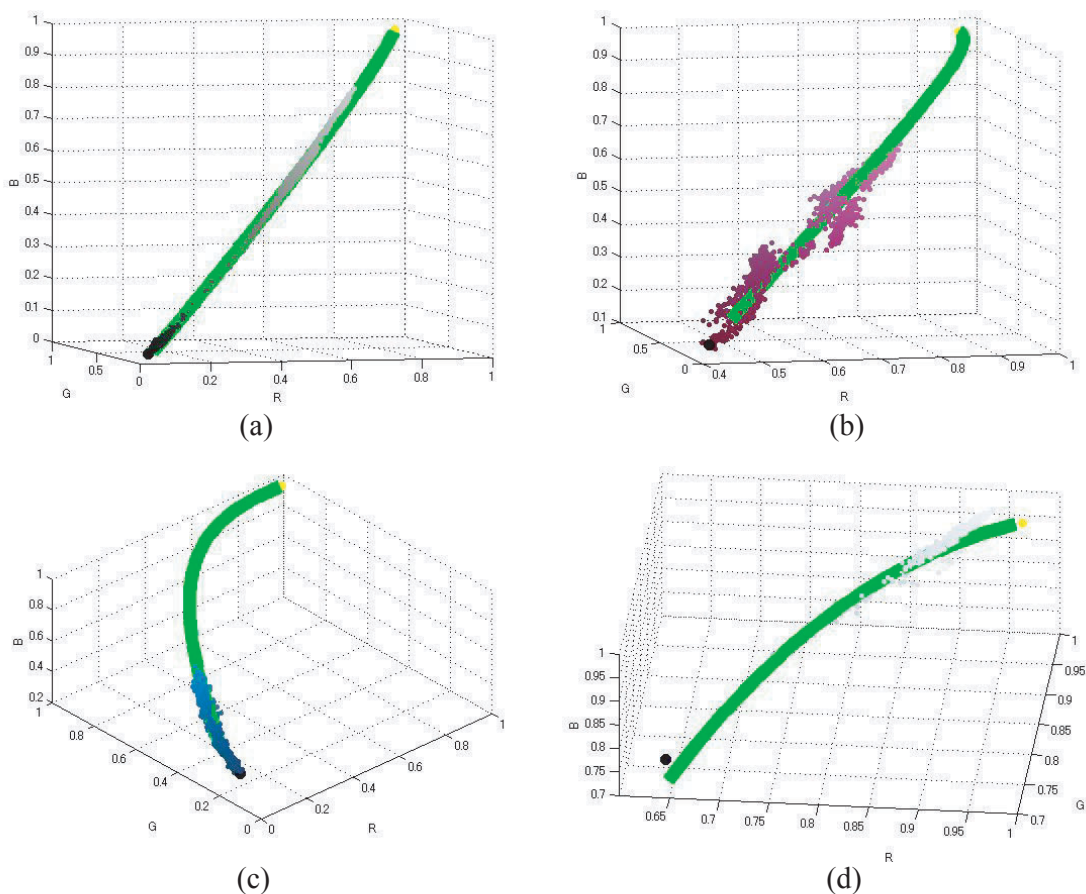
Figure 4.9: Estimated color lines and top layer's color of each colorant in the RGB space. (a) Estimated color line of black colorant. (b) Estimated color line of magenta colorant. (c) Estimated color line of blue colorant. (d) Estimated color line of white colorant.

(a)   (b)

(c)   (d)

(e)   (f)

(g)   (h)
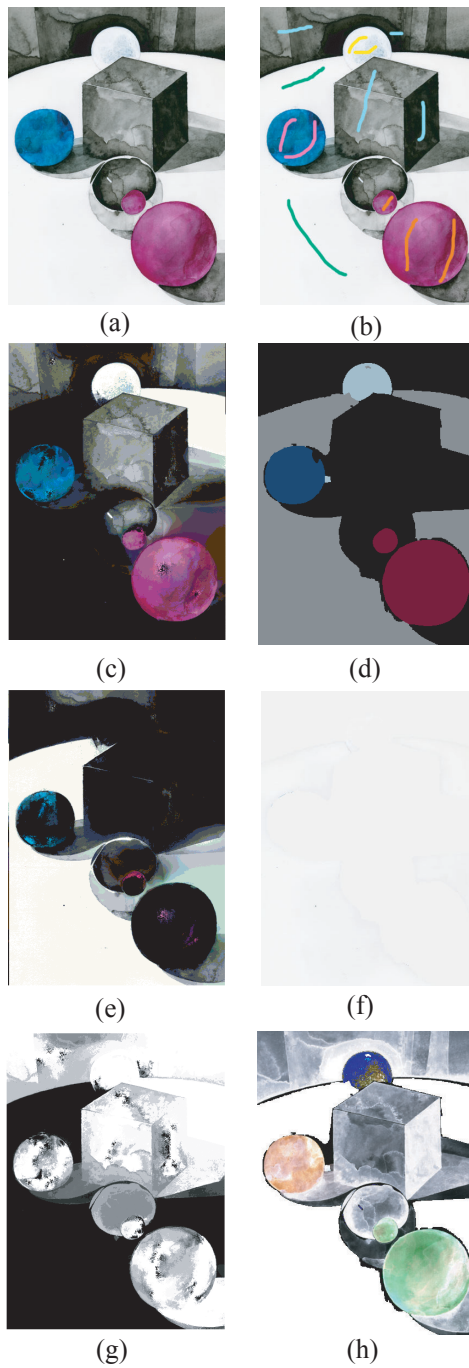
Figure 4.10: (a) Input image: a water color painting painted by a professional artist. (b) Input image with user-specified top and bottom strokes. (c) Extracted top layers by a digital matting method. (d) Extracted top layers by our method. (e) Extracted bottom layer by a digital matting method. (f) Extracted bottom layer by our approach. (g) Extracted opacity by a digital matting method. (h) Extracted $e^{-\mu d}$ by our approach.

(a)

(b)

(c)
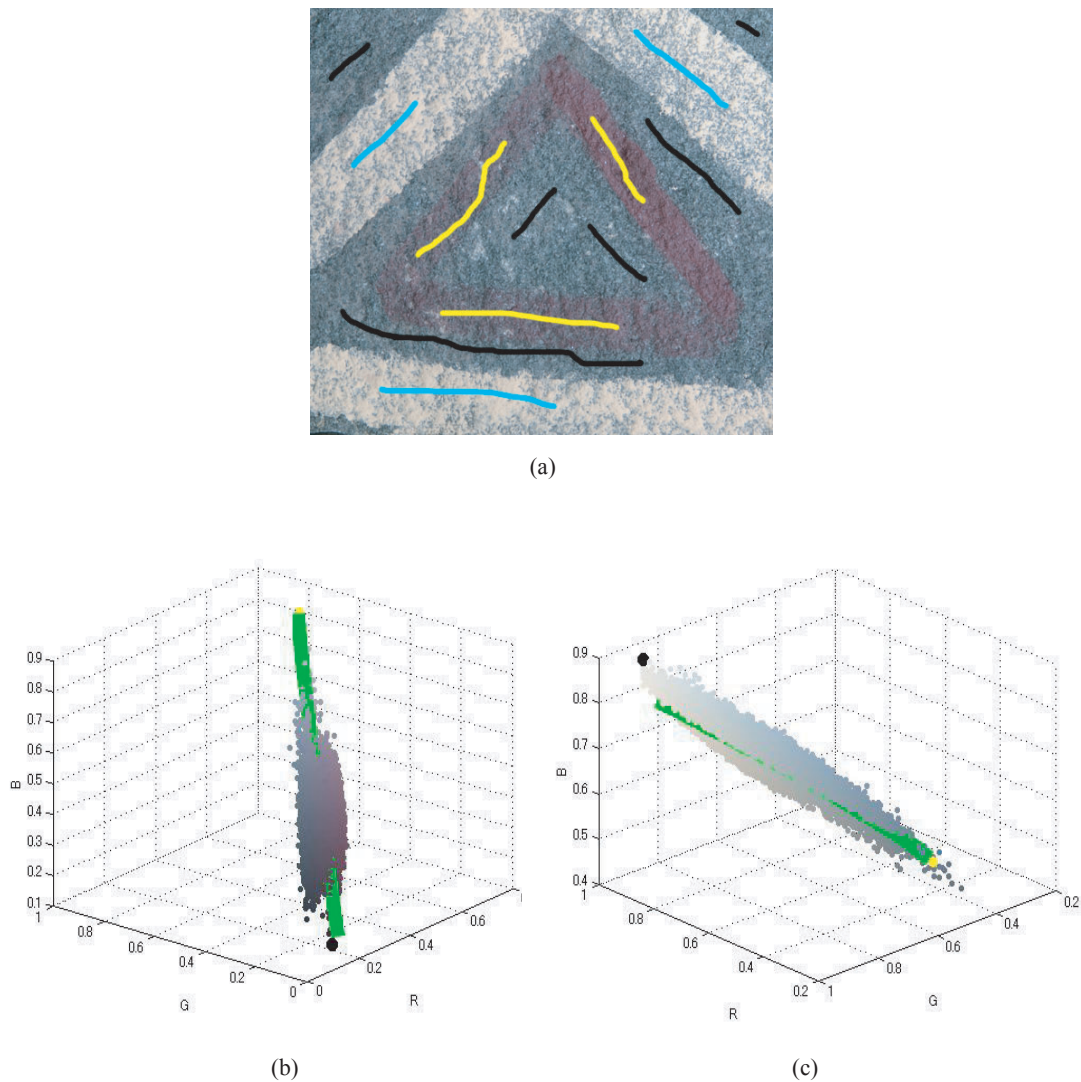
Figure 4.11: Estimated nonlinear color line of layered surfaces with mineral pigments. (a) Scribbled image. (b) Estimated color line of red pigment. (c) Estimated color line of white pigment.

Figs. 4.12 show the results of a rock painting using powdered mineral pigments. Although the bottom layer (the rock) has many slight different colors (like salt and pepper noise), we assume that it has only one uniform color. Consequently, in the estimation of the background (top row, column d), the estimated background is a bit different from the actual bottom layer. Fig. 4.13 shows CG simulation results, which were changed the tone of estimated $e^{-\mu d}$ image.

Fig. 4.15 shows the results for a wall painting of an ancient tumulus. We attempted to restore the wall painting, which had faded by degradation. In Figs.
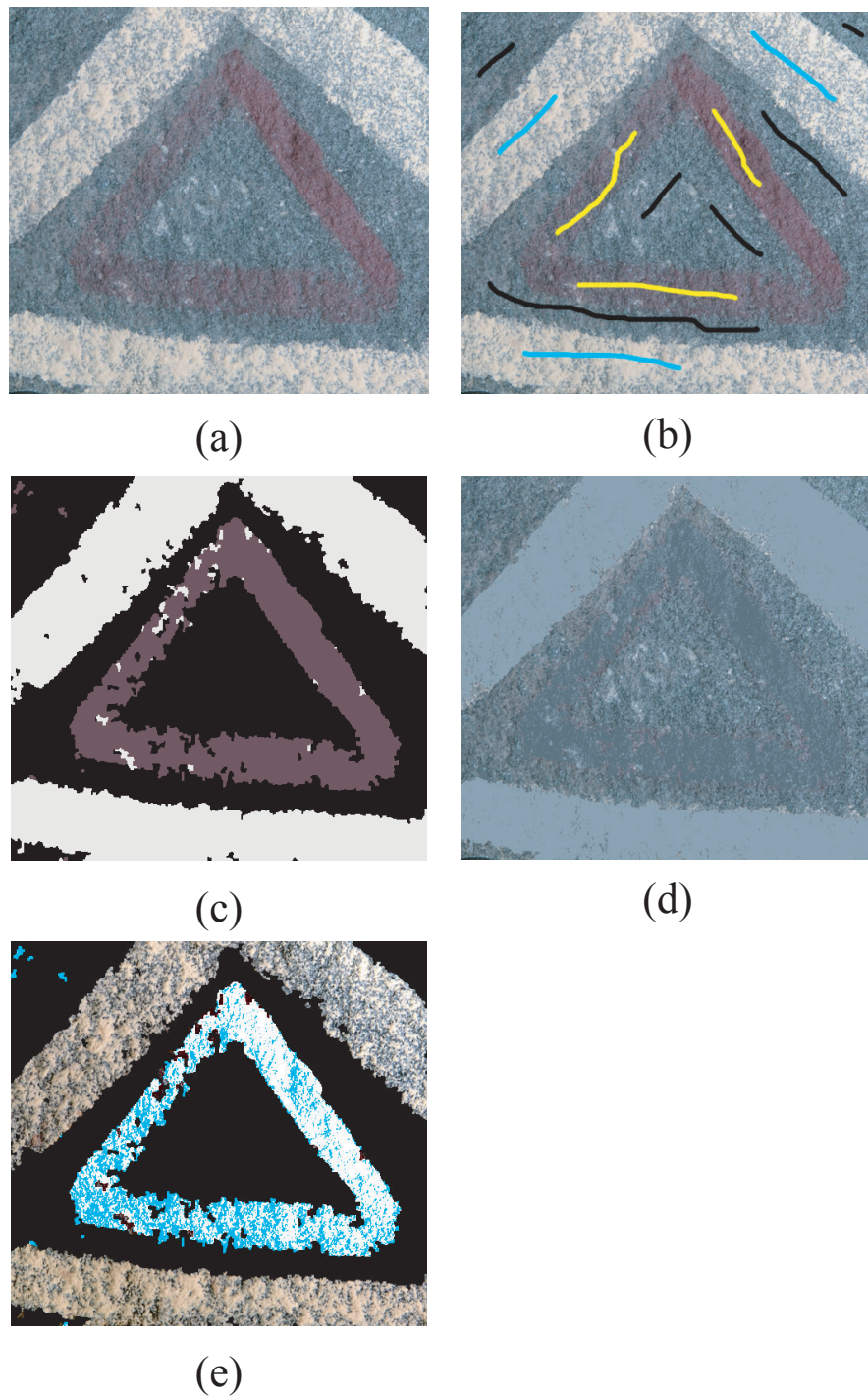
Figure 4.12: Experimental results for layered surfaces with mineral pigments. (a) Input image. (b) Input image with user-specified top and bottom strokes. Black lines are bottom layer markings; the others are mixed layers samples. (c) Estimated top layer image. (d) Estimated bottom layer image. (e) Estimated $e^{-\mu d}$ image.
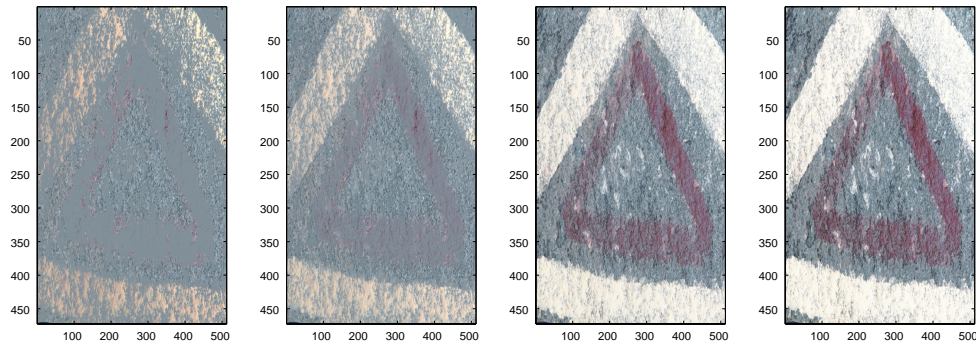
Figure 4.13: CG simulation results of layered surfaces with powdered mineral pigments changing thickness.
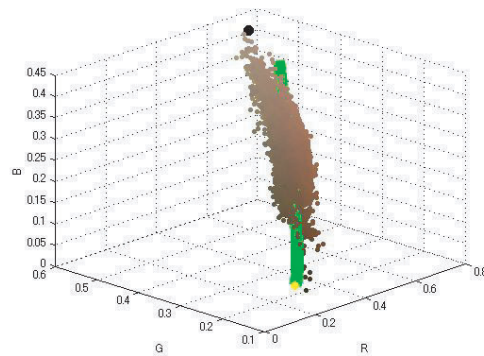
Figure 4.14: Estimated nonlinear color line of wall painting. (a) Scribbled image. (b) Estimated color line.
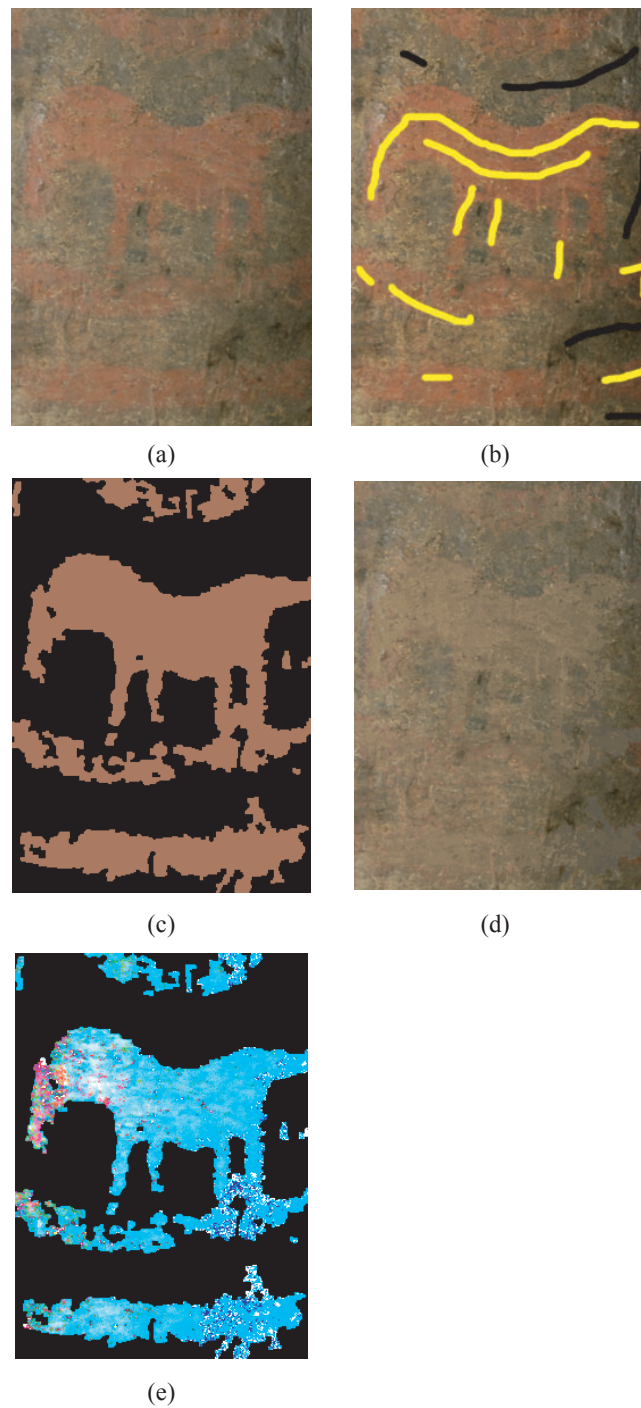
Figure 4.15: Decomposition results of wall painting. (a) Input image. (b) Input image with user-specified top and bottom strokes. Black lines are bottom layer markings; the others are mixed layers samples. (c) Estimated top layer image. (d) Estimated bottom layer image. (e) Estimated $e^{-\mu d}$ images
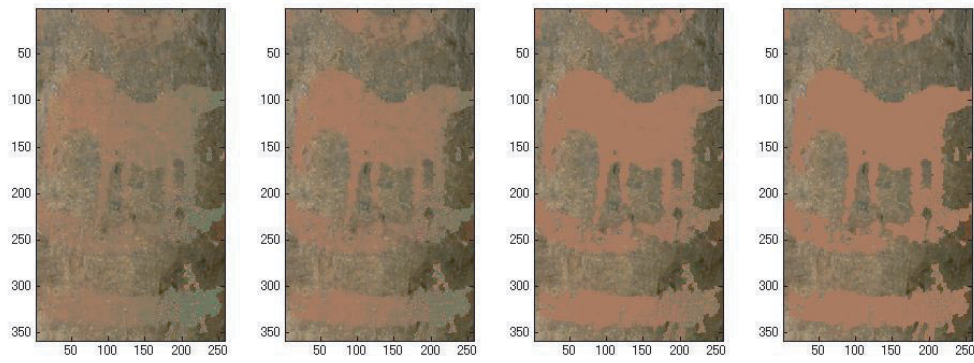
Figure 4.16: CG simulation results of wall painting changing thickness.
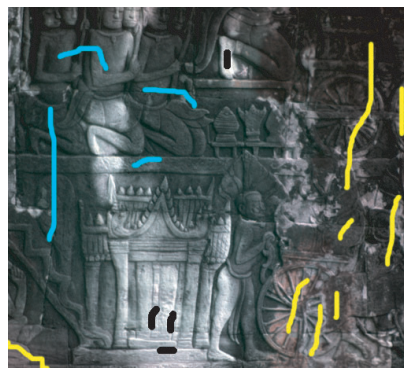
(a)
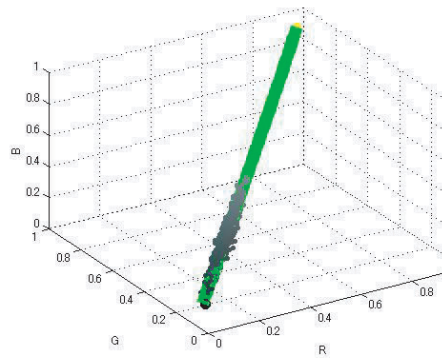
(b)
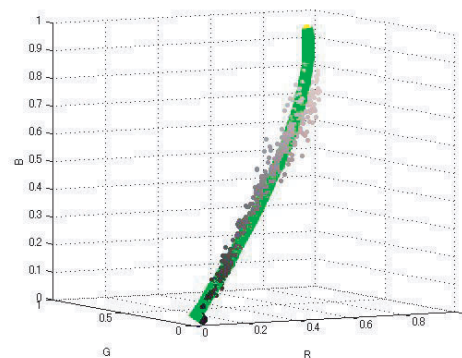
(c)

Figure 4.17: Estimated nonlinear color line of layered surfaces with microorganisims. (a) Scribbled image. (b) Estimated color line of dark green. (c) Estimated color line of dark purple.
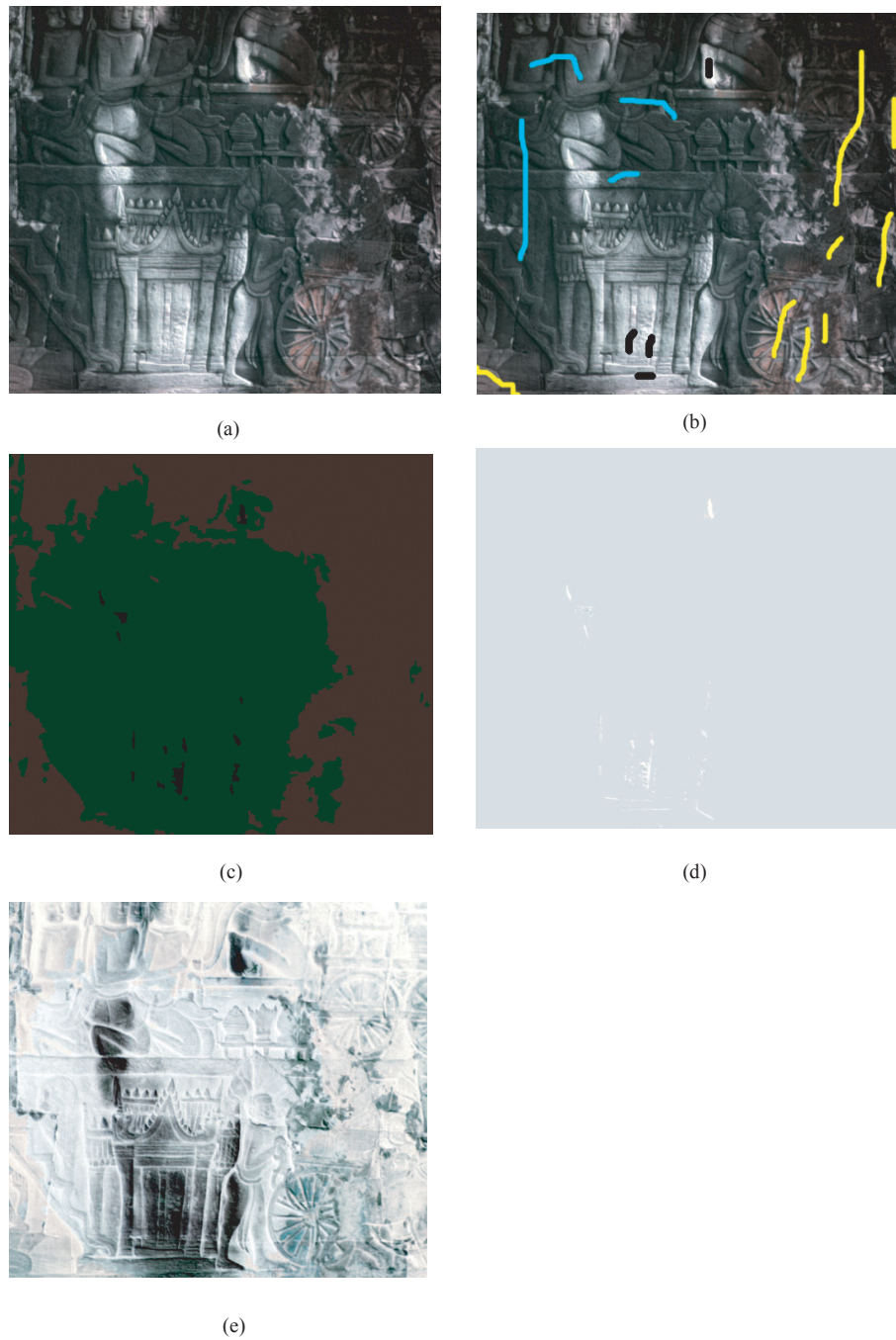
Figure 4.18: Decomposition results for real layered surfaces with microorganisims. (a) Input image. (b) Input image with user-specified top and bottom strokes. Black lines are bottom layer markings; the others are mixed layers samples. (c) Estimated top layer image. (d) Estimated bottom layer image. (e) Estimated $e^{-\mu d}$ image.

4.12, 4.12, and 4.18. c, the extracted top layers, we can observe the painting of a horse more clearly than in the input image. Fig. 4.16 shows CG simulation results, which were changed the tone of estimated $e^{-\mu d}$ image.

Fig. 4.18 shows the results for a relief of an ancient temple, which was degraded by microorganisms. While the surface of the relief is not flat, we applied our method in order to discover the distribution of these microorganisms. In Fig. 4.18. c, the estimated top layer, we can observe how extensively the two different species (the dark purple and the dark green) cover the relief. For better visualization, we increased the brightness of the colors. Figs. 4.12, 4.15, and 4.18.e show the estimated $e^{-\mu d}$ of the input images.

Fig. 4.19 shows the results of applying other methods to the images shown in Figs. 4.12, 4.15, and 4.18. a. Fig. 4.19. a shows the results of a closed form matting method [48]. Fig. 4.19. b shows the results of an object segmentation method [52], and Fig. 4.19.c shows the results of the k-means method. Compared with results of our methods, these results are considerably less accurate.
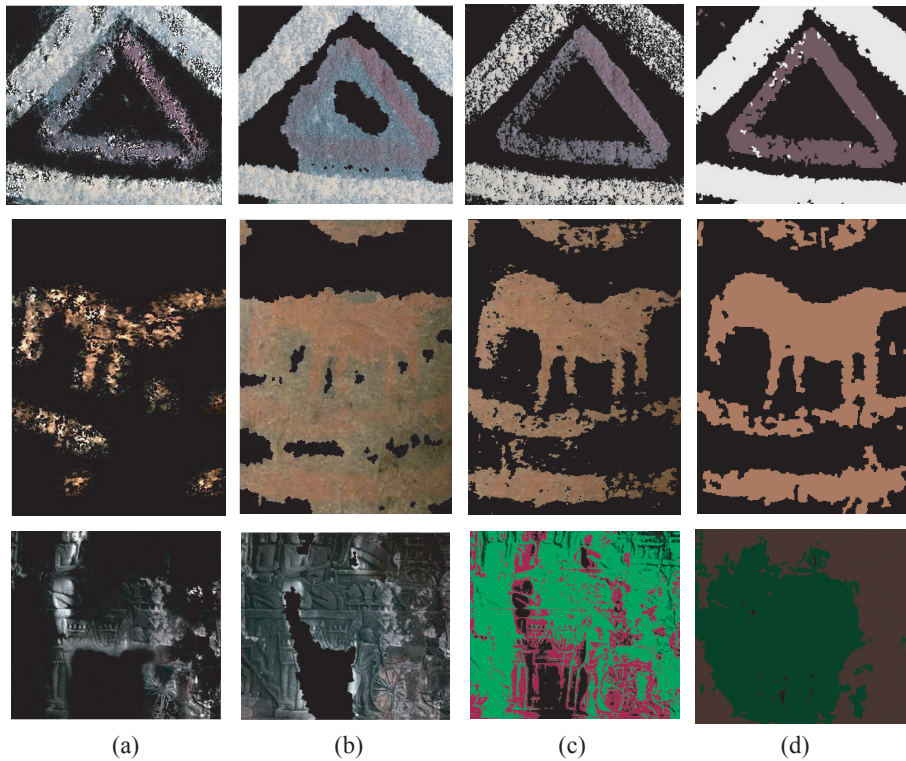
Figure 4.19: (a) Closed-form matting [50] (b) Lazy Snapping [52] (c) k-means (d) Proposed method

4.7   Extended method based on Spectral Information

So far, we described a proposed method based on RGB color. However, we can easily extend the method into a method based on spectral data.

In this section, we describe in detail how to extend our method into a spectral-based method. Futhermore, we employ K/S values, which is the equation of the equation of Kubelka-Munk model [42]. We can estimate some wavelengths without scattering using the following equation:

$$K/S = \frac{(F(\lambda) - 1)^2}{2F(\lambda)} \tag{4.22}$$

where K is the absorption coefficient, and S is the scattering coefficient. When K/S is large, the scattering effect is small. In our experiment, the value of K/S is set at > 0.5. In this way, we can select optimal wavelengths without scattering.

Let $I = I_1(\lambda), I_2(\lambda), \ldots I_i(\lambda), \ldots I_N(\lambda)$, where $I_i(\lambda)$ is an input spectrum of M dimension. $F_i(\lambda)$ is the reflectance spectrum of each top layer F_i. $B(\lambda)$ is the reflectance spectrum of a bottom layer. First, we can calculate the reflectance spectrum $B(\lambda)$ of the bottom layer and reflectance spectra of all top layers $F_i(\lambda)$ as well as we could using an RGB-based method. Second, we can estimate the M' optimal wavelengths by using K/S values. Furthermore, we select the wavelength m having most variance in their wavelengths. Then, we can select E dimensional wavelengths, which are consist of the m and arbitrary $E-1$ wavelengths. However, we do not need to estimate all forms of Eqs.4.26 for segmentation. We can select the number of wavelengths according to computational cost. Third, we estimate nonlinear lines having $E(E < M)$ dimension. It is necessary to use Eqs. (4.14), (4.15) or Eqs. (4.18), (4.19) for estimating nonlinear color lines. Then, we can rewritte Eqs. (4.14) and (4.15) as following the $E-1$ equations:

$$I(E) = F(E) + \psi(E)(I(m) - F(m))^{\gamma(E)} \tag{4.23}$$
$$I(E-1) = F(E-1) + \psi(E-1)(I(m) - F(m))^{\gamma(E-1)}$$
$$I(E-2) = F(E-2) + \psi(E-2)(I(m) - F(m))^{\gamma(E-2)}$$
$$\vdots \tag{4.24}$$
$$I(1) = F(1) + \psi(1)(I(m) - F(m))^{\gamma(1)} \tag{4.25}$$

Eqs.(4.18) and (4.19) can also be rewritten similarly. Next, we segment spectra of each different layer. Then, we use PCA dimension reduction to calculate the affinity

between the pixel's spectrum and bottom layer's spectra. Finally, we can estimate $e^{-\mu(\lambda)d}$ in each pixel, as well as we could do using the RGB-based method.

4.7.1 Experiment and Results

Setup In our experiment, we captured the multispectral image using the LCTF imaging system that is described in chapter3. We also used artificial sunlight((Seric XC-100)). Sample spectra were normalized by an illumination spectrum.

Experiment using Water Color Painting Figs. 4.20~4.22 show the RGB images of decomposed spectra and estimated spectra of each layer. The segmentation accuracy of these results compared favorably with the results of the RGB based-method. Fig. 4.23 shows the comparison of between estimated spectra of top layers and ground truth, and also shows the K/S value of each pigment. Notice that blue and green results have sufficient accuracy, but the red result is less accurate. Fig. 4.23. b shows the K/S values of red pigment. Notice that K/S values are low in error wavelengths. This result implies that a scattering effect is affecting the wavelengths.
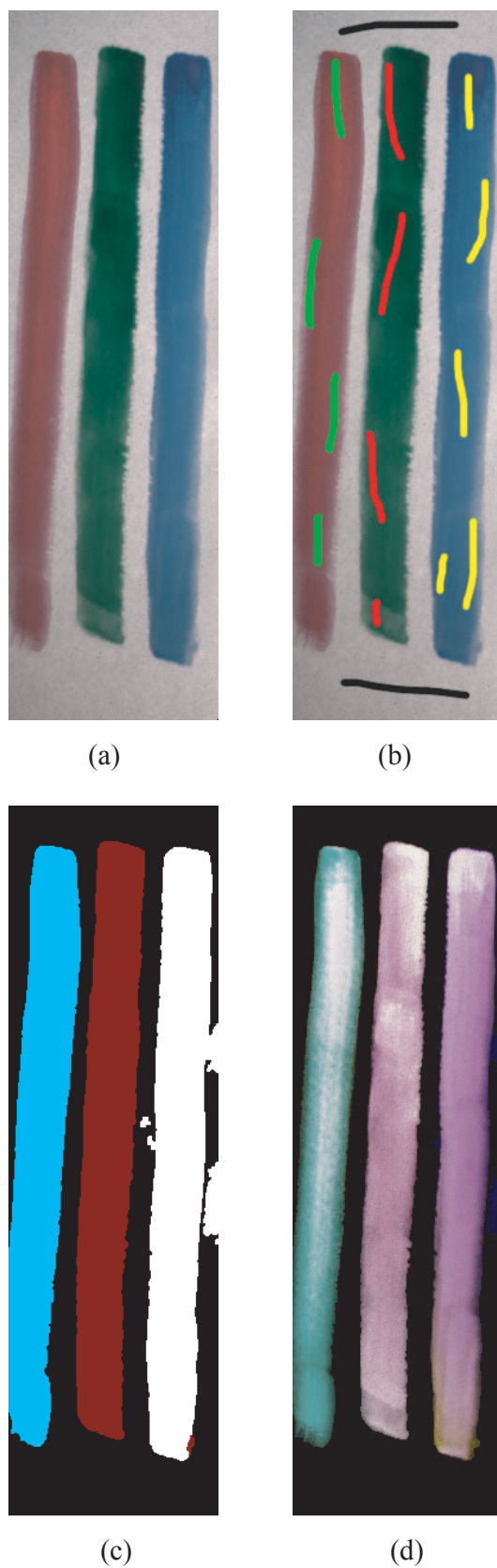
Figure 4.20: Decomposed multispectral images. (a) Input image. (b) Scribbled image. (c) Labeled image. (d) Estimated $e^{-\mu(\lambda)d}$ image.
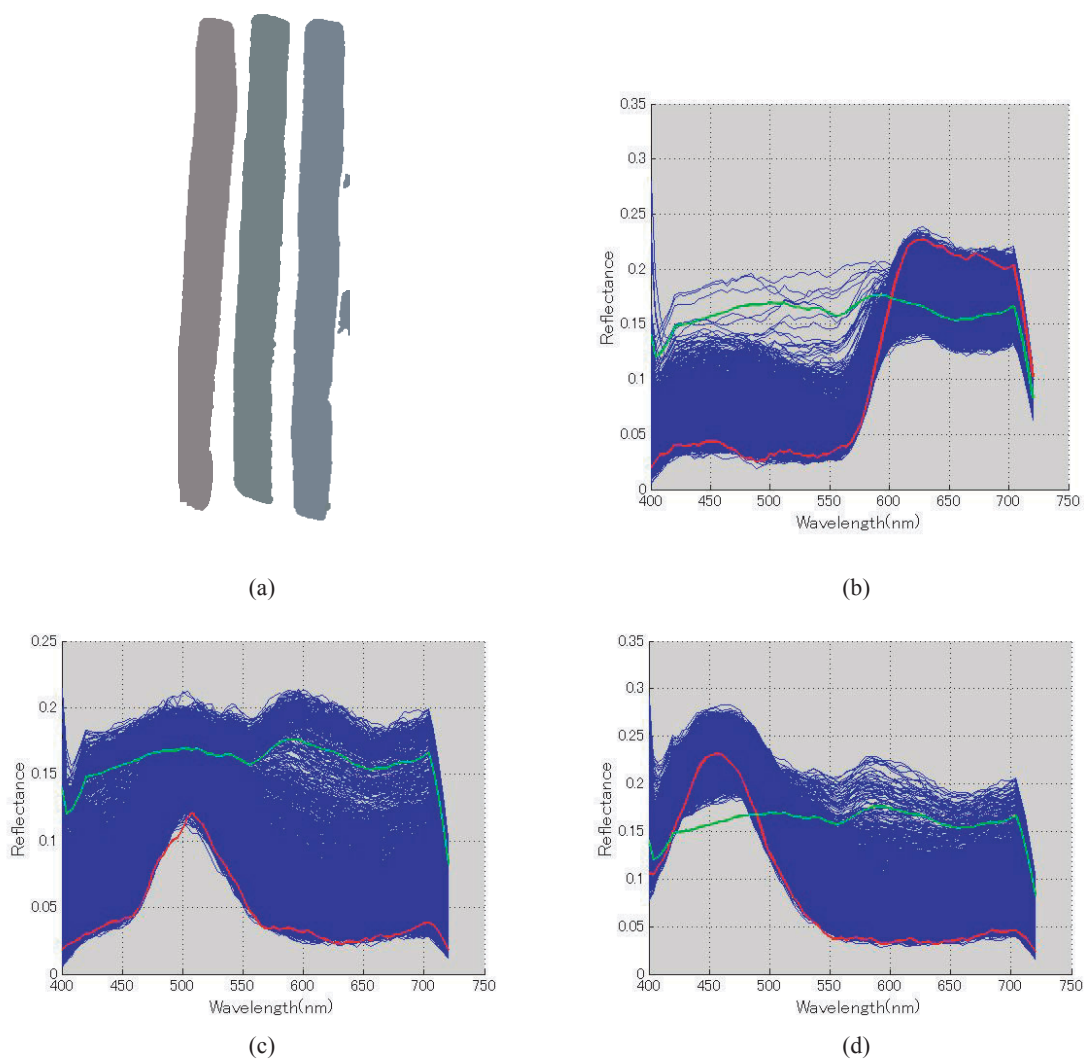
Figure 4.21: Estimated spectra of top layers: blue lines are scribbled sample spectra. Red line is estimated top layer's spectrum. Green line is estimated bottom layer's spectrum. (a) Estimated top layers image. For better visualization, we increased the brightness of the color. (b) Estimated top and bottom spectrum of red pigment. (c) Estimated top and bottom spectrum of green pigment. (d) Estimated top and bottom spectrum of blue pigment.
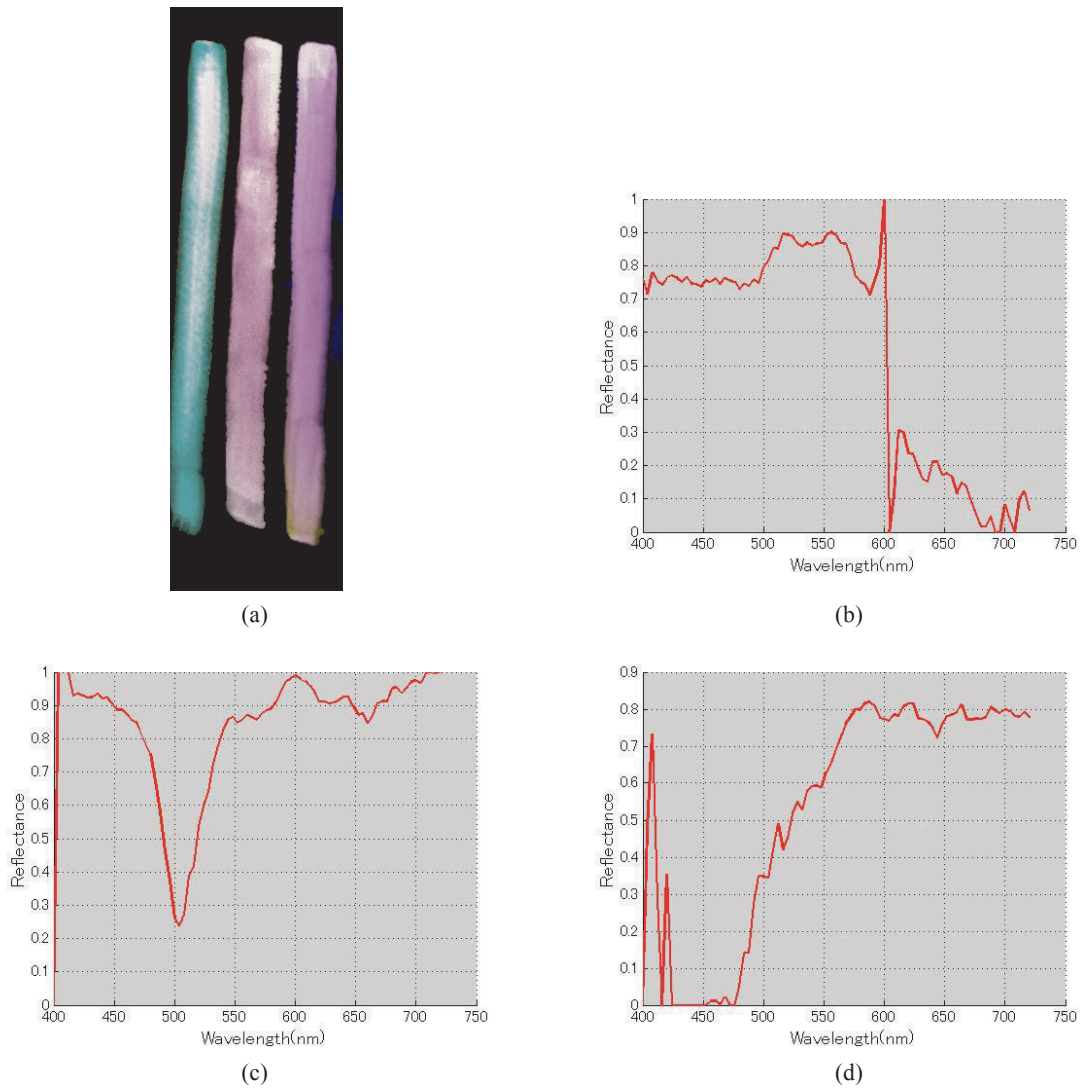
Figure 4.22: Estimated spectra of $e^{-\mu(\lambda)d}$ (a) Estimated top layers image. (b) Estimated $e^{-\mu(\lambda)d}$ spectrum of red pigment. (c) Estimated $e^{-\mu(\lambda)d}$ spectrum of green pigment. (d) Estimated $e^{-\mu(\lambda)d}$ spectrum of blue pigment.
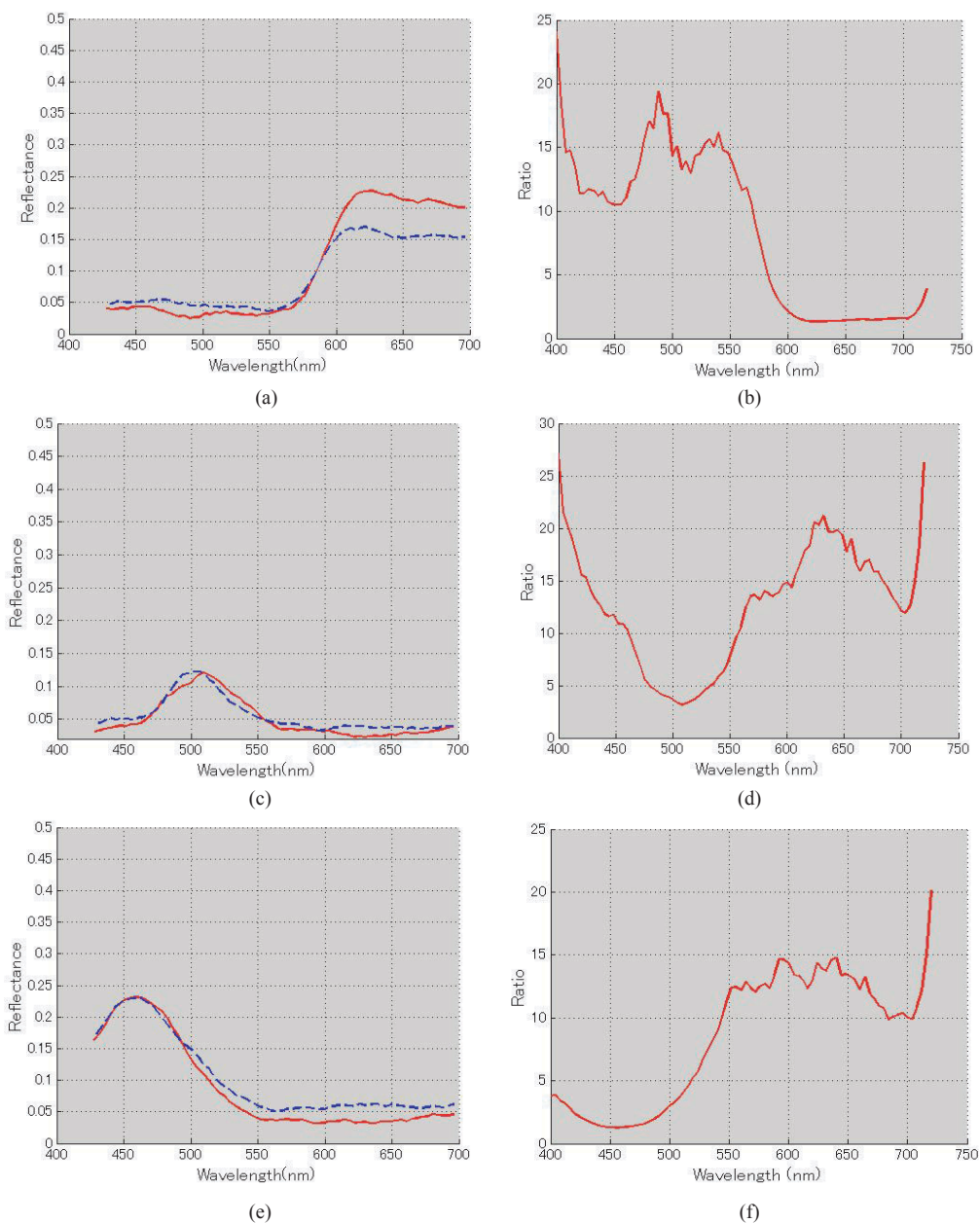
Figure 4.23: Estimated spectra of top layer and K/S values: Red lines of (a), (b), and (c) are estimated spectra. Blue lines of (a), (b), and (c) are ground truth. (a) Red pigment. (b) Estimated K/S values of red pigment. (c) Green pigment. (d) Estimated K/S values of green pigment. (e) Blue pigment. (f) Estimated K/S values of blue pigment.

Layered Surfaces Decomposition for Wall paintings in Noriba Tumulus   We applied our method to wall paintings in the Noriba Tumulus in the Kyushyu area of Japan. The Noriba tumulus is an ancient tomb, made in the 4th century. Several wall paintings resembling triangles and circles were painted by ancient artists in this tumulus.

Using our method, we attempted to extract reflectance spectra of pigments, and to capture the restored shape of deteriorated wall painting. Figs. 4.24~4.27 show the segmented results of two wall paintings and estimated spectra. The result of Fig. 4.24. c showed a circular shape of red pigment. Notice that Fig. 4.24. d and the waveform of Fig. 4.25. d showed a green color that is the opposite of red pigment, showing the absorption spectrum of the pigment.

The result of Fig. 4.26. c also represented the Y shape of a bottom layer. Fig. 4.27 also represented the absorption spectrum of pigment.

However, the results are not sufficiently accurate for reproducing a wall painting. Such surfaces are not flat, and they involve many kinds of grime.

4.8   Summary

We have proposed and demonstrated a novel segmentation method for layered surfaces. Unlike most existing segmentation methods, our method is able to segment the colors correctly even when they change gradually. This success is mainly a due to the nonlinear correlation (Eq. (4.14) ~ (4.19)) between color channels in estimating the reflectance of the top layers.

In addition to segmentation, we also proposed a technique to estimate the optical properties of the top and bottom layers for every pixel in the input image for certain levels of approximation. We consider these approximated estimations could benefit many applications in computer vision and graphics. Experiments with real images showed the effectiveness and the robustness of our proposed method.

Futhermore, we extended our study to a spectral-based method. This method allowed decomposition of optical properties based on spectral information from layered surfaces.
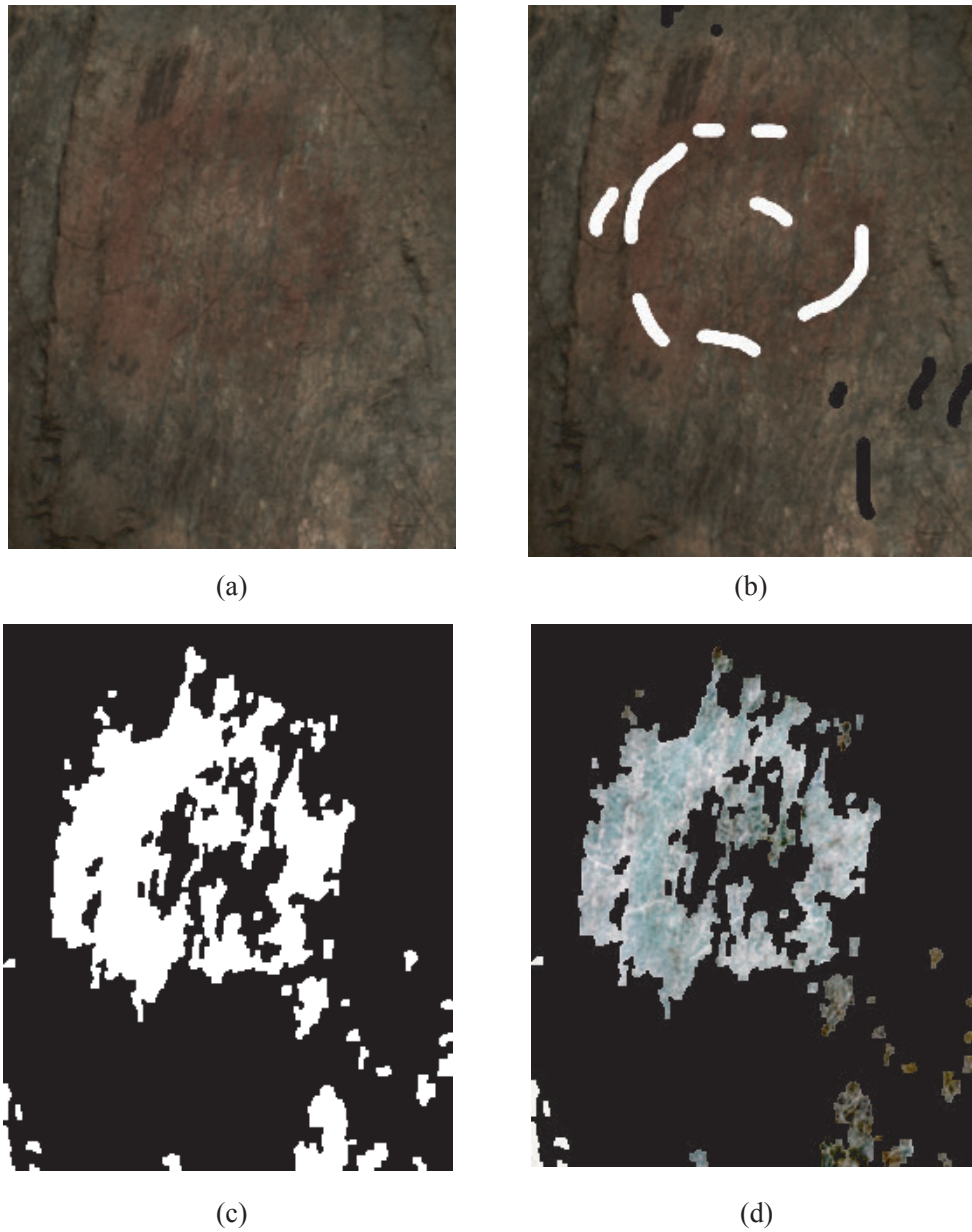
Figure 4.24: Decomposed multispectral images of Noriba tumulus 1. (a) Input image. (b) Scribbled image. (c) Estimated labeled image. (d) Estimated $e^{-\mu(\lambda)d}$ image.
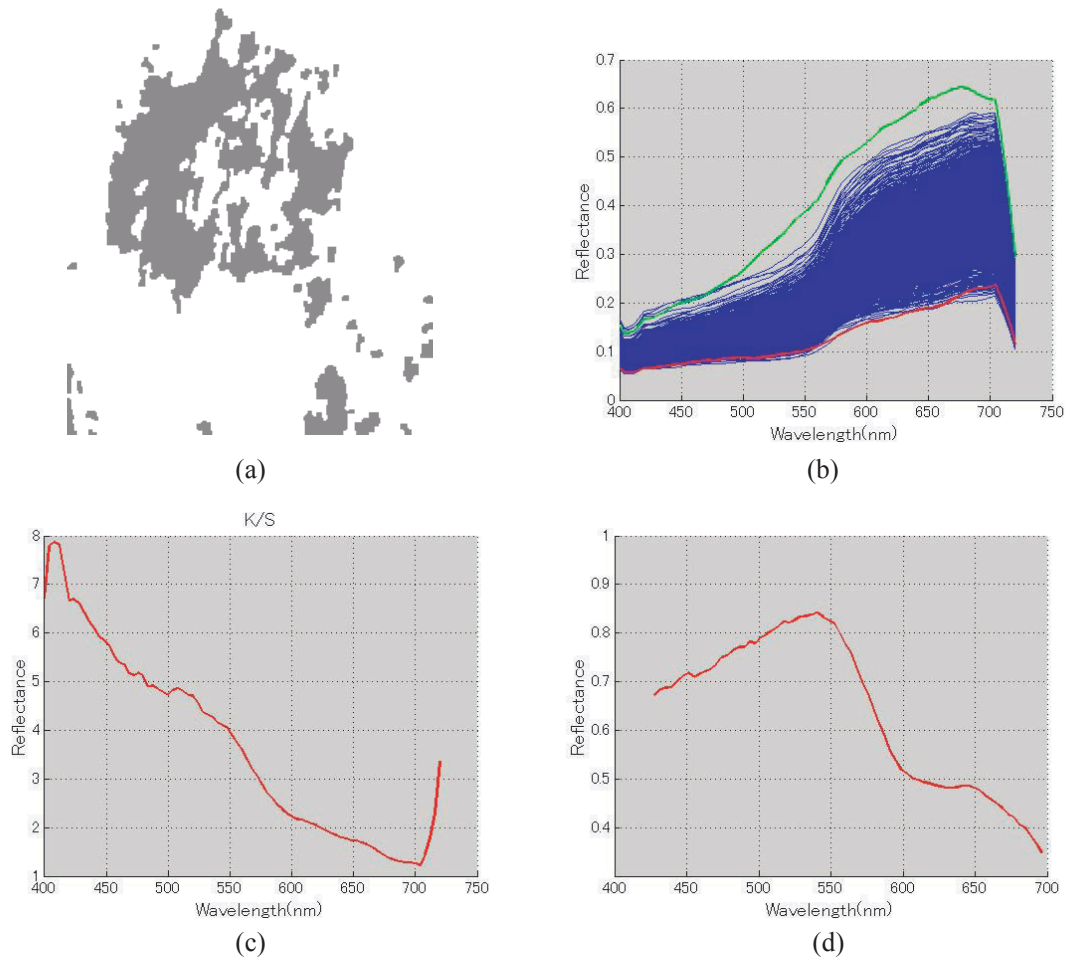
Figure 4.25: Estimated spectra of Noriba tumulus 1. (a) Estimated top layers image. To improve visualization, we increased the brightness of the color. (b) Estimated $e^{-\mu(\lambda)d}$ spectrum of red pigment. Blue lines are scribbled sample spectra. Red line is estimated top layer's spectrum. Green line is estimated bottom layer's spectrum. (c) Estimated K/S values. (d) Estimated $e^{-\mu(\lambda)d}$ spectrum of the pigment.
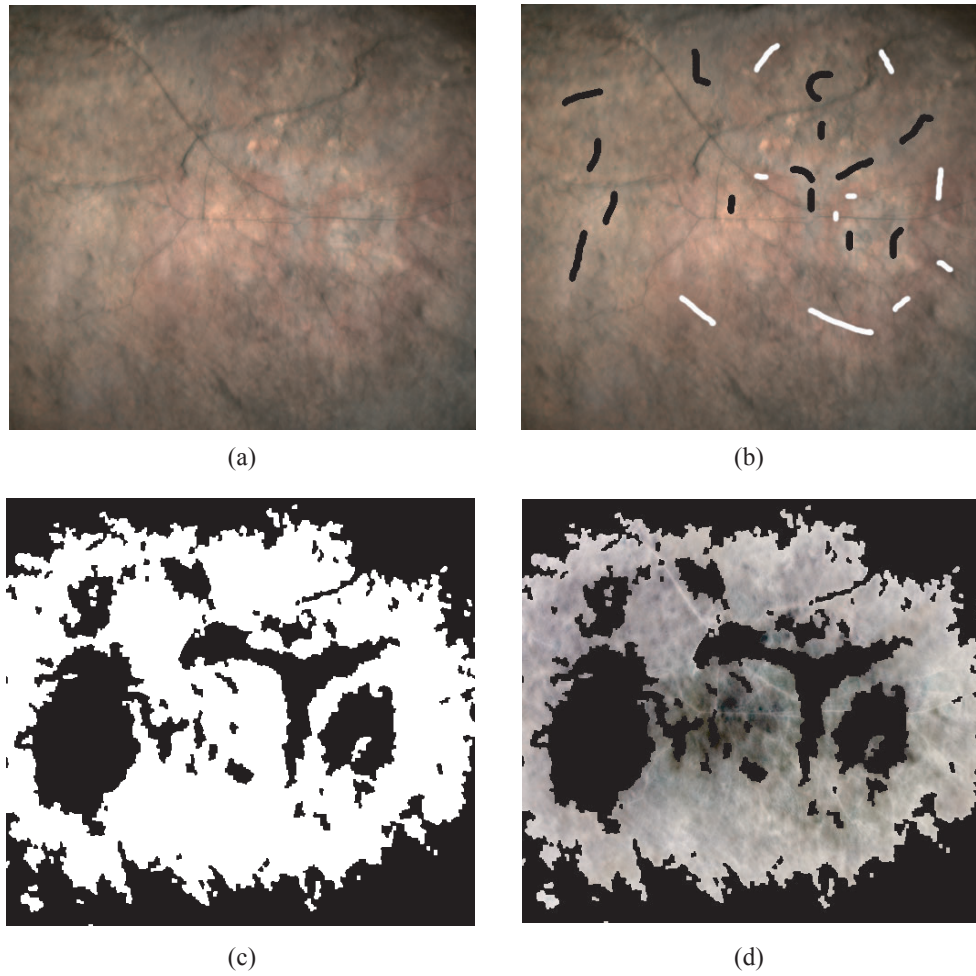
Figure 4.26: Decomposed multispectral images of Noriba tumulus 2. (a) Input image. (b) Scribbled image. (c) Estimated labeled image. (d) Estimated $e^{-\mu(\lambda)d}$ image.

(a)

(b)

(c)

(d)
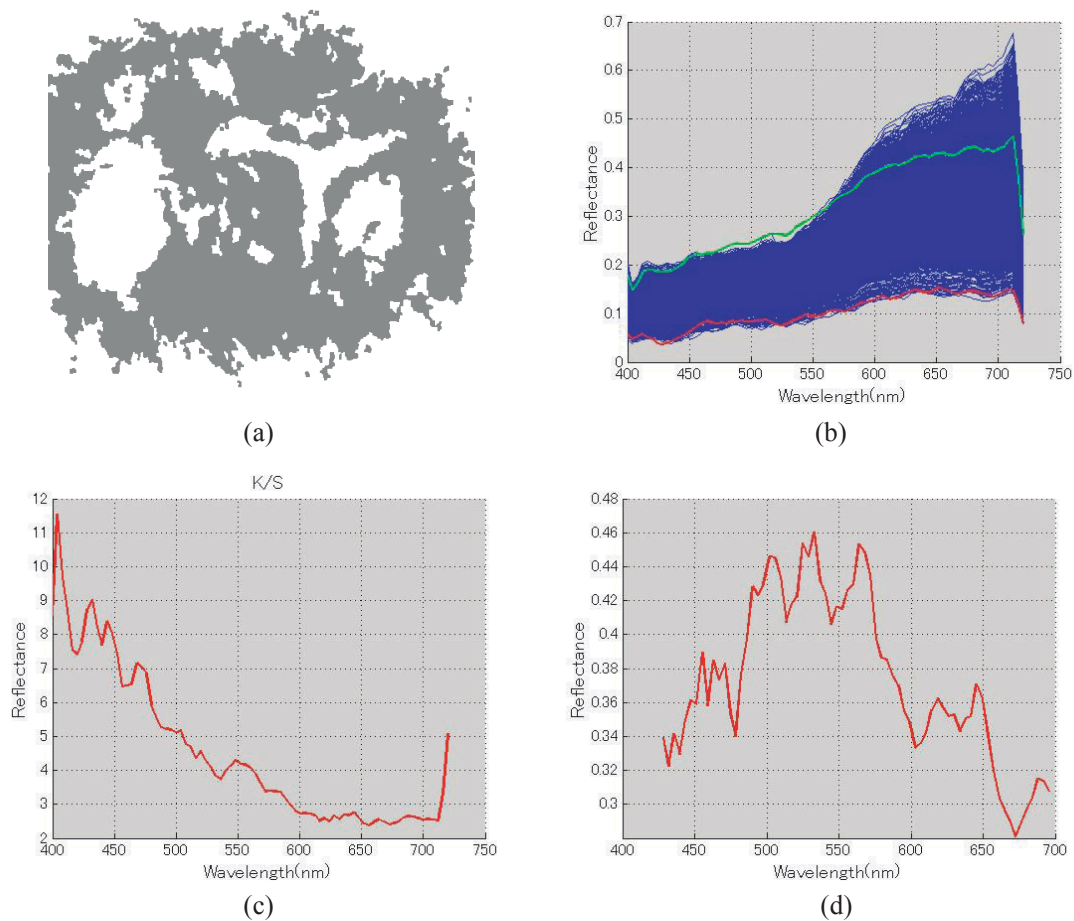
Figure 4.27: Estimated spectra of Noriba tumulus 2. (a) Estimated top layers image. To improve visualization, we increased the brightness of the color. (b) Estimated $e^{-\mu(\lambda)d}$ spectrum of red pigment. Blue lines are scribbled sample spectra. Red line is estimated top layer's spectrum. Green line is estimated bottom layer's spectrum. (c) Estimated K/S values. (d) Estimated $e^{-\mu(\lambda)d}$ spectrum of the pigment.

Chapter 5

Conclusions

5.1 Summary

The ultimate purpose of this dissertation is the development of reflectance analysis methods using a multispectral image and yielding practical applications for modeling cultural assets. Basically, our task involves the development of multispectral imaging systems and methods that analyze reflectance spectra on an object's surface.

First, we developed two multspectral imaging systems: one method can easily produce multiple multispectral images for making a VR model based on sensor fusion procedure, and another method can obtain a single multispectral image of a wide area in an outdoor environment.

Next, because the surface structure of our target object has layered surfaces, we faced the challenging task of analyzing spectral reflectance of layered surfaces. We introduced a multispectral image segmentation method based on a statistical procedure for layered surfaces. Furthermore, we proposed a novel method that can segment and estimate the optical properties each layer based on a physics procedure, and we also proposed a new layered surface model. The layered surfaces decomposition method remains to be proposed.

Finally, we applied these methods to applications for modeling cultural assets.

5.1.1   Color Restoration Method Based on Spectral Information Using Normalized Cut

We are proposing a practical color restoration method based on spectral information. The method can restore color of many texture images by using both high resolution images captured by DSC and spectral information captured by a conventional spectrometer: we can synthesize spatially approximate multispectral images. Restored multispectral images have high resolution and accurate color information.

Unlike conventional methods, the method can be flexible about the environment for obtaining input data. For example, DSC images and spectral information can be obtained under different illumination environments: we do not need to obtain these data simultaneously. Also, we can share our database of spectral reflectance with archaeologists.

The method works efficiently in making a VR model of digital archive contents that satisfies requirements for automation, mobility, color accuracy, and computational cost. We further applied our method to digital archive contents and were able to realize textured images.

5.1.2   Multispectral Imaging for Material Analysis in an Outdoor Environment Using Normalized Cuts

We have developed a new multispectral imaging system in which obtained multispectral images have a spectrum of sufficient spectral resolution in each pixel. Futhermore, the system can capture a multispectral image in wide area at once.

We have also proposed a multispectral image segmentation method, since the different materials can be classified by segmenting different spectra. The proposed method can handle object surfaces having complex reflection based on a statistical procedure.

Our experimental results show the effectiveness for layered surfaces compared with conventional methods. We applied the system and segmentation method to the data from the bas-relief of the Bayon Temple in the Angkor ruin, and identified the class and distribution area of the microorganisms. This method can work well without the adverse effects of layered surfaces such as mixture of colors, absorption, scattering, and shading.

5.1.3 Decomposing Complex Reflection Components of a Layered Surface Using the Spider Model

We have proposed a novel physical model called the "Spider" model that can deal with color changes of layered surfaces and also decompose optical properties of each layers. The proposed model can represent the gradual color changes due to the change of optical properties of layered surfaces based on the Lambert-Beer (LB) based model. Unlike most existing segmentation methods, the proposed decomposition method cannot only segment the colors correctly even when they change gradually, but can also estimate the top layer's reflectance and optical properties, and the bottom layer's reflectance. To be able to decompose layered surfaces is extremely useful for object analysis. Furthermore, there are no methods sharing our goals and techniques. We have developed methods for both an RGB image and a multispectral image.

5.2 Contributions

In this dissertation, we have proposed a framework using a multispectral image for reflectance analysis of layered surfaces. Our framework involves both multispectral image acquisition and reflectance analysis. For multispectral imaging systems, we have proposed two systems: a sensor fusion based system and a panoramic multispectral imaging system. For reflectance analysis, we have proposed two methods: a statistics based method and a physics-based method. Our contribution can summarize as follows:

1. **Development of a practical color restoration method based on spectral information**
   In the color reproduction field, many multispectral imaging methods have been proposed. However, their methods target a small object such as an oil painting, a vase, and a human face. Our method can map many texture images onto a large 3D object. The method can efficiently work in making a VR model of digital archive contents that satisfies requirements of automation, mobility, color accuracy, and computational cost.

2. **Development of a multispectral imaging system that efficiently acquires spectra in a wide area in an outdoor environment**

We have developed a multispectral imaging that can efficiently obtain a multi-spectral image in a wide area. The developed system involves both hardware design and a measuring method produced by software design.

Cultural assets are often located in severe outdoor environments in which wide alterations on the illumination environment often occur quickly, causing saturation and underexposure in obtained images. Our measuring method can estimate optimum exposures based on noise analysis of the system.

3. **Development of a method that segments a multispectral image of layered surfaces**

   In computer vision, many segmentation methods have been proposed. However, there are few multispectral image segmentation methods dealing with the characteristics of layered surfaces. We introduced the relation between the kernel method and the characteristics of layered surfaces, and also developed a multispectral image segmentation method using NCuts based on the kernel method for layered surfaces. We applied our method to analysis of microorganisims of bas-reliefs in the Bayon Temple, and our experimental results showed its effectiveness compared with conventional methods.

4. **Proposing a novel layered surface model**

   In computer vision, most methods using the LB-based model such as digital matting, vision in bad weather, and underwater vision, do not considered the nonlinearity between color channels changing a layer's color: color lines are assumed to represent straight lines because it is assumed that the pixel's opacity is scalar, regardless of the nonlinear absorption of color in layers. This assumption is not accurate for colored layered surfaces, since the observed color of layered surfaces changes depending on the thickness of the layer. We could also extend this model to both RGB images and multispectral images. Furthermore, we think the proposed Spider model can be applied to other objects having negligible scattering.

5. **Development of a method that decomposes each layer's optical properties**

   We have developed a decomposition method that applies to complex reflection components of layered surfaces using the Spider model. In computer vision, most methods cannot segment color of layered surfaces, since they assume surface color is a solid color or a Lambertian surface. However, using the

Spider model, we can effectively segment the color of layered surfaces, and can also estimate the properties of the top and bottom layers of the image.

We consider these estimations could benefit many applications in computer vision and graphics. Experiments with real images showed the effectiveness and the robustness of our proposed method. This method could also be extended to a multispectral image.

5.3 Future Directions and Discussions

In this dissertation, we have proposed some techniques for reflectance analysis of layered surfaces using a multispectral image. In this section, we describe future directions of our approaches, and also discuss how to improve the methods for increasing the precision of analysis.

5.3.1 Real time rendering based on spectral information

Our proposed color restoration method succeeded in producing many multispectral images consisting of sparse spectra. We think it is possible to render images based on spectral information in real time. This idea can be used to simulate objects under arbitrary illumination in digital archive contents.

5.3.2 Development of an omnidirectional multispectral imaging system

For archive purposes, we could capture a panoramic multispectral image using an automatic pan/tilt platform. However, to capture an omnidirectional multispectral image, this system would take about 12 hours. We think it is possible, by improving the optics of an LCTF imaging system, to reduce this time considerably.

5.3.3 Layered surface decomposition for 3D objects

We intend to solve our current constraints regarding flat surfaces. The Spider model can easily extend 3D surfaces, since the brightness of each pixel in a multispectral image depends not on waveform of the spectrum but only on geometry. Using an inverse lighting technique, we think we can handle a 3D surface.

5.3.4   Layered surface decomposition considering scattering

The proposed method assumes the layered surfaces have no scattering coefficients or the scattering coefficients are negligible. We intend to increase the parameter estimation by using a more complex model such as the KM model. However, it is necessary for us to develop some improvements in order to apply the KM model.

Appendix A. k-means Clustering

In this appendix, we describe k-means clustering method. We used k-means mehtod to partition lower embeded space of NCuts.

Firstly, Consider the problem of identifying clusters of data points in a multi-dimensional space. We have a data set $(x_1, \ldots, x_N)$ consisting of N observations of randam D-dimensional Euclidian variable x. The goal of this methd is to partition the data set into some number K of clusters. Then, we suppose for the moment that the value of K is given. Intuitively, we think of a cluster as comparising a group of data points outside of the cluster. We can formalize the notation by first introducing a set of D-dimensional vectors μ_k, where $k = 1, \ldots K$. The μ_k is a prototype asociated with the kth cluster. As we shall see shortly, we can think of the μ_k as representing the centers of the clusters. Then, the goal is to find an assignment of data points to clusters, as well as a set of vectors $\{\mu_k\}$, such that the sum of the squares of the distances of each data point to its closest vector μ_k, is a minimum.

It is convenient at this point to define some notation to describe the assignment of data points to clusters. For each data point x_n, we introduce a crresponding set of binary indicator variables $r_{nk} \in \{0, 1\}$, where $k = 1, \ldots K$, describing which of the K clusters the data point x_n is assigned to, so that if data point x_n is assigned to cluter k then $r_{nk} = 1$, and $r_{nj} = 0$ for $j \neq k$. This is known as the 1-of-K coding scheme. Then, we can define an objective function, sometimes called a *distortionmeasure*, given by:

$$J = \sum_{n=1}^{N} \sum_{k=1}^{K} r_{nk} \|x_n - m_k\|^2 \tag{5.1}$$

which represents the sum of the squares of the distances of each data point to its assigned vector μ_k. The goal is to find values for the r_{nk} and the μ_k so as to minimize J. We can do this through an itarative procedure in which each iteration involves two successive steps corresponding to successive optimizations with respect to the r_{nk} and the μ_k. First we choose some initial values for the μ_k. Then in the first phase, we minimize J with respect to the r_{nk}, keeping the μ_k fixed. In the second phase, we minimize J with respect to the μ_k, keeping r_{nk} fixed. This two-stage optimization is

then repeated until convergence.

Consider first the determination of the r_{nk}. Because J in Eq. 5.1 is a linear function of r_{nk}, this optimization can be performed easily to give a closed form solution. The terms involving different n are independent, and so, we can optimize for each n separately by choosing r_{nk} to be 1 for whichever value of k gives the minimum closest cluster center. More formally, this can be expressed as

$$r_{nk} = \begin{cases} 1 & if \ k = argmin_j \|x_n - \mu_j\|^2 \\ 0 & (otherwise) \end{cases} \tag{5.2}$$

Now consider the optimization of the μ_k with the r_{nk} held fixed. The objective function J is a quadratic function of μ_k, and it can be minimized by setting its derivative with respect to μ_k to zero giving

$$2 \sum_{n=1}^{N} r_{nk}(x_n - \mu_k) = 0 \tag{5.3}$$

which we can easily solve for μ_k to give

$$\mu_k = \frac{\sum_n r_{nk} x_n}{\sum_n r_{nk}} \tag{5.4}$$

The denominator in this expression is equal to the number of points assigned to cluster k, and so this result has a simple interpretation, namely set μ_k equal to the mean of all of the data points x_n assigned to cluster k.

Appendix B. Principal Component Analysis

In this Appendix, we descrbe about Principal Component Analysis (PCA), which is linear dimension reduction method. In dissertation, this method was often used for proposed methods. For examples, in chapter 3, we used both to reduce the dimension of spectra for local linear approximation, and to compare with nonlinear dimension reduction.

PCA is a technique that is widely used for applications such as dimensionality reduction, lossy data compression, feature extraction, and data visualization. It is also known *Karhunen − Loéve* transform.

Consider a data set of observations $\{x_n\}$ where $n = 1, \ldots, N$, and x_n is a Eulidian variable with dimensionality D. The goal is to project the data onto a space having dimemsionality $M < D$ while maximaizeing the variance of th projected data. For the moment, we shall assume that the value of M is given.

To begin with, consider the projection onto a one-dimansional vector u_1, which for convenience (and without loss generality). We choose to be a unit vector so that $u_1^T u_1 = 1$ (note that we are only interested in the direction defined by u_1, not in the magnitude of u_1 itself). Each data point x_n is then projected onto a scalar value $u_1^T x_n$. The mean of the projected data is $u_1^T \bar{x}$, where $\bar{x}$ is sample set means given by

$$\bar{x} = \frac{1}{N} \sum_{a=1}^{N} x_n \tag{5.5}$$

and the variance of the projected data is given by

$$\frac{1}{N} \sum_{n=1}^{N} \{u_1^T x_n - u_1^T \bar{x}\}^2 = u_1^T S u_1 \tag{5.6}$$

S is the data covariance matrix defined by

$$S = \frac{1}{N} \sum_{n=1}^{N} (x_n - \bar{x})(x_n - \bar{x})^T \tag{5.7}$$

We now maximize the projected variance $u_1^T S u_1$ with respect to u_1. Clearly, this has to be a constrained maximization to prevent $\|u_1\| \rightarrow \infty$. The appropriate constraint comes from the normalization condition $u_1^T u_1 = 1$. To enforce this constraint, we introduce a Lagrange multiplier that we shall denote by λ_1, and then make an unconstrained maximization of

$$u_1^T S u_1 + \lambda_1 (1 - u_1^T u_1) \tag{5.8}$$

By setting the derivative with respect to u_1 equal to zero, we see that this quantity will have a stationary point when

$$S u_1 = \lambda_1 u_1 \tag{5.9}$$

which says that u_1 must be an eigenvector of S. If we left-multiply by u_1^T and make use of $u_1^T u_1 = 1$, we see that the variance is given by

$$u_1^T S u_1 = \lambda_1 \tag{5.10}$$

and so the variance will be a maximum when we set u_1 equal to the eigenvector having the largest eigenvalue *lambda*$_1$. This eigenvectors is known as the first principal component.

We can define addtional principal components in an incremental fashion by choosing each new direction to be that which maximize the projected variance amongst all possible directions orthogonal to those already considered. If we consider the general case of an M-dimensional projection space, the optimal linear projection for which the variance of the projected data is maximized is now defined by M eigenvectors $u_1, \ldots, u_M$ of the data covariance matrix S corresponding to the M largest eigenvalues $\lambda_1, \ldots, \lambda_M$.

In some applications of PCA, the number of data points is smaller than th dimensionality of the data space. For example, we might want to apply PCA to a data set of a few hundred images, each of which corresponds to vector in a space of potentially several million dimensions (corresponding to three color values for each of the pixels in the image). Note that in a D-dimensional space a set of N points, where $N < D$, defines a linear subspace whose dimensionality is at most $N - 1$, and so there is little point in applying PCA for values of M that are greater than $N - 1$. Indeed, if we perform PCA we will find that at least $D - N + 1$ of the eigenvalues are zero, corresponding to eigenvectors along whose directions the data set has zero variance. Furthermore, typical algorithms for finding the eigenvectors of a $D \times D$

matrix have a computational cost that scale like $O(d^3)$, and so for applications such as the image example, a direct application of PCA will be computationlly infeasible.

References

[1] N. Apostoloff and A. Fitzgibbon. Bayesian video matting using learnt image prior. *in proceedings of IEEE CVPR*, 2004.

[2] A. Beer. Bestimmung der absorption des rothen lichts in farbigen flussigkeiten. *Ann. Phys. Chem*, 86(2):78–90, 1852.

[3] C. M. Bishop. Pattern recognition and machine learning. *Springer*, 2008.

[4] M. Born and E. Wolf. *Principles of Optics*. Cambridge, seventh edition, 1999.

[5] L. M. Bruse, C. H. Koger, and J. Li. Dimensionality reduction of hyperspectral data using discrete wavelet transform feature extraction. *IEEE Transactions on and remote sensing*, 40(10), 2002.

[6] S. Chandrasekhar. *Radiative Transfer*. Dover, New York, 1960.

[7] Y. Chuang, A. Agarwala, B. Curless, D.H. Salesin, and R. Szeliski. Video matting of complex scenes. *in proceedings of SIGGRAPH*, 2002.

[8] Y. Chuang, B. Curless, D.H. Salesin, and R. Szeliski. A bayesian approach to digital matting. *in proceedings of IEEE CVPR*, 2001.

[9] Y. Chuang, D.B. Goldman, B. Curless, D.H. Salesin, and R. Szeliski. Shadow matting and compositing. *in proceedings of SIGGRAPH*, 2003.

[10] P. E. Debevec. Making the parthenon.

[11] R. Fattal. Single image dehazing. *to appear in SIGGRAPH*, 2008.

[12] P. F. Felzenszwalb and D. P. Huttenlocher. Efficient graph-based image segmentation. *IJCV*, 59(2), 2004.

[13] G. F.Hughes. On the mean accuracy if statical pattern recognizers. *IEEE Trans.Theory*, IT-14(1):55–68, 1968.

[14] G.D. Finlayson, S.D. Hordley, and P.M. Hubel. Color by correlation: a simple, unifying, framework for color constancy. *IEEE Trans. on PAMI*, 23(11):1209–1221, 2001.

[15] G.D. Finlayson and G. Schaefer. Solving for color constancy using a constrained dichromatic reflection model. *IJCV*, 42(3):127–144, 2001.

[16] G.D. Finlayson and S.D.Hordley. Color constancy at a pixel. *JOSA A.*, 18(2):253–264, 2001.

[17] C. Fowlkes, S. Belongie F. Chung, and J. Malik. Spectral grouping using the nystrom method. *IEEE Trans. on PAMI*, 26(2), 2004.

[18] Z. Fu, A. R. Kelly, T. Caelli, and R. T. Tan. On automatic absorption detection for imaging spectroscopy: A comparative study. *IEEE Transaction on geoscience and remote sensing*, 45(11), 2007.

[19] Y. Furukawa and J. Ponce. Accurate, dense, and robust multiview stereopsis. *in proceedings of IEEE CVPR*, 2007.

[20] T. Gevers, H. M. G. Stokman, and J. van de Weijer. Color constancy from hyper-spectral data. *Proceedings of British Machine Vision Conference*, 2000.

[21] M. Goesele, B. Curless, and S. M. Seitz. Multi-view stereo revisited. *in proceedings of IEEE CVPR*, 2:2402–2409, 2006.

[22] M. Gong and Y. H. Yang. Fast unambiguous stereo matching using reliability-based dynamic. *IEEE Trans. on PAMI*, 27(6):998–1003, 2005.

[23] H. Haneishi, S. Miyahara, and A. Yoshida. Image acquisition technique for high dynamic range scenes using a multiband camera. *Color research and application*, 31(4), 2006.

[24] T. Hasegawa and M. D. Fairchild. Estimation of object reflectance spectra from digital camera images. *Proceedings of the 12th Color Imaging Conference: Color Science and Engineering Systems, Technologies, Applications*, 2004.

[25] H. Hayakawa. Photometric stereo under a light source with arbitrary motion. *JOSA A.*, 11(11):3079–3089, 1994.

[26] C. Hernández, G. Vogiatzis, and R. Cipolla. Multiview photometric stereo. *IEEE Trans. on PAMI*, 30(3):548–554, 2008.

[27] A. Hertzmann and S. M. Seitz. Example-based photometric stereo: shape reconstruction with general, varying brdfs. *IEEE Trans. on PAMI*, 27(8):1254–1264, 2005.

[28] H. Hirschmuller and D. Scharstein. Evaluation of cost functions for stereo matching. *in proceedings of IEEE CVPR*, pages 1–8, 2007.

[29] A. Ikari, T. Masuda, T. Mihashi, K. Matsudo, N. Kuchitsu, and K. Ikeuchi. High quality color restoration using spectral power distribution for 3d textured model. *Proc 11th International conference on virtual system and multimedia*, 2005.

[30] K. Ikeuchi. Determining surface orientations of specular surfaces by using the photometric stereo method. *IEEE Trans. on PAMI*, 3(6):661–669, 1981.

[31] K. Ikeuchi and D. Miyazaki. Digitally archiving cultural objects. *Springer,New York*, 2007.

[32] K. Ikeuchi, T. Oishi, J. Takamatsu, R. Sagawa, A. Nakazawa, R. Kurazume, K. Nishino, M. Kamakura, and Y. Okamoto. The great buddha project:digitally archiving, restoring, and analyzing cultureal heritage objects. *IJCV*, 75(1):189–208, 2007.

[33] G. M. Johnson and M. D. Fairchild. Full spectral color calculations in realistic image synthesis. *IEEE Computer Graphics and Applications*, 19(4):47–53, 1999.

[34] D.B. Judd, D.L. MacAdam, and G. Wyszecki. Spectral distribution of typical daylight as a function of correlated color temperature. *Journal of Optics Society of America*, 54(8):1031–1040, 1964.

[35] T. Kakuta, T. Oishi, and K. Ikeuchi. Development and evaluation of asuka-kyo mr contents with fast shading and shadowing. *VSMM*, 2008.

[36] R. Kawakami, J. Takamatsu, and K. Ikeuchi. Color constancy from black body illumination. *JOSA A.*, 24(7), 2007.

[37] R. Kawakami, R.T. Tan, and K. Ikeuchi. Consistant surface color for texturing large objects in outdoor scenes. *in proceedings of IEEE ICCV*, 2, 2005.

[38] N. Keshava and J. F.Mustard. Spectral unmixing. *IEEE Signal processing magazine*, 2002.

[39] G.J. Klinker. *A Physical Approach to Color Image Understanding*. PhD thesis, Carnegie Mellon University, May 1988.

[40] G.J. Klinker, S.A. Shafer, and T. Kanade. The measurement of highlights in color images. *IJCV*, 2:7–32, 1990.

[41] G. Kortoum. *Reflectance Spectroscopy*. Springer-Verlag, New York, 1969.

[42] P. Kubelka and F. Munk. Ein beitrag zur optik der farbanstriche. *Z. Tech. Phys*, 12:593–601, 1931.

[43] H. Kwon and N. M. Nasrabadi. Kernel matched subspace detectors for hyperspectral target detection. *IEEE Trans. on PAMI*, 28(2), 2006.

[44] Ikeuchi lab. Bayon digital archival project.

[45] J.H. Lambert. Photometria sive de mensura de gratibus luminis, colorum et umbrae. *Eberhard Klett: Augsberg, Germany*, 1760.

[46] D. Landgrebe. Hyperspectral image data analysis. *IEEE Signal processing magazine*, 2002.

[47] H. C. Lee. Introduction to color imaging science. *Cambridge University Press*, 2005.

[48] A. Levin, A. R. Acha, and D. Lischinski. Spectral matting. *in proceedings of IEEE CVPR*, 2007.

[49] A. Levin, D. Lischinski, and Y. Weiss. Colorization using optimization. *in proceedings of SIGGRAPH*, 2004.

[50] A. Levin, D. Lischinski, and Y. Weiss. A closed form solution to natural image matting. *in proceedings of IEEE CVPR*, 2006.

[51] M. Levoy. The digital michelangelo project. *in proceedings of SIGGRAPH*, 2000.

[52] Y. Li, J. Sun, C. Tang, and H. Shum. Lazy snapping. *ACM Transactions on Graphics*, 23:303–308, 2004.

[53] David G. Lowe. Distinctive image features from scale-invariant keypoints. *IJCV*, 2004.

[54] D. Manolakis and G. Shaw. Detection algorithms for hyperspectral imaging applications. *IEEE Signal processing magazine*, 2002.

[55] T. Masuda, A. Ikari, T. Mihashi, K. Matsudo, N. Kuchitsu, K. Kawano, T. Yamashoji, M. Masuyama, R. Kamo, and K. Ikeuchi. Recognition of mural color in ozuka tumulus in sunlight and taper light. *VSMM*, 2005.

[56] T. Miyake, Y. Tokoyama, N. Tsumura, and H. Haneishi. Development of multiband color imaging systems for recording of art paintings. *Proc.SPIE*, 1999.

[57] D. Miyazaki, R.T. Tan, K. Hara, and K. Ikeuchi. Polarization-based inverse rendering from a single view. *in proceedings of IEEE ICCV*, 2003.

[58] P.S. Mudgett and L.W. Richard. Multiple scattering calculations for technology. *Applied Optics*, 10(7):1485–1502, 1971.

[59] Kyusyu National Museum. Decorated toms database.

[60] Tokyo Natioinal Museum and Ltd Toppan Printing Co. Tnm and toppan museum theater.

[61] Tokyo National Museum. Web archive.

[62] S. Narasimhan and S.K. Nayar. Interactive deweathering of an image using physical models. *IEEE Workshop on Color and Photometric Method in Computer Vision*, 2003.

[63] S. K. Nayar and S. G. Narasimhan. Vision in bad weather. *in proceedings of IEEE ICCV*, pages 820–827, 1999.

[64] K. Nishino, S.Y. Zhang, and K. Ikeuchi. Determining reflectance parameters and illumination distribution from a sparse set of images for view-dependent image synthesis. *in proceedings of IEEE ICCV*, pages 599–606, 2001.

[65] S. Noah, S. M. Steven, and S. Richard. Photo tourism: Exploring photo collections in 3d. pages 835–846, 2006.

[66] T. Oishi, A. Nakazawa, R. Kurazume, and K. Ikeuchi. Fast simultaneous alignment of multiple range images using index image. *Proc. Int'l Conf. 3-D Digital Imaging and Modeling*, 2003.

[67] T. Oishi, R. Sagawa, A. Nakazawa, R. Kurazume, and K. Ikeuchi. Parallel simultaneous alignment of a large number of range images on distributed memory system. *IPSJ*, 46(9):2369–2378, 2005.

[68] S.A. Prahl. Light transport in tissue. *PhD Thesis, University of Texas at Austin*, 1988.

[69] Y. Reibel, M. Jung, M. Bouhifd, B. Cunin, and C. Draman. Ccd or cmos camera noise charactarisation. *The European Physical Journal Applied Physics*, 21(1):75–80, 2003.

[70] E. Reinhard, M. Ahikmin, B. Gooch, and P. Shirley. Color transfer between images. *IEEE Computer Graphics and Applications*, 21(5):34–41, 2001.

[71] C. Rother, V. Kolmogorov, and A. Blake. Grabcut interactive foreground extraction using iterated graph cuts. *ACM Transactions on Graphics*, 23:309–314, 2004.

[72] S. Roweis and L. Saul. Nonlinear dimensionality reduction by locally linear embedding. *Science*, 2000.

[73] R.T.Tan. Visibility in bad weather from a single image. *in proceedings of IEEE CVPR*, 2008.

[74] M. Ruzon and C. Tomashi. Alpha estimation in natural images. *in proceedings of IEEE CVPR*, pages 18–25, 2000.

[75] R. Sagawa, K.Nishino, and K. Ikeuchi. Adaptively merging large-scale range data with reflectance properties. *IEEE Trans. on PAMI*, 27(3):392–405, 2005.

[76] R. Sagawa, K.Nishino, M.D.Wheeler, and K. Ikeuchi. Parallel processing of range data merging. *Proc. International conference Intelligent Robots and Systems*, 2001.

[77] Y. Sato, M.D. Wheeler, and K. Ikeuchi. Object shape and reflectance modeling from observation. *in proceedings of SIGGRAPH*, pages 379–387, 1997.

[78] B. Schölkopf, A. Smola, and K. R Müller. Nonlinear component analysis as a kernel eigenvalue problem. *Neural Computation*, 10:1299–1319, 1998.

[79] Y. Y. Schechner and N. Karpel. Clear underwater vision. *in proceedings of IEEE CVPR*, 2004.

[80] Y. Y. Schechner and S. K. Nayar. Generalized mosaicing:wide field of view multispectral imaging. *IEEE Trans. on PAMI*, 2000.

[81] S. M. Seitz, B. Curless, J. Diebel, D. Scharstein, and R. Szeliski. A comparison and evaluation of multi-view stereo reconstruction algorithms. *in proceedings of IEEE CVPR*, 1:519–526, June 2006.

[82] S. M. Seitz and C. R. Dyer. Photorealistic scene reconstruction by voxel coloring. *International Journal of Computer Vision*, 35(2):151–173, 1999.

[83] S. Shafer. Using color to separate reflection components. *Color Research and Applications*, 10:210–218, 1985.

[84] J. Shi and J. Malik. Normalized cuts and image segmentation. *IEEE Trans. on PAMI*, 22(8), 2000.

[85] F. Solomon and K. Ikeuchi. Extracting the shape and roughness of specular lobe objects using four light photometric stereo. *IEEE Trans. on PAMI*, 18(4):449–454, 1996.

[86] Specim. Imspector.

[87] J. Sun, J. Jia, C. Tang, and H. Shum. Poisson matting. *in proceedings of SIG-GRAPH*, 2004.

[88] J. Sun, N. N. Zheng, and H. Y. Shum. Stereo matching using belief propagation. *IEEE Trans. on PAMI*, 25(7):787–800, 2003.

[89] R. Szeliski, R. Zabih, D. Scharstein, O. Veksler, V. Kolmogorov, A. Agarwala, M. Tappen, , and C. Rother. A comparative study of energy minimization methods for markov random fields. *in proceedings of ECCV*, 2006.

[90] H. D. Tagare and R. J. P. deFigueiredo. A theory of photometric stereo for a class of diffusenon-lambertian surfaces. *IEEE Trans. on PAMI*, 13(2):133–152, 1991.

[91] Y. Taguchi, B. Wilburn, C. Zitnick, and C.L.Redmond. Stereo reconstruction with mixed pixels using adaptive over-segmentation. *in proceedings of IEEE CVPR*, 2008.

[92] R. T. Tan and K. Ikeuchi. iterative framework for separating reflection components of textured surfaces using a single image. *in Proceeding of International Symposium of the CREST Digital Archiving Project*, pages 67–81, 2003.

[93] R. T. Tan, K. Nishino, and K. Ikeuchi. Separating diffuse and specular reflection components based on surface color ratio and chromaticity. *in proceedings of IAPR International Workshop on Machine Vision Applications, MVA*, pages 14–19, 2002.

[94] R. T. Tan, K. Nishino, and K. Ikeuchi. Color constancy through inverse intensity chromaticity space. *JOSA A.*, 21(3):321–334, 2004.

[95] K. L. Tang, C. K. Tang, and T. T. Wong. Dense photometric stereo using tensorial belief propagation. *in proceedings of IEEE CVPR*, 1:132–139, 2005.

[96] J. B. Tenenbaum, V. de Silva, and J. C. Langford. A global geometric framework for nonlinear dimensionality reduction. *Science*, 290:2319–2323, 2000.

[97] S. Tominaga, T. Fukuda, and A. Kimachi. High-resolution imaging system for omnidirectional illumination estimation. *Proc. 15th Color Imaging Conference Final Program and Proceedings*, 2007.

[98] S. Tominaga and R. Okajima. Object recognition by multi-spectral imaging with a liquid crystal filter. *Proc. 15th Int. Conf. on Pattern Recognition*, 17(4), 2000.

[99] S. Tominaga and B.A. Wandell. Standard surface-reflectance model and illumination estimation. *JOSA A.*, 6(4):576–584, 1989.

[100] N. Tsumura, N. Ojima, K. Sato, M. Shiraishi, H. Shimizu, H. Nabeshima, S. Akazaki, K. Hori, and Y. Miyake. Image-based skin color and texture analysis/synthesis by extracting hemoglobin and melanin information in the skin. *ACM SIGGRAPH*, pages 770–779, 2003.

[101] G. C. Valls and L. Bruzzone. Kernel-based methods for hyperspectral image classification. *IEEE Transactions on and remote sensing*, 43(6), 2005.

[102] G. Vogiatzis, P. H. S. Torr, and R. Cipolla. Multi-view stereo via volumetric graph-cuts. *in proceedings of IEEE CVPR*, 2, 2005.

[103] J. Wang and M. F. Cohen. An iterative optimization approach for unified image segmentation and matting. *in proceedings of IEEE ICCV*, 2005.

[104] J. Wang and M. F. Cohen. Optimized color sampling for robust matting. *in proceedings of IEEE CVPR*, pages 1–8, 2007.

[105] J. Wasserman. Michelangelo's florence pieta. *Princeton University press*, 2003.

[106] Y. Wei and L. Quan. Region-based progressive stereo matching. *in proceedings of IEEE CVPR*, 1, 2004.

[107] J. Wexler, A.W. Fitzgibbon, and A. Zisserman. Image-based environment matting. *in proceedings of Eurographics*, 2002.

[108] J. Wexler, A.W. Fitzgibbon, and A. Zisserman. Bayesian estimation of layers from multiple images. *in proceedings of ECCV*, 2004.

[109] O. Woodford, R. Ian, P. H. S. Torr, and A. Fitzgibbon. Global stereo reconstruction under second order smoothness priors. *in proceedings of IEEE CVPR*, 2008.

[110] R. J. Woodham. Photometric method for determining surface orientation from multiple images. *Optical Engineering*, 19(1):139–144, 1980.

[111] G. Wyszecki and W.S. Stiles. *Color Science: Concept and Methods, Quantitative Data and Formulae*. Wiley Inter-Science, second edition, 1982.

[112] M. Yamaguchi, Y. Murakami, T. Uchiyama, K. Ohsawa, and N. Ohyama. Natural vision: Visual telecommunication based on multispectral technology. *Proc.IDW*, 2000.

[113] L. Zhang, B. Curless, A. Hertzmann, and S. Seitz. Shape and motion under varying illumination: unifying structure from motion, photometric stereo, and multiview stereo. *in proceedings of IEEE ICCV*, pages 618–625, 2003.

List of Publications

Journal Papers

1. Tetsuro Morimoto, Tohru Mihashi, Katsushi Ikeuchi, "Color Restoration Method Based on Spectral Information Using Normalized Cut," *International Journal of Automation and Computing.*,Vol.5,Num 3, July 2008

2.   ,   ,   "Normalized Cut
    ",   ,62, 9, September 2008

International Conferences

1. Tetsuro Morimoto, Katsushi Ikeuchi, "Multispectral Imaging for Material Analysis in an Outdoor Environment Using Normalized Cuts,"*In 10th IEEE International Conference on Computer Vision, Color and Reflectance in Imaging and Computer vision Workshop*, Kyoto, Japan, Oct.2009

2. Tetsuro Morimoto, Mayuko Chiba, Yoko Katayama, Katsushi Ikeuchi, "Multispectral Image Analysis for Bas-relief at the Inner Gallery of Bayon Temple," *Proceedings of 22nd CIPA Symposium*,Kyoto, Japan, 2009

3. Tetsuro Morimoto, Tohoru Mihashi, Katsushi Ikeuchi, "Color Restoration Method Based on Spectral Information Using Normalized Cut," *In 8th Asian Conference on Computer Vision, Workshop on Multi-dimensional and Multi-view Image Processing*, Tokyo, Japan, Nov. 2007

4. Shintaro Ono, Tetsuro Morimoto, Jun Takamatsu, Takeshi Oishi, Masataka Kagesawa, Katsushi, "3-D Modeling of Somma and Pompei Excavations Buried by Eruption of Mt. Vesuvio," Cities on Volcanoes 5 in Shimabara, November 2007

Domestic Conferences

1.   Robby T Tan,   ,   "
                                    ",   MIRU2009   ,
              July   2009

2.   "Normalized Cut   ",
                        MIRU2006   ,   July
    2008

3.   ,   "   ",
                        MIRU2007   ,August
    2007